Towards Photonic Chip Integration of an Oscillating Photonic Bell State from a Semiconductor Quantum Dot

by

Brady Cunard

A thesis
presented to the University of Waterloo
in fulfillment of the
thesis requirement for the degree of
Master of Science
in
Physics (Quantum Information)

Waterloo, Ontario, Canada, 2023

Author's Declaration

This thesis consists of material all of which I authored or co-authored: see Statement of Contributions included in the thesis. This is a true copy of the thesis, including any required final revisions, as accepted by my examiners. I understand that my thesis may be made electronically available to the public.

Statement of Contributions

The results in this thesis were only made possible with contributions from people in my group. The 4-f pulse shaper in Chapter 3 was created by Matteo Pennacchietti and I, and tomography apparatus in Chapter 3 was primarily constructed by those who came before us, but was modified by Matteo and I. The tomography measurements and data analysis was performed mainly by Matteo Pennacchietti, with significant help from myself, especially towards the end of the experiments. The entirety of Chapter 4 was a group effort between Sayan Gangopadhyay, Matteo Pennacchietti, and I, with help from Jack DeGooyer and Maeve Wentland. The photonic integrated circuit was completely designed by me.

Abstract

The demand for entangled photon sources has been growing in all areas of quantum information technologies. However, many modern single-photon sources suffer from fundamental limitations which limit their ability to produce these single-photons, as many of the "high quality" sources are probabilistic in nature. This probabilistic emission limits the "on-demand" requirement needed for many quantum information technologies. As a result, other types of single photon sources have been the topic of research for the past two decades, in which quantum dots are a promising candidate. Quantum dots are regions in space which electron-hole pairs can be confined and, using a phenomenon called "spontaneous emission," can emit single photons on demand. This is because the creation of electron-hole pairs is a deterministic process, which is a major topic of study in this thesis. In addition, the quantum dot which is the focus of this thesis is capable of emitting pairs of entangled photons on-demand, which have a wide array of applications in the quantum computing community. Our quantum dot is also embedded inside a nanowire, which this thesis will show, improves its performance in the areas which are considered important to the quantum dot, quantum computing, quantum networking, and quantum communication communities.

The nanowire quantum dots, comprised of an InAsP quantum dot embedded in an InP nanowire studied in this thesis show improvements over other quantum dot sources in key areas: photon purity, with a $g^{(2)}_{XX}(0) = 0.0055 \pm 0.0003$ and $g^{(2)}_{X}(0) = 0.0028 \pm 0.0003$, and entanglement, with peak concurrence (fidelity) values of $\mathcal{C}= 95.6 \pm 0.7\%$ ($\mathcal{F}= 97.7 \pm 0.4\%$) and lifetime weighted concurrence (fidelity) of $\mathcal{C}= 90.2 \pm 0.2\%$ ($\mathcal{F}= 94.0 \pm 0.1\%$). These results are an improvement from previous results on the same nanowire quantum dot, with peak concurrence of $\mathcal{C}= 87 \pm 4\%$ and lifetime weighted concurrence of $\mathcal{C}= 52 \pm 3\%$. The reason for the improvements on the same dot is because of the detection systems, superconducting nanowire single photon detectors. These detectors have far less timing jitter, dark counts, and higher efficiency than their counterparts, single photon avalanche diodes, which suggests these quantum dots are far better than previously thought. This thesis explores the effects of the detection systems in resolving a time-dependent oscillating quantum state, which occurs when a quantum dot has a fine-structure splitting. The fine-structure splitting is present in quantum dots that have strain, random alloying, or an asymmetric confining potential, causing asymmetry in the physical dimensions of the quantum dot. This asymmetry causes a lifting in the degeneracy of the exciton state, which causes the exciton state to precess. This oscillation happens on a timescale similar to the single photon avalanche diodes timing jitter, causing a "blurring" of the oscillating quantum state. This is mediated by using faster detectors, which this thesis will explore.

In addition to single photon sources, this thesis also focuses on the creation of photonic integrated circuits capable of supporting the photons emitted from our quantum dot. This is important because our quantum dot emits at wavelengths $\approx$ 894 nm, which is not supported by the silicon platform typically offered for photonic integrated circuits. This thesis will focus on a new platform, silicon nitride, which is capable of supporting light at our wavelengths. The results of this thesis demonstrate the simulated performance of the silicon nitride photonic integrated circuits at our wavelengths and lay the groundwork for a path forward to testing them with our source.

Acknowledgements

I would like to thank my group members for the support in the lab, and their willingness to offer their guidance whenever possible.

I would like to thank my friends and family for supporting me on this new journey in life. It was a difficult decision, but the correct one. I will be forever grateful for those who offered support and cheered for me.

I would like to thank Michael Reimer, my supervisor, for hiring me and putting his trust in me to become a member of this group.

I would like to thank Emily Nobes for catching my bad grammar mistakes and for her feedback.

I would also like to thank my cat, Yin, for offering many cuddles (often against her will) during the stressful nights writing this thesis.

Finally, I would like to thank my partner, Kaitlyn, for her love and support. It would not have been possible without her.

Table of Contents

List of Figures

List of Tables

Chapter 1

Introduction

Since its inception, the field of quantum information processing (QIP) has been developing at an unprecedented rate. Well-known quantum algorithms exist today that can solve problems which are un-computable for classical computers. Harnessing these algorithms through a quantum computer will revolutionize computing. However, there exists no current platform which can perform these algorithms on a meaningful scale. Despite this, the field of QIP has continued to evolve and make promising steps toward a potential platform capable of performing quantum algorithms and portraying a real advantage over their classical counterparts.

Some of the current platforms which show promise in a future of QIP include nuclear magnetic resonance (NMR) [5], trapped ions [6], semiconductor qubits [7], and nitrogen vacancies in diamond [8]. Each of these platforms have their own advantages and drawbacks, but due to the field of QIP still being in its infancy, it is unclear which platform will rise above the rest. These platforms are typically bulky (resource intensive with large spacial footprints) and lack universality; rudimentary quantum computers are limited in the types of operations they can perform. In contrast, classical computers are highly universal with a relatively small footprint. However, classical computers have limitations in areas of cryptography and database querying, which often rely on brute force algorithms dependent on the processing speed. Quantum computers harness quantum mechanical properties such as superposition and entanglement to surpass classical computers in these areas.

Like classical computers, quantum computers are comprised of simple components that, when combined, perform increasingly complex operations. The smallest building block in a classical computer is the transistor, which store information in a binary 0 or 1. Quantum computers emulate this information storage by using a "qubit," which refers to the state of

a quantum system. The qubit is represented as $|0\rangle$ and $|1\rangle$, and will be further explained in this thesis. One of the platforms which has been explored to represent the qubit is the photon. Photons are discrete "packets" of light which arise from the consequences of quantum mechanics; where confined particles have discrete energies. Photons are also "flying qubits," meaning they travel. This can make storing information difficult, but not impossible, as some solid state platforms attempt to store the information in cesium clouds [9], making photons a promising platform for QIP.

The optimal production of photons are debated in the quantum computing community. All platforms have their advantages and disadvantages, but there are efforts to improve in those areas. For example, spontaneous parametric down conversion sources emit "high quality" photons, but due to the process being probabilistic, do not emit photons on demand. The on-demand aspect of single photon emission is extremely important for quantum information and quantum computing applications, which makes the search for such a source important. Quantum dots, however, are great candidates for on demand emission, but suffer their own drawbacks as well. However, it can be shown that by manipulating the environment around the quantum dot by embedding it inside a nanowire can mitigate these issues. Quantum dots can also be utilized to emit entangled pairs of photons through the biexciton-exciton cascade, which is another highly sought after property. It is for these reasons that quantum dots have made their way to the forefront of quantum computing for their promise of high-quality, on-demand photons. To measure the quality of emitted photons, various experiments were performed, such as the Hanbury-Brown-Twiss and tomography experiments. It will become evident that the method of excitation used to produce these photons, along with the measurement systems used to detect them, directly affects the quality of emitted photons.

These experiments typically require many resources. Passive optics such as mirrors, beamsplitters, quarter and half waveplates, etc., require a large footprint and expensive detection equipment. A major goal of the QIP community is to reduce the footprint for commercial and personal purposes in the future. One way which is explored is by using photonic integrated circuits. These circuits confine light on a photonic chip, in which by creating simple elements of dielectric media, one can perform simple operations which emulate that of free space optics. Devices such as beamsplitters, waveplates, and filters can be made on these photonic integrated circuits. Photonic integrated circuits are also commercially available because they are CMOS compatible, capable of being fabricated using the same process as transistors in a classical computer.

This thesis will be organized as follows. Chapter 1 will establish the mathematics and physics required to describe the quantum systems, and establish photons as a viable platform to use in a quantum computer. Chapter 2 will establish quantum dots as a source of

entangled photons, while diving into the intricacies of their operation. It is in this chapter that the issue of fine-structure splitting is introduced. Fine-structure splitting occurs when there is an asymmetry in the confining potential inside our quantum dot, causing a degradation in entanglement. However, in addition to chapter 3 exploring how to determine the quality of the emitted photons, it also addresses how improvements in detection equipment, along with using a two-photon resonant excitation scheme, the issue of fine-structure splitting can be mitigated. Chapter 4 will explain in detail how photonic integrated circuits work, as well as components we designed specifically for the quantum dot. Finally, Chapter 5 will describe the results and lay the groundwork for future experiments.

1.1 Quantum Information

Quantum information processing refers to the study and manipulation of information through quantum mechanical principles and systems. It explores how these principles and systems can be used to store, process, and transmit data differently than classical computers. Through this review of classical computation, I will build a more comprehensive and intuitive understanding of the theory of QIP in a way which can be understood by a reader who has previous knowledge of classical computation.

As mentioned before, computation theory is the study of how systems store, process, and transmit data. To understand classical computation theory, we first need to establish what "data" is and how it is classically stored. In classical computation theory, data is raw information which has yet to be processed into something that can be interpreted. For example, data can be considered the ingredients in a recipe which has yet to be cooked. In classical computation theory, data comprises bits, or binary digits, which represent the smallest amount of information that can be represented in a classical computer. Bits can come in many forms, but always takes on one of two values: 0 or 1. In classical analogue systems, the bit can be implemented as a high or low voltage. For example, measuring 5 V corresponds to a logic 1 and measuring 0 V corresponds to a logic 0. There are also digital analogues to these systems, which use a metal-oxide-semiconductor field-effect transistor (MOSFET) to represent the bit. These MOSFETs either allow or inhibit the flow of current to represent the logical 1 or 0. Information stored in bits are processed by logic gates which take in multiple inputs to perform a calculation and produce an output. Measurement of the output will determine the answer to the calculation, and can consist of one or more bits stored in an array of bits as memory. This memory can be accessed later for further calculations.

In quantum information theory, the basic unit of information is called the qubit, or

quantum bit. Qubits are represented using "ket notation", $|\psi\rangle$, where ψ represents a quantum state and the brackets establish a "vector space" in which the state ψ resides. This vector space consists of orthogonal eigenvectors called state vectors, and any state within this vector space can be represented as a linear combination of these state vectors. Typically, these state vectors are represented as either $|0\rangle$ or $|1\rangle$

$$|0\rangle = \begin{bmatrix} 1 \\ 0 \end{bmatrix}, \qquad |1\rangle = \begin{bmatrix} 0 \\ 1 \end{bmatrix} \tag{1.1}$$

and, when measured, yield a result of either 0 or 1 with some probability for each outcome. Not knowing the outcome before measuring means there must be some distribution of probabilities between each state vector which describe $|\psi\rangle$. Because of this, $|\psi\rangle$ is represented as a linear superposition of $|0\rangle$ or $|1\rangle$. Because the probability of measuring $|0\rangle$ or $|1\rangle$ must be less than or equal to 1, the probability of measuring either $|0\rangle$ or $|1\rangle$ must be normalized to 1. As a result, $|\psi\rangle$ is represented as a sum of probability amplitudes, α and β, where α and β can be complex numbers and $|\alpha|^2 + |\beta|^2 = 1$.

To illustrate how we can represent states as a superposition, suppose we had a state $|\psi\rangle$ with the following outcome probabilities:

$$\begin{cases} 0 & \text{with probability of } \frac{1}{4} \\ 1 & \text{with probability of } \frac{3}{4} \end{cases} \tag{1.2}$$

if we follow the convention established earlier, we can represent the state as

$$|\psi\rangle = \sqrt{\frac{1}{4}}\,|0\rangle + \sqrt{\frac{3}{4}}\,|1\rangle \tag{1.3}$$

Where α and β can be complex states with the same outcome probability and can have a phase difference. For example, a state with the same outcome probabilities as equation 1.3 but with a phase difference may look like:

$$|\psi\rangle = \sqrt{\frac{1}{4}}\,|0\rangle + i\sqrt{\frac{3}{4}}\,|1\rangle \tag{1.4}$$

These quantum states can be represented up to a global phase, $|\psi\rangle = e^{i\phi}\,|\psi\rangle$ for $0 \leq \phi < 2\pi$. This phase difference does not have any physical meaning, but enables quantum algorithms to have advantages over classical algorithms. Quantum algorithms can use this phase

difference to constructively (or destructively) interfere the state of the output to make outcomes more (or less) likely to distinguish between these input states, which is a uniquely quantum effect, which is used in quantum search algorithm's such as Shor's factoring algorithm [10] and Grover's search algorithm [11].

With quantum phenomena like superposition and interference at the disposal, one might be wondering what physical system we can use to implement the algorithms to take advantage of these effects. One such system proposes we use photons as qubits. The proceeding sections of this thesis will expand on this proposal.

1.2 Photons and Photonic Qubits

Electromagnetic (EM) radiation has long been known to have wave-like properties. Maxwell proposed that all EM radiation consists of a time-varying electric and magnetic field, $\mathbf{E}(r,t)$[1] and $\mathbf{B}(r,t)$, respectively, which satisfy his four equations:

$$\nabla \times \mathbf{B}(r,t) = \mu_0 \mathbf{J}(r,t) + \frac{1}{c^2}\frac{\partial}{\partial t}\mathbf{E}(r,t) \tag{1.5}$$

$$\nabla \times \mathbf{E}(r,t) = -\frac{\partial}{\partial t}\mathbf{B}(r,t) \tag{1.6}$$

$$\nabla \cdot \mathbf{B}(r,t) = 0 \tag{1.7}$$

$$\nabla \cdot \mathbf{E}(r,t) = \frac{1}{\epsilon_0}\rho_V(r,t) \tag{1.8}$$

where μ_0 is the permeability of free space, c is the speed of light, $\mathbf{J}(r,t)$ is the current density, ϵ_0 is the permittivity of free space, and ρ_V is the volume charge density. The solution to these equations for a source free region ($\mathbf{J}= \rho_V = 0$) i.e. no electric charge densities or currents present in the region of interest, are:

$$\mathbf{E}(r,t) = Re\{E_0 e^{i(\mathbf{k}\cdot\mathbf{r}-\omega t)}\} \tag{1.9}$$

$$\mathbf{B}(r,t) = Re\{\mathbf{k} \times \frac{E_0}{\eta_0} e^{i(\mathbf{k}\cdot\mathbf{r}-\omega t)}\} \tag{1.10}$$

[1]Bolded variable represents a vector.

where $\eta_0 = \sqrt{\frac{\mu_0}{\epsilon_0}} = 120\pi$. This term is called the free-space characteristic impedance, which describes the impedance EM waves experience when travelling in a vacuum. k represents the wave vector number, which has the value of $k = \frac{2\pi}{\lambda}$, and $\mathbf{k} \cdot \mathbf{r}$ denotes the direction of propagation of the EM wave. ω represents the angular frequency of the EM wave.

The solutions to Maxwell's equations are sinusoidal functions dependent on the angular frequency, ω and follow the dispersion equation:

$$\omega = c|\mathbf{k}| \tag{1.11}$$

and particles can be described by their own dispersion relation:

$$E = \frac{|\mathbf{p}|^2}{2m} = \frac{1}{2}m\mathbf{v}^2 \tag{1.12}$$

where E is the energy, $\mathbf{p}$ is the momentum, m is the mass, and $\mathbf{v}$ is the velocity of a particle. When comparing the two, we notice that for an EM wave, $\omega \propto \mathbf{k}$ and for a particle, $E \propto |\mathbf{p}|^2$. Through Maxwell's equations, a relationship between energy and momentum has been obtained for a plane-wave described in terms of ω and $\mathbf{k}$.

Einstein proposed that in certain instances EM radiation consists of discrete quanta of energy [12] which take the form of:

$$E = \hbar\omega \tag{1.13}$$

where $\hbar$ is the modified Plank's constant, $\hbar = \frac{h}{2\pi}$. Assuming a photon is a particle of 0 mass, the total energy of a particle can be written as:

$$E = \sqrt{(m_0c^2)^2 + |\mathbf{p}|^2c^2} \tag{1.14}$$

where m_0 is the resting mass. By inserting the mass of the photon and equating it to equation 1.13 we get:

$$\hbar\omega = |\mathbf{p}| \cdot c \tag{1.15}$$

rearranging and inserting equation 1.11 we get:

$$\mathbf{p} = \hbar\mathbf{k} \tag{1.16}$$

$\|\psi\rangle$	Polarization Basis
$\|H\rangle$	Horizontal
$\|V\rangle$	Vertical
$\|D\rangle$	Diagonal
$\|A\rangle$	Anti-diagonal
$\|R\rangle$	Right-circular
$\|L\rangle$	Left-circular

Table 1.1: Complete set of polarization bases for photons.

We now have a direct relationship between the momentum of the photon and it's angular frequency.

From Maxwell's equations and Einstein's proposal of discrete energy levels from photons, we have established that photons behave as both particles and waves. By extension, we can use the Schrödinger equation to solve for the energy solutions for a given photon wave-function. Solutions to the Schrödinger equation are quantum in nature, therefore making photons prime candidates for the information carriers for quantum computation.

1.2.1 Polarization

With photons established as a platform for quantum information in the form of a qubit, it's useful to explore how this can be represented in a physical system. To establish a basis for qubits, there has to be some degrees of freedom in which we can encode information. For the purpose of this thesis, we will explore a photon's ability to encode information in its polarization degree of freedom, which will tie into the experiments explained in this thesis.

Polarization of a photon is described by the direction of oscillation of the electric field as it propagates through space, where the oscillation direction is perpendicular to its propagation direction. For a visualization, see figure 1.1. We must choose a convention to establish the qubits, meaning we must choose a direction of the oscillating field to encode $|0\rangle$ and $|1\rangle$ qubits to. It's useful to name polarization in terms of a horizontal and vertical basis, as it allows for easy visualization of the oscillating field. A field which is horizontally polarized will oscillate from side to side, a vertically polarized field will oscillate. Other polarization states include diagonal, anti-diagonal, right circularly, and left circularly polarized light. For brevity, we will refer to their ket notations:

By establishing $|H\rangle$ and $|V\rangle$ as $|0\rangle$ and $|1\rangle$ qubits respectively, we have established a basis set capable of encoding information to the photon polarization states.

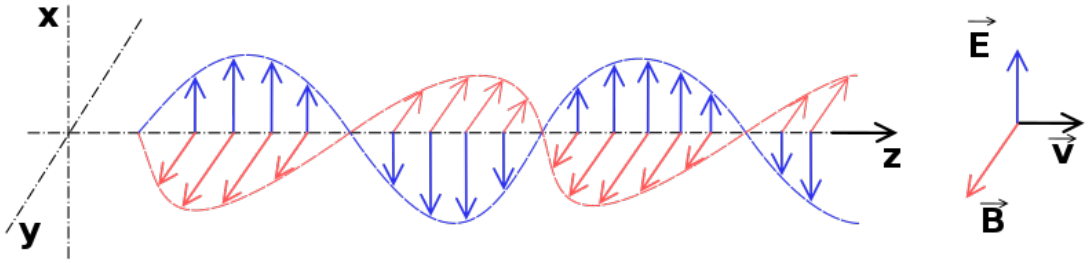

Figure 1.1: Representation of an oscillating electromagnetic field. The blue vectors represent the electric field oscillation, the red vector represents the magnetic field oscillation, and the black vector represents the direction of propagation. Figure by SuperManu, licensed under CC BY 4.0.

$$|H\rangle = \begin{bmatrix} 1 \\ 0 \end{bmatrix}, \qquad |V\rangle = \begin{bmatrix} 0 \\ 1 \end{bmatrix} \tag{1.17}$$

Using this basis as a starting point, it is possible to describe other polarization states in terms of these states. To do this, we will establish $|D\rangle$, $|A\rangle$, $|L\rangle$, and $|R\rangle$ in terms of their quantum information counterparts, i.e. $|D\rangle \to |+\rangle$, $|A\rangle \to |-\rangle$, $|L\rangle \to |i\rangle$, and $|R\rangle \to |-i\rangle$. Each of these bases can be represented by the following vector notation:

$$|+\rangle = |D\rangle = \frac{1}{\sqrt{2}} \begin{bmatrix} 1 \\ 1 \end{bmatrix} = \frac{1}{\sqrt{2}} \left(\begin{bmatrix} 1 \\ 0 \end{bmatrix} + \begin{bmatrix} 0 \\ 1 \end{bmatrix} \right) = \frac{1}{\sqrt{2}} (|H\rangle + |V\rangle), \tag{1.18}$$

$$|-\rangle = |A\rangle = \frac{1}{\sqrt{2}} \begin{bmatrix} 1 \\ -1 \end{bmatrix} = \frac{1}{\sqrt{2}} \left(\begin{bmatrix} 1 \\ 0 \end{bmatrix} - \begin{bmatrix} 0 \\ 1 \end{bmatrix} \right) = \frac{1}{\sqrt{2}} (|H\rangle - |V\rangle), \tag{1.19}$$

$$|i\rangle = |L\rangle = \frac{1}{\sqrt{2}} \begin{bmatrix} 1 \\ i \end{bmatrix} = \frac{1}{\sqrt{2}} \left(\begin{bmatrix} 1 \\ 0 \end{bmatrix} + \begin{bmatrix} 0 \\ i \end{bmatrix} \right) = \frac{1}{\sqrt{2}} (|H\rangle + i\,|V\rangle), \tag{1.20}$$

$$|-i\rangle = |R\rangle = \frac{1}{\sqrt{2}} \begin{bmatrix} 1 \\ -i \end{bmatrix} = \frac{1}{\sqrt{2}} \left(\begin{bmatrix} 1 \\ 0 \end{bmatrix} - \begin{bmatrix} 0 \\ i \end{bmatrix} \right) = \frac{1}{\sqrt{2}} (|H\rangle - i\,|V\rangle). \tag{1.21}$$

Bra-ket notation is a compact representation of vector algebra. For example, the inner product, $\langle a|b\rangle$ represents the dot product between two vectors $|a\rangle$ and $|b\rangle$. The outer product, $|a\rangle\langle b|$, represents a matrix formed out of the elements of $|a\rangle$ and the complex

transpose of $|b\rangle$, i.e. $|b\rangle^\dagger = \langle b|$. Using this, it can be shown that pairs of these basis states can form their own orthogonal basis set capable of encoding information. By using the definitions established, we can see that $|D\rangle$ and $|A\rangle$ form an orthonormal basis set and $|L\rangle$ and $|R\rangle$ also do.

$$\begin{aligned}
\langle D|A\rangle &= \left[\frac{1}{\sqrt{2}}(\langle H| + \langle V|)\right]\left[\frac{1}{\sqrt{2}}(|H\rangle - |V\rangle)\right] \\
&= \frac{1}{2}\left[\cancelto{1}{\langle H|H\rangle} + \cancelto{0}{\langle H|V\rangle} + \cancelto{0}{\langle V|H\rangle} - \cancelto{1}{\langle V|V\rangle}\right] \\
&= \frac{1}{2}\left[1 - 1\right] \\
&= 0
\end{aligned}$$

$$\begin{aligned}
\langle L|R\rangle &= \left[\frac{1}{\sqrt{2}}(\langle H| - i\langle V|)\right]\left[\frac{1}{\sqrt{2}}(|H\rangle + i|V\rangle)\right] \\
&= \frac{1}{2}\left[\cancelto{1}{\langle H|H\rangle} + i\cancelto{0}{\langle H|V\rangle} - i\cancelto{0}{\langle V|H\rangle} - \cancelto{1}{\langle V|V\rangle}\right] \\
&= \frac{1}{2}\left[1 - 1\right] \\
&= 0
\end{aligned}$$

With an understanding of how to mathematically represent polarization by using braket notation and linear algebra, it may not be obvious how we can extract this information in an experiment. In the next section, we will discuss what it means to measure photons, and the statistics that arise from them being treated as quantum objects.

1.2.2 Measurement

Measurement is often a difficult concept to conceive when talking about quantum objects such as photons. What does it mean to measure a photon? How can we measure a photon? What does that measurement tell us about the photon and, just as importantly, about the source from which the photon was produced? In this section we will establish a formal definition of measurement, answer some of the previously raised questions, and explore how we can perform these measurements in an experimental setting.

Photon measurement is a destructive measurement process, both physically and mathematically. Physically, when a photon is measured it is absorbed by a device that converts

its energy into an electrical signal which can be measured by sensitive electrical equipment. Mathematically, a photon that can be described by a quantum state $|\psi\rangle = \alpha|0\rangle + \beta|1\rangle$ will, when measured, appear in either $|0\rangle$ or $|1\rangle$ state. The probability amplitudes α and β describe the probability of $|\psi\rangle$ being measured in either $|0\rangle$ or $|1\rangle$ state after repeated measurements. When $|\psi\rangle$ is measured in either $|0\rangle$ or $|1\rangle$ state, we say $|\psi\rangle$ is collapsing to one of the two states. In other words, $|\psi\rangle = \alpha|0\rangle + \beta|1\rangle$ is a description of the full state but a measurement outcome of $|0\rangle$ or $|1\rangle$ represents the collapse of $|\psi\rangle$ onto one of the measurement basis states, $|0\rangle$ or $|1\rangle$, with probabilities of $|\alpha|^2$ and $|\beta|^2$ respectively. Repeated measurements are needed to determine α and β and fully reconstruct $|\psi\rangle$. This repeated measurement technique will be explored further in chapter 3.

To explore a mathematical definition of HOW to perform measurements, we first need to discuss operators and observables. Operators are mapping functions which "operate" on elements in a vector space. Observables are physical properties which can be measured, or physically "observed," and are represented by a Hermitian matrix. A Hermitian matrix, H, has the following properties:

$$H = H^\dagger \qquad \text{where} \qquad H^\dagger = (H^*)^T$$
$$HH^\dagger = H^\dagger H$$

where "*" represents the complex conjugate and the "T" represents the transpose.

Some examples of observables include position ($\hat{x}$, $\hat{y}$, $\hat{z}$), momentum ($\hat{p}$), and energy ($\hat{E}$). The "hats" on each observable denote linear operators, which have the property of preserving the linear structure of the space and obey the following properties:

$$\hat{M}(|\psi\rangle + |\phi\rangle) = \hat{M}|\psi\rangle + \hat{M}|\phi\rangle$$
$$\hat{M}(c|\psi\rangle) = c\hat{M}|\psi\rangle$$

where $\hat{M}$ is the linear operator, $|\psi\rangle$ and $|\phi\rangle$ are states, and c is some scalar constant. Because quantum mechanics has no standard basis, it is useful to work with abstract operators themselves, as we can freely change the basis in which we are working. To see how we can use operators to measure an observable, we can look at an example of a measurable quantity and see how these operators can be used to extract a measurement value. For example, let's start with energy[2], $\hat{E}$.

[2]Typically, the energy operator is denoted by $\hat{H}$, known as the *Hamiltonian*.

Suppose we construct an apparatus to measure the energy of the quantum particle, $|\psi\rangle$, as shown in figure 1.2. If the result of the measurement was such that the energy of $|\psi\rangle$ is 1 eV, then we know that $|\psi\rangle$ must have been in the state which would result in the measured outcome. If the measurement apparatus were to measure $|\psi\rangle$ to have an energy of 2 eV, then $|\psi\rangle$ must have been in the state which would result in the measured outcome, and so on. If we were to list the energies of $|\psi\rangle$ and associate the different energies to a particular state of ψ, we would get:

$$
\begin{aligned}
E_0 &\rightarrow |\psi_0\rangle \\
E_1 &\rightarrow |\psi_1\rangle \\
E_2 &\rightarrow |\psi_2\rangle \\
E_3 &\rightarrow |\psi_3\rangle \\
&\vdots \\
E_n &\rightarrow |\psi_n\rangle
\end{aligned}
$$

Each state $|\psi_n\rangle$ is known as a definite state, where $|\psi_n\rangle$ has a 100% certain value for its energy, E_n. The definite states are known as eigenstates, and the associated values obtained from the observable acting on them are the eigenvalues. Formally, we represent an observable acting on a state by $\hat{E}\,|\psi_n\rangle = E_n\,|\psi_n\rangle$.

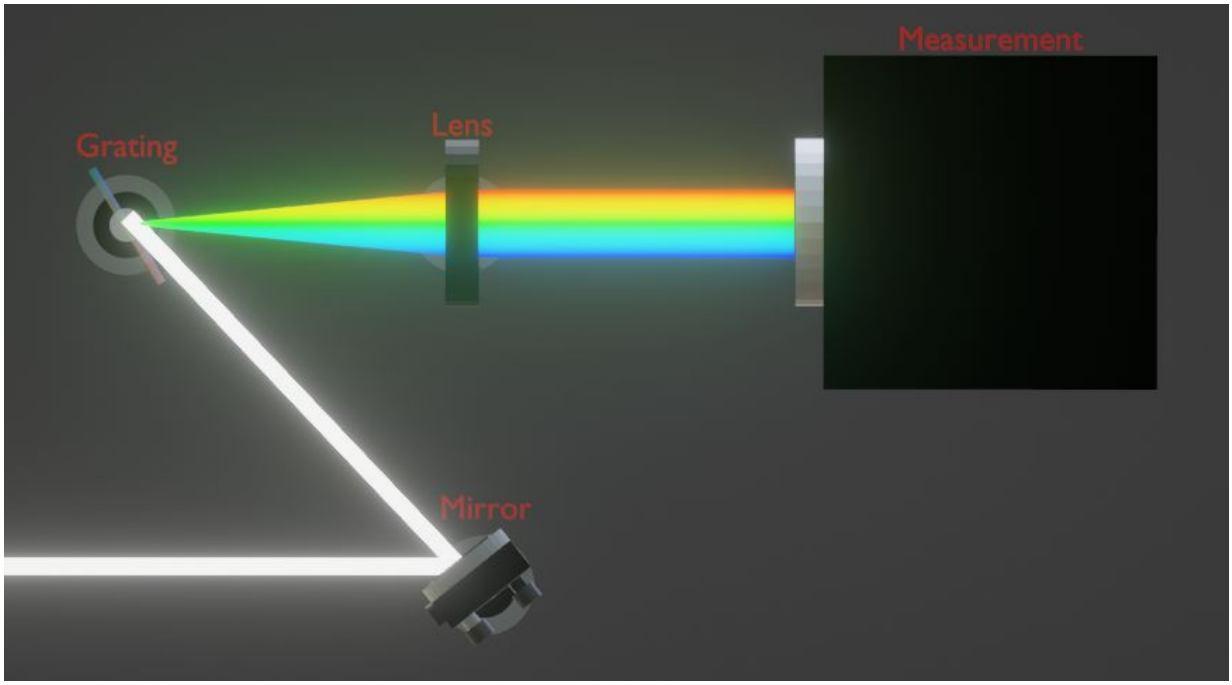

Figure 1.2: A physical measurement apparatus for measuring the energy of light. White light enters the setup, strikes a mirror, and is directed onto a reflective grating. The gratings' function is to separate the white light into its colour spectrum, such that light of different wavelengths reflect at different angles. The lens then collimates the light before entering the measurement device, where the intensity of each colour of light can be measured.

For a complete representation of $|\psi\rangle$, we must denote it as a superposition of all possible states.

$$|\psi\rangle = \alpha\,|\psi_0\rangle + \beta\,|\psi_1\rangle + \delta\,|\psi_2\rangle + ... + \gamma\,|\psi_n\rangle$$

where α, β, δ, and γ are the probability amplitudes mentioned in section 1.1 and all possible states up to $|\psi_n\rangle$ are the eigenvectors of $|\psi\rangle$. By repeatedly measuring observables, we can determine each of the eigenstates of $|\psi\rangle$. It's important to note that only one eigenvalue and eigenstate can be obtained per measurement, so multiple measurements are needed to determine the full representation of $|\psi\rangle$[3]. To summarize, every physical observable is represented by some linear operator in a vector space.

[3]This measurement process can be done with any observable associated with $|\psi\rangle$, not just energy.

Any observable of a physical system must adhere to the following rules:

1. Observables must have real[4] eigenvalues.
2. Observables' eigenstates must span the entire vector space.
3. Eigenstates must be mutually orthogonal.

Physical quantities are inherently real, and their eigenvalues must reflect that. Next, it may be difficult to understand why an observables' eigenstates must span the entire vector space. By recalling that any quantum state can be written as a linear combination of its eigenstates, i.e.

$$|\psi\rangle = \sum_i E_i \, |\psi_i\rangle$$

If we take the observable to be energy, then we can write $|\psi\rangle$ as a linear combination of all possible eigenstates associated with the energy observable. If there was some state $|\phi\rangle$ which could not be expressed in this way, $|\phi\rangle$ would not have any possible energy outcomes, since eigenstates represent the definite states obtained from a measurement. This is impossible since $|\phi\rangle$ MUST have some energy value when it is measured due to it being a physical system. This means that it can be written in a superposition of its energy eigenstates, thus we have reached a contradiction. Finally, it can be shown that these eigenstates must be mutually orthogonal. If we start with two non-orthogonal states, $|E_0\rangle$ and $|E_1\rangle$, shown in figure 1.3. Notice that we can decompose $|E_0\rangle$ into two components, $|E_1\rangle$ and $|E_{0\perp}\rangle$. Now, if we write $|E_0\rangle$ in terms of its components, we get $|E_0\rangle = \alpha \, |E_1\rangle + \beta \, |E_{0\perp}\rangle$. If we measure $|E_0\rangle$, there is some possibility of obtaining an eigenvalue of E_1, which does not correlate with how we defined these definite states. Remember, when measuring $|E_0\rangle$, there should be a 100% chance of obtaining E_0. Therefor, enforcing the orthogonality of the eigenstates $|E_0\rangle$ and $|E_1\rangle$.

[4]Real refers to the set of real numbers in mathematics.

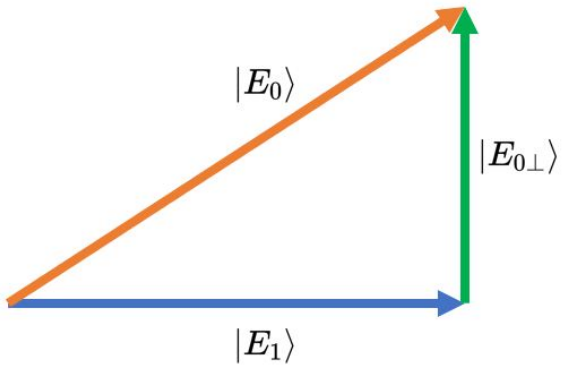

Figure 1.3: Non-orthogonal representation of two states, $|E_1\rangle$ and $|E_0\rangle$.

Now that we have established how we can represent measured physical quantities using operators and observables, we will delve into a mathematical procedure used in QIP to describe measurement of $|\psi\rangle$ in the "computational basis states", i.e. $|0\rangle$ and $|1\rangle$. Although quantum systems are physical systems and therefore have physical observables, for a purely informational point of view it is useful to describe measurements in terms of these basis states.

To begin, we must first establish the observables. These observables stem from the previously mentioned states in section 1.2.1 on polarization. In this instance, the eigenstates are $|0\rangle$, $|1\rangle$, $|+\rangle$, $|-\rangle$, $|+i\rangle$, and $|-i\rangle$ with observables X, Y, and Z where

$$X = \begin{bmatrix} 0 & 1 \\ 1 & 0 \end{bmatrix}, \qquad Y = \begin{bmatrix} 0 & -i \\ i & 0 \end{bmatrix}, \qquad Z = \begin{bmatrix} 1 & 0 \\ 0 & -1 \end{bmatrix}$$

and

$$\begin{aligned} X\,|+\rangle &= |+\rangle\,, \\ X\,|-\rangle &= -\,|-\rangle\,, \\ Y\,|+i\rangle &= |+i\rangle\,, \\ Y\,|-i\rangle &= -\,|-i\rangle\,, \\ Z\,|0\rangle &= |0\rangle\,, \\ Z\,|1\rangle &= -\,|1\rangle\,. \end{aligned}$$

Notice we can represent each of the observables in bra-ket notation, $X = |+\rangle\langle+| + |-\rangle\langle-|$, $Y = |+i\rangle\langle+i| - |-i\rangle\langle-i|$, and $Z = |0\rangle\langle0| - |1\rangle\langle1|$.

Because quantum mechanics is probabilistic, it's useful to talk about measurement outcomes in terms of probabilities. For example, if I begin with some state $|\psi\rangle$, which I can represent in any of the aforementioned basis states, what is the probability of measuring a particular outcome? To answer this question, we need to introduce projectors. Projectors are a tool which allow us to determine the probability of measuring $|\psi\rangle$ in any of the eigenstates. If we wanted to know the probability of $|\psi\rangle$ being in the $|0\rangle$ or $|+\rangle$ state, the projector will be $P_0 = |0\rangle\langle0|$ and $P_+ = |+\rangle\langle+|$ respectively, and so on for all other eigenstates. Suppose we want to determine the probability of measuring $|\psi\rangle$ in the $|+i\rangle$ state. We first establish the projector, $P_{+i} = |+i\rangle\langle+i|$, then we measure the associated probability by obtaining an "expectation value". The expectation value is the average outcome after many repeated measurements. Continuing with the example, the expected outcome for the state is $\langle\psi| P_{+i} |\psi\rangle = \langle\psi|+i\rangle\langle+i|\psi\rangle$. The outcome of $\langle\psi|+i\rangle$ denotes the amount of overlap (see figure 1.4) between $|\psi\rangle$ and $|+i\rangle$, thus giving us a probability of $|\psi\rangle$ being in state $|+i\rangle$.

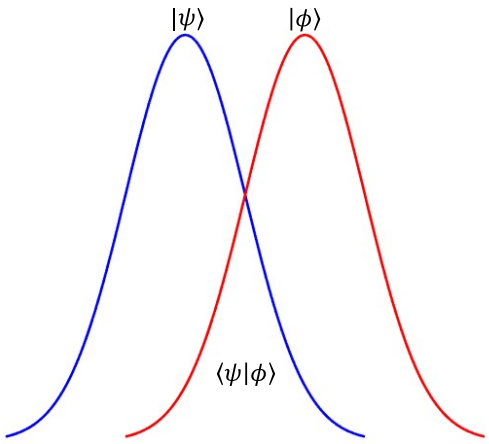

Figure 1.4: Visual representation of how two different states, $|\psi\rangle$ and $|\phi\rangle$ overlap. The region where they overlap is denoted as the inner product (dot product) of the two states, $\langle\psi|\phi\rangle$.

1.3 Multi-qubit Systems and Entanglement

So far, we have been under the assumption that we are working with single qubit systems. However, single qubit systems are not sufficient for a proper quantum computation scheme, similar to how one bit is not sufficient for a classical computation scheme. We need more qubits to store, process, and transmit data for quantum computational schemes on a scale which matches or surpass their classical counterparts. However, there are some interesting mathematical consequences arise from when introducing additional qubits to the system, which we will explore in this section.

Before we delve into introducing additional qubits, we must first establish the rules of tensor products. Tensor products allow us to combine elements from two vector spaces into a new vector space. Let's look at an example. Suppose we want to create a new vector space from vectors U and V. We can do this by taking the tensor product of the two vectors, $U \otimes V$. Elements of U and V ($u \in U$, $v \in V$) are individually tensored with one another to form a new space. To illustrate this, let's assume U and V are 2×2 matrices.

$$U = \begin{bmatrix} u_{00} & u_{01} \\ u_{10} & u_{11} \end{bmatrix}, \qquad V = \begin{bmatrix} v_{00} & v_{01} \\ v_{10} & v_{11} \end{bmatrix}$$

Now if we take $U \otimes V$ we get:

$$U \otimes V = \begin{bmatrix} u_{00}\begin{bmatrix} v_{00} & v_{01} \\ v_{10} & v_{11} \end{bmatrix} & u_{01}\begin{bmatrix} v_{00} & v_{01} \\ v_{10} & v_{11} \end{bmatrix} \\ u_{10}\begin{bmatrix} v_{00} & v_{01} \\ v_{10} & v_{11} \end{bmatrix} & u_{11}\begin{bmatrix} v_{00} & v_{01} \\ v_{10} & v_{11} \end{bmatrix} \end{bmatrix}$$

$$U \otimes V = \begin{bmatrix} u_{00}v_{00} & u_{00}v_{01} & u_{01}v_{00} & u_{01}v_{01} \\ u_{00}v_{10} & u_{00}v_{11} & u_{01}v_{10} & u_{01}v_{11} \\ u_{10}v_{00} & u_{10}v_{01} & u_{11}v_{00} & u_{11}v_{01} \\ u_{10}v_{10} & u_{10}v_{11} & u_{11}v_{10} & u_{11}v_{11} \end{bmatrix}.$$

The result is an entirely new space constructed from the elements of the old, individual spaces. We will use this property to build the multi-qubit system. Let's start with the computational basis states, $|0\rangle$ and $|1\rangle$. If we want to create a new space using these states, we again use the tensor product operation.

$$|0\rangle \otimes |1\rangle = \begin{bmatrix} 1 \begin{bmatrix} 1 \\ 0 \end{bmatrix} \\ 0 \begin{bmatrix} 1 \\ 0 \end{bmatrix} \end{bmatrix} = \begin{bmatrix} 1 \\ 0 \\ 0 \\ 0 \end{bmatrix}$$

To simplify the notation, we can use a well known shorthand notation to refer to a tensor product of two kets, which is $|a\rangle \otimes |b\rangle = |ab\rangle$. Using this shorthand notation, we can simplify the above to $|0\rangle \otimes |1\rangle = |01\rangle$. Notice that the tensor product does not commute, i.e. $|01\rangle \neq |10\rangle$ because

$$|1\rangle \otimes |0\rangle = \begin{bmatrix} 0 \begin{bmatrix} 1 \\ 0 \end{bmatrix} \\ 1 \begin{bmatrix} 1 \\ 0 \end{bmatrix} \end{bmatrix} = \begin{bmatrix} 0 \\ 0 \\ 1 \\ 0 \end{bmatrix}.$$

In general, the properties of tensor products are:

1. Linearity
   Any scalar a and b can be factored outside a tensor product:
   $(au) \otimes (bv) = (ab)(u \otimes v)$

2. Distributive
   The tensor product can be distributed over addition:
   $u \otimes (v + w) = u \otimes v + u \otimes w$

3. Associativity
   Brackets can permeate through the tensor product:
   $u \otimes (v \otimes w) = (u \otimes v) \otimes w$

4. Dual Spaces
   Conjugate transpose of tensor products are the same as the tensor product of conjugate transpose:
   $(u \otimes v)^\dagger = u^\dagger \otimes v^\dagger$

Physically, multiple qubits consist of multiple photons, where each photon represents a single qubit.

So far we have only been working with separable states, where the multi-qubit state was constructed via two independent states. In other words, we can represent the multi-qubit state as a tensor product of those independent states, i.e. $|01\rangle = |0\rangle \otimes |1\rangle$ or $|\psi\rangle = \alpha|0\rangle + \beta|1\rangle$. We can also introduce multi-qubit states, such as $|\phi\rangle = \alpha|00\rangle + \beta|01\rangle$. By using the distributive property, we can deconstruct this state into $|\phi\rangle = |0\rangle \otimes (\alpha|0\rangle + \beta|1\rangle)$. These two representations are equivalent and is a helpful representation when performing single qubit operations, i.e. manipulating qubit 1 or qubit 2.

However, how do we interpret the state $|\Phi\rangle = \frac{1}{\sqrt{2}}(|00\rangle + |11\rangle)$? This state is known as a "Bell State" and there is no way to deconstruct it into a tensor product of two smaller states like we just did with $|\phi\rangle$. Because of this, the state is known to be "entangled", which is one of the most important properties in enabling quantum computation. We will explore how we can quantify entanglement in section 1.3.2, but first we will need to introduce the "density matrix" and explore how it can be used to give a complete description of the quantum state.

1.3.1 The Density Matrix

The density matrix, also known as the density operator, is a mathematical tool which we can construct from the quantum states that hosts all the information in the quantum system. It is a fundamental concept of quantum mechanics for this reason. The symbol typically used to represent the density matrix is ρ.

Now that we have established why the density matrix is important in broad terms, we will explore how we can construct it and establish a general form which we can extrapolate to specific quantum states. First, we will construct a density matrix from a single qubit state $|\psi\rangle = \alpha|0\rangle + \beta|1\rangle$. From this state, the density matrix is defined as $\rho = |\psi\rangle\langle\psi|$, where $\langle\psi| = |\psi\rangle^\dagger = \alpha^*\langle 0| + \beta^*\langle 1|$. We can see how the density matrix is formed through the following example:

$$
\begin{aligned}
\rho &= |\psi\rangle\langle\psi| \\
\rho &= (\alpha|0\rangle + \beta|1\rangle)(\alpha^*\langle 0| + \beta^*\langle 1|) \\
\rho &= \alpha\alpha^*|0\rangle\langle 0| + \alpha\beta^*|0\rangle\langle 1| + \beta\alpha^*|1\rangle\langle 0| + \beta\beta^*|1\rangle\langle 1| \\
\rho &= |\alpha|^2 \begin{bmatrix}1\\0\end{bmatrix}\begin{bmatrix}1 & 0\end{bmatrix} + \alpha\beta^* \begin{bmatrix}1\\0\end{bmatrix}\begin{bmatrix}0 & 1\end{bmatrix} + \beta\alpha^* \begin{bmatrix}0\\1\end{bmatrix}\begin{bmatrix}1 & 0\end{bmatrix} + |\beta|^2 \begin{bmatrix}0\\1\end{bmatrix}\begin{bmatrix}0 & 1\end{bmatrix} \\
\rho &= \begin{bmatrix}|\alpha|^2 & \alpha\beta^* \\ \beta\alpha^* & |\beta|^2\end{bmatrix}.
\end{aligned}
$$

At first glance, the density matrix does not seem that impressive. However, this simple representation of a state is extremely useful due to its plethora of properties when describing PHYSICAL states, i.e. quantum states which we can physically observe. When taking this into account, the properties of the density matrix are as follows:

1. Density matrices are Hermitian:
   $\rho = \rho^\dagger$.

2. Density matrices are positive semi-definite:
   The eigenvalues of density matrices are positive to ensure the probabilities of measuring quantum states remains positive.

3. The trace of a density matrix is ALWAYS equal to 1:
   $Tr(\rho) = 1$
   Remember, taking the trace of a matrix involves taking the sum of the diagonals.
   $Tr\left(\begin{bmatrix} |\alpha|^2 & \alpha\beta^* \\ \beta\alpha^* & |\beta|^2 \end{bmatrix} \right) = |\alpha|^2 + |\beta|^2$

4. Determining whether a state is *pure* or *mixed*:
   $Tr(\rho^2)$ allows us to tell whether a state is pure or mixed.
   $Tr(\rho^2) = 1$ corresponds to a pure state
   $Tr(\rho^2) \leq 1$ corresponds to a mixed state. Mixed state density matrices can be represented as a probabilistic sum of pure state density matrices, $\rho = \sum_{i=0}^{m} P_i \left|\psi_i\right\rangle \left\langle\psi_i\right|$ where P_i is the probability of measuring some pure state $|\psi_i\rangle$.

5. Expectation values of observables can be found using density matrices:
   $Tr(\rho A) = \langle\psi| A |\psi\rangle =< A >$[5], where A is some observable.

There is also the concept of a "reduced density matrix". So far we've only been describing a density matrix which represents an entire system. However, if we have a system represented by a density matrix ρ_{ab} consisting of systems ρ_a and ρ_b, where $\rho_{ab} = \rho_a \otimes \rho_b$, there should be a method of retrieving the individual density matrices associated with each system. This method is known as a "partial trace". This involves "tracing out" one of the systems, leaving the desired system intact. Suppose we want to retrieve the density matrix ρ_a from the composite system ρ_{ab}. To do this, we perform a partial trace over the degrees of freedom of subsystem B. The notation for this operation is $\rho_a = Tr_b(\rho_{ab})$. Let's look at the following example, where the initial state is $|\psi_{ab}\rangle = \frac{1}{\sqrt{2}}(|01\rangle + |10\rangle)$.

[5] $< A >$ is a shorthand notation for the expectation value, $\langle\psi| A |\psi\rangle$.

First, we construct the density matrix using the method established earlier.

$$\rho_{ab} = |\psi_{ab}\rangle \langle\psi_{ab}|$$
$$\rho_{ab} = \frac{1}{2}[(|01\rangle + |10\rangle)(\langle 01| + \langle 10|)]$$
$$\rho_{ab} = \frac{1}{2}(|01\rangle \langle 01| + |01\rangle \langle 10| + |10\rangle \langle 01| + |10\rangle \langle 10|)$$

It's useful to leave ρ_{ab} in this form. Next, using the formal definition for the partial trace:

$$\rho_a = Tr_b(\rho_{ab}) = \sum_i (I_a \otimes \langle i|_b)\rho_{ab}(I_a \otimes |i\rangle_b) \tag{1.22}$$

Where $|i\rangle_b$ represents the basis state of subsystem b, and I_a represents the identity matrix for subsystem a, which can also be represented in bra-ket notation, $I = |0\rangle \langle 0| + |1\rangle \langle 1|$. Now, using equation 1.22, the partial trace becomes:

$$\rho_a = \frac{1}{\sqrt{2}}[(\langle 01|01\rangle + \langle 01|10\rangle) |0\rangle \langle 0| + (\langle 10|01\rangle + \langle 10|01\rangle) |1\rangle \langle 1|$$
$$\rho_a = \frac{1}{\sqrt{2}}[(0 + 1) |0\rangle \langle 0| + (0 + 0) |1\rangle \langle 1|]$$
$$\rho_a = \frac{1}{\sqrt{2}} |0\rangle \langle 0|$$

The result is a density matrix which describes the quantum state $|\psi_a\rangle$, obtained by tracing out the subsystem corresponding to the quantum state $|\psi_b\rangle$. Now that we've established the density matrix and its properties, we can use it in the quest to quantify entanglement.

1.3.2 Quantifying Entanglement

Entanglement up to this point has been described mathematically as a state which cannot be deconstructed into a tensor product of two smaller, pure states. However, this does not give us an intuitive description of WHAT entanglement is. Entanglement is nuanced in the sense that there are many levels of entanglement. There are "maximally entangled" states, such as the Bell state mentioned in section 1.3, and there are "unentangled/separable"

states. These are the two extreme cases, but, in reality, entanglement lies on a spectrum. In this section, we will explore the meaning of entanglement and how we can quantify the "amount" of entanglement in the state.

Remember, when we talk about qubits, we are talking about information. Entanglement is just another outcome of how information in quantum mechanics can be arranged. Entanglement tells us that the outcomes from the measurement of one qubit automatically implies the state of the other. To see this, let's look at a maximally entangled state, the Bell state mentioned in section 1.3, $|\Phi\rangle = \frac{1}{\sqrt{2}}(|00\rangle + |11\rangle)$. The measurement outcomes for qubit 1 are as follows:

$$\begin{cases} 0 & \text{with probability of } \frac{1}{2} \\ 1 & \text{with probability of } \frac{1}{2} \end{cases}$$

However, due to the entanglement, the outcomes for qubit 2 are already known based on the measurement outcome of qubit 1.

$$\begin{cases} \text{Qubit 1} = 0, & \text{Qubit 2} = 0, \text{ with probability of } 100\% \\ \text{Qubit 1} = 1, & \text{Qubit 2} = 1, \text{ with probability of } 100\% \end{cases}$$

We can see why this is the case because if we measure the first qubit to be in $|0\rangle$, we know that the second qubit must be in state $|0\rangle$ as well because of how the state is prepared. The information within the state allows us to efficiently measure one qubit and, with a 100% probability, know the outcome of the other qubit.

So far we have assumed that the Bell state is maximally entangled, which allows us to make the assumption of knowing the outcome of qubit 2 given the measured outcome of qubit 1. But how do we know? The next step to quantifying entanglement (i.e. determining how entangled the state is) is examining the entanglement of formation (EF) [13], which is a quantitative measurement of the entanglement of a bipartite quantum state. This is calculated by finding the Von Neumann entropy of the reduced density matrix of one of the qubits. The Von Neumann entropy tells us the amount of information contained in the quantum state and can tell us how far the reduced density matrix is from being a pure state.

The EF for a pure state is defined as

$$EF = -Tr[\rho_i ln(\rho_i)] \tag{1.23}$$

where ln is the natural matrix logarithm and ρ_i is the reduced density matrix for qubit i. The EF returns a value between 0 and 1 where 0 corresponds to a completely separable state (unentangled) and 1 corresponds to a maximally entangled state [14]. We can also represent the EF in terms of eigenvectors and eigenvalues, $\rho = \sum_i \lambda_i |i\rangle \langle i|$,

$$EF = -\sum_i \lambda_i ln(\lambda_i) \tag{1.24}$$

where λ_i is the eigenvalues for the associated eigenvector, $|i\rangle$. For a two qubit pure state, the EF can be rewritten in the form of a binary entropy function [13]:

$$EF = -xlog_2(x) - (1-x)log_2(1-x), \tag{1.25}$$

$$x = \frac{1+\sqrt{1-C(\rho)^2}}{2} \tag{1.26}$$

where x is monotonically increasing and ranges from 0 to 1, and $C(\rho)$ is known as the "concurrence" of the two qubit state, which also ranges between 0 and 1 [13].

Concurrence is a function of the density matrix and is a monotonically increasing function[6] of entanglement, and allows us to quantify the entanglement present between two qubits. Both EF and concurrence can be used to calculate entanglement, but concurrence is often the most preferred method due to the relative ease of calculation. To calculate concurrence, we will first explore how to calculate it for a pure state and then generalize it for any mixed state. To start, we will take the set of Bell states, i.e.:

$$\left|\Phi^+\right\rangle = \frac{1}{\sqrt{2}}(|00\rangle + |11\rangle) \tag{1.27}$$

$$\left|\Phi^-\right\rangle = \frac{1}{\sqrt{2}}(|00\rangle - |11\rangle) \tag{1.28}$$

$$\left|\Psi^+\right\rangle = \frac{1}{\sqrt{2}}(|01\rangle + |10\rangle) \tag{1.29}$$

$$\left|\Psi^-\right\rangle = \frac{1}{\sqrt{2}}(|01\rangle - |10\rangle) \tag{1.30}$$

[6]Monotonically increasing functions describes a function which is either increasing or "flat". It does not "dip down" for all values of x.

because we know that these states are maximally entangled, as asserted earlier in this section, we can define the concurrence for a pure state using these Bell states. First, we need to compact these states into an easy-to-use formula. Let $|\psi\rangle = \sum_{i=1}^{4} \alpha_i |e_i\rangle$, where $|e_i\rangle$ represents one of the Bell states and α_i represents the probability amplitudes. Using this representation, we can express the concurrence as [15]

$$C(\rho) = \left| \sum_{i=1}^{4} \alpha_i^2 \right|. \tag{1.31}$$

In other words, the concurrence is the magnitude of the sum of probability amplitudes for all pure states in the system.

Now that we've defined concurrence for a set of pure states, what about mixed states? We know that concurrence can take on any value between 0 and 1, where a completely separable (unentangled) state will give a value of $C(\rho) = 0$, and a maximally entangled state will give a value of $C(\rho) = 1$. But what about the values in between this range? From ref [13], it is shown that the concurrence for any two qubit mixed state can be found using the formula

$$C(\rho) = max(\lambda_1 - \lambda_2 - \lambda_3 - \lambda_4, 0) \tag{1.32}$$

where λ_i are the eigenvalues of the matrix $\sqrt{\sqrt{\rho}\tilde{\rho}\sqrt{\rho}}$, ordered from largest to smallest, where $\tilde{\rho} = (\sigma_y \otimes \sigma_y)\rho^*(\sigma_y \otimes \sigma_y)$, and ρ^* and σ_y are the complex conjugate of ρ and the Pauli-y matrix respectively. The 0 in the formula is to ensure that the concurrence is never negative, as those values are established to be impossible. This method of calculating concurrence and, by extension, entanglement, is how we will experimentally determine how entangled the pair of photons are. This is because calculating the concurrence of a mixed state is significantly easier to do than calculating the EF for a mixed state, and we do not know with certainty if the state generated in the experiments is truly a perfectly entangled state.

Another quantity of interest is "Fidelity". Fidelity tells us "how far" the measured state is from another state rather than a pure measurement of how entangled the state is, like concurrence. Fidelity is useful in the experiments because it can tell us how close we are to the desired entangled state, i.e. how close the measured state is to a Bell state[7]. The fidelity is defined as:

[7]It will be shown in chapter 3 why we want the measured state to be Bell a state.

$$F(\rho) = Tr[\rho\rho_0] \tag{1.33}$$

and

$$F(\psi) = |\langle\psi|\psi_0\rangle|^2 \tag{1.34}$$

where ρ_0 ($|\psi_0\rangle$) is the density matrix (state) we are referencing, i.e. the Bell state. Given some state ρ with a value of concurrence, $C(\rho)$, the fidelity to the maximally entangled state is bounded between [16]:

$$max\left(\frac{1+C}{4}, C\right) \leq F \leq \frac{1+C}{2} \tag{1.35}$$

meaning that the fidelity of a two-qubit system will always have values within the range of 0.25 and 1, and $C(\rho) \leq F(\rho)$. Both concurrence and fidelity are used in conjunction to quantify how entangled the measured state is, and how closely the state resembles the desired state. Throughout this thesis, we will focus on these two quantities when discussing entanglement.

Chapter 2

Entangled Photon Sources

2.1 Important Properties of Entangled Photon Sources

So far, we have discussed using photons as qubits by encoding information in their polarization degree of freedom. We have also discussed entanglement and what it means for QIP. However, we have not discussed HOW photons become entangled, which is directly related to how the photons are created. In this section, we will discuss potential entangled photon sources and weigh the benefits of each.

Entangled photon pairs can be generated in a variety of ways, such as radiative cascades or optical processes in non-linear crystals. However, regardless of the process, we require entangled photon sources to fit a list of criteria which determine the ideal photon source. The list consists of five properties:

1. **On-demand:** Photons are only produced when triggered.
2. **Bright:** The rate of producing photon pairs is high.
3. **No Multi-photon Emission Probability:** One and only one pair of photons is produced when desired.
4. **Entangled:** Each pair of photons emitted by the source is maximally entangled.
5. **Indistinguishable:** Each photon in the entangled pair have identical properties to subsequent emitted pairs, such as frequency and spacial mode.

An ideal photon pair source should satisfy all of these criteria. However, no source will satisfy all criteria perfectly, and after an in depth exploration of each of these criteria it will become clear.

2.1.1 On-Demand

To reiterate, a photon source is considered "on-demand" if and only if a photon is produced when the source is triggered to do so. The term "triggered" is a term used as a placeholder for any action which, when performed, the system in question will produce a photon. Some classical analogies to a triggering system include pressing the button on a walkie-talkie to allow yourself to communicate with the other device. There is no way to talk to the other device unless the button is pressed. This is the philosophy behind the "on-demand" property. For the purposes, we require a pair of entangled photons to be emitted when the triggering event is activated.

To be considered on-demand, an entangled two photon source must exhibit the following qualities: high photon pair generation probability, and high source pair extraction efficiency. Photon pair generation probability is the product of the probabilities of one photon being emitted after another for one triggering event [17]. This step is crucial because for one triggering event we want exactly two entangled photons, no more and no less, to ensure the protocol for encoding the information is implemented properly every time. The other crucial component, pair extraction efficiency, can be defined as the probability of collecting light at the output of the source [18]. The light is then collected into a fibre or an objective where it can be used for future experiments. For a truly on-demand source, having high pair generation probabilities and pair extraction efficiencies is crucial for performing QIP protocols.

One can see why it is important for a single photon pair source to be on-demand. For example, the Hong-Ou-Mandel experiment [19]. This experiment requires two photons to meet at a beamsplitter where they will interfere with each other and destructively interfere. The result is that there will be no coincidence[1] detection[2]. This is just one example of an experiment which can benefit from on-demand sources. Other experiments include quantum key distribution (QKD) [20], entanglement swapping [21], and linear optical quantum computing [22, 23].

[1] Coincidences are characterized by an on-off scheme where detectors are turned on by the first incoming photon and turned off by the second. The time between detections can be used to determine the distance between the photons, or when the photons were emitted.

[2] This is assuming the photons are indistinguishable. See section 2.1.5 for further context.

2.1.2 Single Photon Generation Probability Rate or "Brightness"

Brightness refers to the rate at which the source can generate entangled photon pairs. Typically, this measurement is denoted in counts per second, which refers to the number of photons which can be generated from the source. Because the QIP protocols require us to encode information on photons, we want to create as many photons as possible to maximize the amount of information we can encode. The more information we can encode, the more powerful the protocols can become. An analogy can be drawn to the classical modern day internet systems. Every internet service provider attempts to offer the "fastest" internet possible. Right now, typical internet speeds for a consumer can range from megabits to gigabits, meaning the amount of information flowing from the internet to your personal computer falls within that range. The same idea would be applicable for the quantum internet.

Every source has a theoretical limit to the number of photons it can generate. For example, a QD which produces entangled photon pairs through a bi-exciton exciton (XX-X) cascade is limited by the lifetimes of the XX and X [24]. If the lifetimes of the XX and X are 800 ps and 400 ps respectively, then the number of entangled photon pairs that can be produced, R, is less than the inverse of the sum of the lifetimes, i.e. $R < \frac{1}{(800+400)ps} = 833$ MHz. This relationship between the intrinsic rate at which photons can be generated and methods of increasing this is an important research field of its own. The results from such research will likely be used to improve single photon sources [25].

Because photon loss is common, having a high photon flux[3], and therefore a bright source, is desirable. QIP protocols using photons are typically carried out in free space, fibre optic networks, or photonic circuits[4]. Each of these methods involve photons travelling from point A to point B. The longer the photon is travelling and the more components it interacts with, the higher the probability that the photon will be absorbed and the information it carried will be lost. This inherently limits the scale of the QIP protocol. To counteract this, having a source that can transmit data at a high rate is desirable [26, 27].

2.1.3 No Multi-photon Emission Probability

Multi-photon emission probability refers to a source that emits only one pair of entangled photon pairs per triggering mechanism. The difference between multi-photon emission

[3]Photon flux refers to the number of photons passing through a given area.

[4]For more information on this topic, see chapter 4.

probability and on-demand photon sources is that on-demand refers only to an emission event. It does not care about WHAT is emitted. For example, a source can be triggered to emit a single photon but instead of emitting only one, it emitted multiple. This source is considered to be on-demand, but with high multi-photon emission probability. A source with no multi-photon emission probability would only emit the required number of photons in a given triggering event. It may emit them for every triggering event, but only the required number of photons is emitted per successful triggering event. Hence, why we want the source to be both on-demand and no multi-photon emission probability.

A well known method of measuring multi-photon emission probability is through a $g^{(2)}(\tau)$. The $g^{(2)}(\tau)$ is a second order correlation function which measures the difference in arrival time between two photons from the same emitter [28]. The $g^{(2)}(\tau)$ function can take on values between 0 and 1 and tell us how periodic the source is emitting. The function can be represented in the following equation:

$$g^{(2)}(\tau) = \frac{< \hat{a}^\dagger(0)\hat{a}^\dagger(\tau)\hat{a}(\tau)\hat{a}(0) >}{< \hat{a}^\dagger(0)\hat{a}(0) >^2} \tag{2.1}$$

where $\hat{a}^\dagger$ and $(\hat{a})$ are the creation and annihilation operators[5] respectively [28]. The values of τ represent arrival time separation of the photons [29]. Ideally, we want $g^{(2)}(0) = 0$, which is connected to the probability of emitting two or more photons at the same time [29, 28, 30].

For a single photon source, the $g^{(2)}(0) < 0.5$. The $g^{(2)}(0)$ function can also tell you the amount of background light present in the set-up. A source could be emitting in perfect time intervals but stray light entering the system can be detected, thus skewing the result. Thus, $g^{(2)}(0)$ can also be a metric of measuring the quality of the setup. Because the QIP protocols require pairs of photons, we need a low multi-photon emission probability, meaning we require the source emits two photons, one after another, in regular intervals. This will require an extension of the $g^{(2)}(0)$ experiment to incorporate a pair of photons. This experiment is known as the Hanbury-Brown-Twiss experiment and can be used to correlate between photons in two beams of light [31]. Further exploration of this method can be found in chapter 3.

[5] $\hat{a}^\dagger |n\rangle = \sqrt{n+1}\,|n+1\rangle$ and $\hat{a}\,|n\rangle = \sqrt{n}\,|n-1\rangle$ are often referred to as "ladder operators", which increment/decrement the number of photons in a particular mode, $|n\rangle$, respectively. Interestingly, $\hat{a}^\dagger\hat{a}$ returns the number of photons in mode $|n\rangle$, i.e. $\hat{a}^\dagger\hat{a}\,|n\rangle = n\,|n\rangle$.

2.1.4 Entanglement

For a physical system where we want to encode the information in the polarization degree of freedom on a pair of entangled photons. Experiments which require pairs of entangled photons require that the source can deterministically emit these entangled pairs. One example of such a source are quantum dots, which are well known platforms for generating these entangled pairs of photons [2, 32, 33, 34, 35, 36]. These quantum dot sources are capable of generating entangled photon pairs with fidelity and concurrence values of 0.859 ± 0.006 and 0.80 ± 0.02 respectively [2]. These sources are considered to be highly entangled in the quantum dot community and it is proposed that the limiting factor for these measured values of fidelity and concurrence lies in the measurement devices themselves[6] [37].

Entanglement is a key property which separate quantum algorithms from classical ones. Using entanglement, linear optics, and post-selection[7] has been proven powerful enough to solve bounded-error quantum polynomial time (BQP)[8] [38]. This makes it a powerful tool in all areas of computation. If we forgo universality[9], problems which are traditionally hard for classical computers to solve can be solved by a quantum computer with ease. An example of this was Xanadu's cloud based quantum computer tailored to solving the Gaussian Boson Sampling problem. This problem, which would take over 9000 years for a classical computer to solve, was solved in only 36 μs by their computer. More information on their quantum computer can be found in Ref. [39]. Based on the previous work in QIP protocols and experiments, there have been exciting results which show promise for the future of quantum computers, thanks to the unique property of entanglement.

2.1.5 Indistinguishable

The last desirable property of entangled photon sources which we require the source to have is for the photons to be indistinguishable. As mentioned before, indistinguishable is a qualitative description of the level of "sameness" between subsequently emitted photons. If two photons emitted have the same wavelength and spatial profile, they are considered to be indistinguishable. Any deviation of these parameters, whether it be inhomogeneous

[6] See section 2.2 for more information.

[7] Post-selection is the act of continuing a quantum algorithm given the outcome of an intermediate measurement.

[8] (BQP) is the class of decision problems solvable by a quantum computer in polynomial time, with an error probability of at most $\frac{1}{3}$ for all instances [38].

[9] Universality in computational theory is the concepts that a computer can solve many types of problems.

broadening from spin noise in the environment[10], or inconsistent temperatures causing the addressed energy levels in a QD to fluctuate can lead to a degradation of indistinguishability. A source which can emit indistinguishable photons is highly desirable because QIP protocols are implemented assuming all photons are the same.

Visibility of interference, or visibility for short, is a metric used to determine the level of indistinguishability. If two photons are indistinguishable and enter a beam splitter, they should both exit through the same port of the beamsplitter [19, 40, 41]. If this occurs, then there should be no coincidences measured, and the source is considered to have high visibility. Visibility is defined as

$$V = 1 - \frac{g^{(2)}(0)}{g_0^{(2)}(0)} \tag{2.2}$$

where $g^{(2)}(0)$ is the measured value and $g_0^{(2)}(0)$ is the measured value where the photons have been purposefully distinguishable [41]. For example, $g^{(2)}(0)$ would correspond to a measurement of two horizontally polarized photons and $g_0^{(2)}(0)$ would correspond to a measurement where one of the photons has their polarization rotated to vertically polarized. This act of rotating one of the photons' polarization ensures that there will be no interference in the beamsplitter, eliminating the condition of photons exiting exclusively through the same port. It is worth noting that visibility is typically taken over finite time windows. This is because environmental factors which can cause dephasing (inhomogeneous broadening) need time to influence subsequent photons. The result being the shorter the time window, the higher the visibility.

Highly indistinguishable photons are a sought after metric when considering photon sources. QIP protocols using linear optics are created assuming all the photons are the same, because we want the photons to interact with the components in the same way every time. QIP protocols using linear optics were first introduced in ref [22], where the components used were phase shifters and beam splitters. These components are passive optics, meaning we have no way of changing their properties as they act on individual photons. This type of QIP is called linear optical quantum computing (LOQC) and is a widely studied area in its own respect. We will explore more into this area in chapter 4 and delve into each of the passive optics components used in this scheme.

[10]Inhomogeneous broadening refers to mechanisms which result in the inconsistent widening of different emissions, which is wavelength dependent. For example, inhomogeneous broadening can cause the XX emission line to broaden more than the X emission line.

Figure 2.1: Visual representation of an ideal source, juxtaposed with how photon packets which deviate from the ideal will behave in different moments in time. Reused from [1], copyright 2017 by Springer International Publishing (see Copyright Permission Forms 5).

2.2 Quantum Dots

Thus far, we've alluded to potential platforms for entangled pairs of single photons. We've established the criteria and goals in which these sources should strive to achieve. In this section we will explore QDs, which is the subject of my research, and delve into the physics of how they work and how they create entangled pairs of single photons.

The methods used to grow the QDs are important. They determine the physical dimensions of the QD which in turn determine the electro-optical properties. There are a variety of materials which are used to grow these quantum dots, some of which include Gallium Arsenide (GaAs) [42, 43, 44, 45], Gallium Nitride (GaN) [46, 47, 48], and Indium Arsenide Phosphide (InAsP) [49, 50, 51, 52, 53, 54, 55]. In this thesis, we will focus on InAsP quantum dots embedded inside Indium Phosphide (InP) nanowires, as they are the focus of the research carried out in the lab. Next, we will explore the electro-optical properties of these quantum dots to gain insight on how they generate entangled photon pairs, some issues related to the growing techniques and how that relates to entanglement, and

finally how the nanowire creates an environment which can increase collection efficiency.

2.2.1 Confinement

Confinement refers to the modification of the conduction band (CB) and the valence band (VB) due to the confinement of the QD in space, and happens as materials of different electrical properties are deposited in the growing process. The change in the CB and VB result in local charge carriers being confined to the region. They exist in discrete energy levels within the new energy environment, as opposed to the continuous energy spectrum from the surrounding bulk environment. The reason this is desirable is that we have confined a region in space where the electrical properties are different from the surrounding areas, thus we can address this region directly.

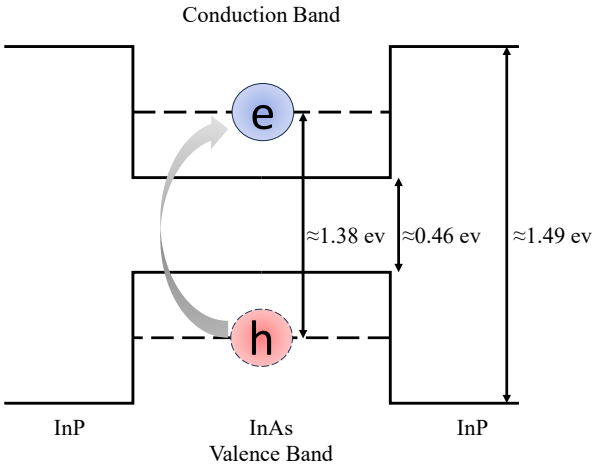

Figure 2.2: This figure shows the band structure of the quantum dot. The band gap is formed when an InAs material is deposited onto an InP material, modifying the bulk energy structure. As the bands are modified, they confine electrons and holes inside the CB and VB, whose wavefunctions are such that only electrons and holes of certain energies are allowed to exist inside the QD. It was determined that the energy of the bandgap is 0.46 eV, the energy of the first allowable excitation is 1.38 eV, and the energy from the VB to the CB is 1.49 eV.

To address this region in the context of this thesis means we need to "excite" it. Exciting the QD refers to increasing the energy of an "electron" (e), so that it "jumps" from the valence band to the conduction band, leaving behind a "hole" (h). These holes refer to

an absence of an electron and are positively charged relative to their environment. They also have a respective mass and spin as they move through their environment, similar to an electron. This movement is simply the propagation of the gap the electron left as other electrons move to fill it, which in turn leaves another gap.

The confinement that happens inside a QD has a similar structure to that of an atom. As electron-hole pairs are excited inside the QD, they can also occupy higher energy levels. These energy levels are similar to that of the electron shells inside an atom, where the first excited level is the s-shell, the next is the p-shell, and so on. These levels are formed due to the geometry of the QD, which can be modelled as a "hockey puck", as seen in figure 2.3. The reason for the hockey puck shape is because of how it is grown; as a part of a nanowire. This structure as a whole is known as a nanowire QD (NWQD) and will be explored further in section 2.2.4.

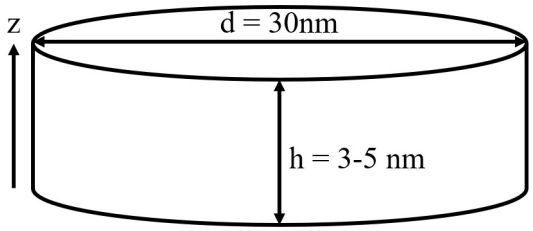

Figure 2.3: Simplified representation of the QD. The QD is about 3-5 nm in height with a diameter of about 30nm.

The strong confinement from the QD comes from the z direction, i.e. the height of the QD and the Bohr radius, a_0. For QDs of the type shown in figure 2.3, $a_0 \approx 25$ nm [56], the confinement only allows for one electron-hole pair inside the QD. This confinement has vertical walls for the CB and VB (see figure 2.2), which are the hallmarks of a quantum well. But, if we look at the QD in three dimensions, there is also confinement in the radial direction. This allows for sublevels to form, which are the s, p, d shells and so on. The confinement in this direction resembles that of a two-dimensional quantum harmonic oscillator (QHO). The equation for a QHO looks like

$$V(r) = \frac{1}{2} m^* \omega^2 r^2 \tag{2.3}$$

where m^* is the effective mass of the electron or hole (depending on whether we are looking at the CB or VB respectively), and $r = (x, y)$, representing the x or y direction,

corresponding to the two degrees of freedom mentioned previously [57]. The solutions to the allowable energy states given these parameters are

$$E_{n,l} = (2n + |l| + 1)\hbar\omega \tag{2.4}$$

where $n = 0, 1, 2, ...$ and $l = 0, \pm1, \pm2, ...$ are the radial and orbital quantum numbers respectively, and $\hbar\omega$ is the quantized energy of the electron or hole. These quantum numbers give rise to these sublevels and the existence of degenerate states[11]

For the purposes of the experiments, we will be focusing on just the s-shell of the QD, which we can use to deterministically generate the entangled photons. In figure 2.2, we point out that electrons and holes appear in pairs. Wherever there is a hole, there was an electron that was excited to create it. This coupling of the two particles creates their own quasi-particle known as an "exciton". This exciton has its own electro-optical properties which allows us to create photons. In the next section, we will explore how we can use the exciton to create photons and how the process unfolds inside the QD system.

2.2.2 Photon Generation

Now that we've established how QDs can confine electrons and holes inside them in the form of an exciton, next we will explore how we can use these states to generate photons, and then expand on this to explain how we can generate entangled photons. To begin, we first need to revisit photons from chapter 1. We know that photons have spin angular momentum [58], which we will use in conjunction with electron-hole dynamics inside the QD explained in section 2.2.1 to explain how to produce photons.

When the QD is excited, it creates an electron-hole pair as the electron jumps to the CB. The electron will wait until it relaxes back to the VB and the electron and hole recombines. This relaxation-combination sequence is a radiative process, meaning there is a photon produced [59]. However, it is not obvious WHY a photon is produced during this process. To explore why this is, we need to explore the optical selection rules.

[11] Degenerate states refer to solutions to the Schrödinger equation, where different states can have the same energy eigenvalues. This can occur, for example, when an electron with spin $\frac{1}{2}$ can be a solution and an electron with spin -$\frac{1}{2}$ can also be a solution. Both electrons have the same energy but opposite spins, meaning two different states can have the same energy eigenvalue solutions, thus they are degenerate.

Optical Selection Rules

Optical selection rules are a set of rules which govern optical transitions between energy states inside physical systems, in this case a QD. These rules dictate that the total angular momentum will be preserved during these transitions. To apply these rules to the system, we need a description of the angular momentum of the states inside the QD. To do this, we reintroduce operators, particularly the angular momentum operator, $\hat{\mathbf{J}}$, where $\mathbf{J}$ represents the total angular momentum of the system. $\mathbf{J}$ can be represented as the sum of all angular momentum and spin processes in the system:

$$\hat{\mathbf{J}} = \hat{\mathbf{L}}_{band} + \hat{\mathbf{L}}_{e,h} + \hat{\mathbf{S}} \tag{2.5}$$

where $\hat{\mathbf{L}}_{band}$ represents the angular momentum of the internal band (CB or VB), $\hat{\mathbf{L}}_{e,h}$ represents the angular momentum of the electron or hole, and $\hat{\mathbf{S}}$ represents the spin angular momentum. These operators return eigenvalues $j, l_{band}, l_{e,h}$, and s. Another important quantity to note is j_z, which is the projection of the total angular momentum onto the z-axis, and falls within a range of values between $-j$ and j, i.e. $j_z \in \{-j, -j+1, ..., j-1, j\}$. For example, if $j = 2$, then $j_z = \{-2, 1, 0, 1, 2\}$.

Electrons and holes are both spin $\frac{1}{2}$ particles, i.e. $s = \frac{1}{2}$. In a QD, electrons in the lowest energy state of the CB behaves like an s-shell orbital in an atom. In this case, both $\hat{\mathbf{L}}_{e,h} = 0$[12] and $\hat{\mathbf{L}}_{band} = 0$. Remember, we are only limiting ourselves to the lowest energy state because, as mentioned in section 2.2.1 in ref [56], one electron-hole pair are allowed inside the QD. In this lowest energy state, $\hat{\mathbf{J}} = \hat{\mathbf{S}}$, and as a result $j = s = \frac{1}{2}$ and $j_z = \pm\frac{1}{2}$. However, remember that in the QD we have a pair of electrons and holes. When the electron is excited into the CB, it leaves behind a hole. The electron will sit in the lowest energy state in the CB, but to minimize the energy difference between them, the hole must occupy a higher energy level in the VB. This results in the hole exhibiting p-orbital like behaviour. Because of this, the total angular momentum of this state has to involve the band momentum, resulting in the total angular momentum $\hat{\mathbf{J}} = \hat{\mathbf{L}}_{band} + \hat{\mathbf{S}}$. In this instance, $l_{band} = 1$, $s = \frac{1}{2}$, $j = \{|l_{band} + s|, |l_{band} - s|\} = \{\frac{3}{2}, \frac{1}{2}\}$, and $j_z = \{\{-\frac{3}{2}, -\frac{1}{2}, \frac{1}{2}, \frac{3}{2}\}, \{-\frac{1}{2}, \frac{1}{2}\}\}$ for holes and electrons respectively [60, 61]. Notice that holes can take on two different values of angular momentum: $j = \frac{3}{2}$ and $j = \frac{1}{2}$, which are referred to heavy holes (hh) and (lh) respectively. If we analyze the band structure of the QD, we can see a separation of these energy bands in the presence of uni-axial strain as a function of the wavevectors k

[12] This is true for electrons in the s-shell of the CB and holes in the p-shell of the VB because these are the lowest energy states allowed.

and $k_{\|}$, where k is the wavevector of the unit cell of the QD and $k_{\|}$ is perpendicular to the axis of strain.

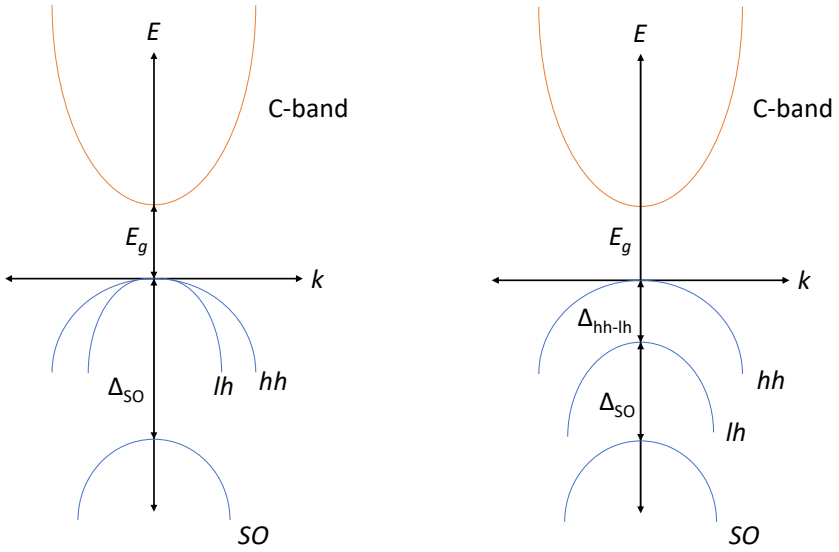

Figure 2.4: Here is the band structure for the CB and VB of a QD. The curve associated with the CB corresponds to the energy of the electron with $j = \frac{1}{2}$. In the VB, the holes are separated into three regimes: $j = \frac{3}{2}$, $j_z = \pm\frac{3}{2}$ for heavy holes, $j = \frac{1}{2}$, $j_z = \pm\frac{1}{2}$ for light holes, and $j = \frac{1}{2}$ for the lower energy state. The heavy holes and light holes are separated by Δ_{hh-lh}. Notice in both figures that the heavy holes and light holes "bend" at different rates, which is because of the spin-orbit coupling, denoted by Δ_{SO}.

Because we will be focusing on the lowest energy state, whenever the term holes are used from here on the will refer to the heavy holes, as they are the necessary component to produce the entangled photons. The reason for this is that for a photon to be emitted, it has to carry some momentum. The recombination of an electron with $j = \frac{1}{2}$ and a hole with $j = \frac{3}{2}$ will have some residual angular momentum. Due to the conservation of angular momentum, this residual angular momentum is not allowed. Thus, a photon is emitted containing this residual angular momentum. Therefor, the optical selection rules are such that

$$\Delta j = 1, \qquad \Delta j_z = \pm 1, \qquad \Delta s = 0. \tag{2.6}$$

For left circularly polarized (LCP) light, $\Delta j_z = +1$, and for right circularly polarized (RCP) light, $\Delta j_z = -1$.

Thus far, we have only touched on the exciton as the quasi-particle which can form inside the QD energy band structure when an excitation event occurs. However, due to the Pauli-exclusion principal, since these particles are fermions, two can occupy their respective states at a time given they have opposite spins. This phenomenon creates another, higher energy quasi-article known as the biexciton and is integral for photon pair generation.

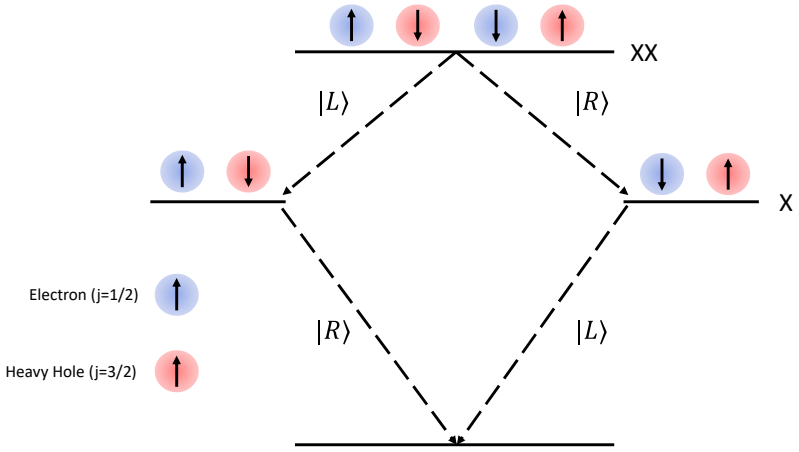

Figure 2.5: The biexciton-exciton (XX-X) cascade. Electron-hole pairs with their respective angular momentum recombine to emit either LCP or RCP, depending on their value of Δj_z. To create the entangled pair, the XX must fully decay into the ground state.

The QD can generate entangled photons through a process known as the biexciton-exciton (XX-X) cascade. It begins when two electrons of opposite spins are excited into the CB. what happens next can be one of two options: an electron-hole recombination can exhibit $\Delta j_z = -1$ followed by a $\Delta j_z = +1$, emitting an RCP photon followed by an LCP photon, and vice versa. These are the only two options available for the XX and the X, meaning that when the XX photon is emitted and measured to be either LCP or RCP, we know with certainty the polarization of the other, thus the pair of photons are entangled. This entangled state is known as the $|\Phi^+\rangle$ state, and is one of the maximally entangled Bell states, as seen in equation 2.7.

$$\left|\Phi^+\right\rangle = \frac{1}{\sqrt{2}}(|RL\rangle + |LR\rangle) \tag{2.7}$$

In the next section, we will explore the consequences of strain and it's effects on the energy band structure of the QD. Strain is an often unavoidable consequence of growing these QDs because of the lattice mismatching which occurs to form the islands necessary for the QD. This strain causes some deviations in the emission spectrum of the QD in the form of an energy splitting in the exciton. This energy splitting causes the ideal, time-independent Bell state to oscillate in time. This oscillating state is still entangled, and will be explored further in chapter 3.

2.2.3 Fine Structure Splitting

Throughout the previous sections, it was assumed that the QD was perfectly symmetrical in the radial direction. This perfect symmetry was necessary to obtain the energy level structure of the XX-X cascade shown in figure 2.5. However, this ideal situation can never be realized as slight deviations from the perfect symmetry are almost always present. This deviation, such as an elliptical shaped QD, can result in asymmetric radial confinement of charge carriers [62, 63, 64].

The asymmetry lifts the degeneracy of the two exciton states, meaning they are no longer at the same energy. The amount at which they are lifted, δ, is known as the fine structure splitting. The energy difference causes a phase accumulation proportional to δ and the time between the biexciton and exciton recombination, τ. Taking these two factors into account, the new state in the presence of fine structure splitting is now

$$\left|\tilde{\Phi}^+\right\rangle = \frac{1}{\sqrt{2}}(|HH\rangle + e^{i\tau\frac{\delta}{\hbar}}|VV\rangle) \tag{2.8}$$

where $\left|\tilde{\Phi}^+\right\rangle$ is the time dependent version of the Bell state $|\Phi^+\rangle$. By expanding into the circular basis, we can see an interesting behaviour,

$$\left|\tilde{\Phi}^+\right\rangle = \frac{1}{\sqrt{2}}(|RL\rangle + |LR\rangle)\cos\left(\frac{\delta\tau}{2\hbar}\right) - \frac{1}{\sqrt{2}}(|RR\rangle + |LL\rangle)i\sin\left(\frac{\delta\tau}{2\hbar}\right). \tag{2.9}$$

If we analyze the equation, we can see there are some oscillatory terms, $\cos\left(\frac{\delta\tau}{2\hbar}\right)$ and $i\sin\left(\frac{\delta\tau}{2\hbar}\right)$. What these oscillating terms do is cause an oscillation between the two bell

states $|\Phi^+\rangle$ and $|\Psi^+\rangle$[13] [65].

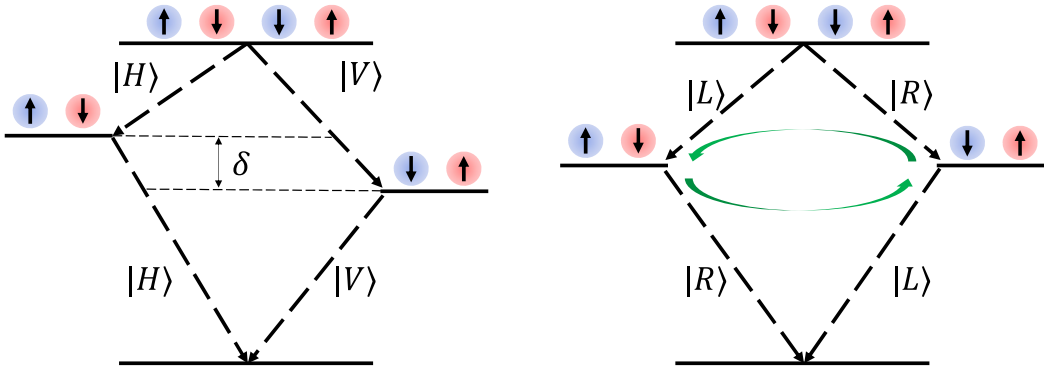

Figure 2.6: The XX-X cascade with a non-zero fine structure splitting. Depending on the basis you are observing, two different behaviours can be observed: in the linear basis, fine structure splitting presents itself as an energy difference which is proportional to δ between exciton states. In the circular basis, it presents itself as oscillating between two Bell states $|\Phi^+\rangle$ and $|\Psi^+\rangle$.

Typically, the fine structure splitting is an unwanted property for these QDs as it is known to degrade the degree of entanglement of the emitted photons because they provide a "which path" information [66, 67, 68]. However, in chapter 3 we will explore that, with fast enough detection equipment, it is possible to resolve the oscillating state in time. Resolving the state in time with fast detection equipment allows us to accurately reconstruct the density matrix of the state and mitigates the fine structure splitting's degradation of the entanglement fidelity. As evidence will show, the source in the presence of fine structure splitting still exhibit high degrees of entanglement consistent with state-of-the-art sources currently being tested today.

2.2.4 Nanowire Quantum Dots

So far we have only referred to the source as a nanowire quantum dot, without explaining what it is other than the generic properties of a QD. The nanowire is not part of the QD, i.e. it does not aid in the generation of photons. The nanowire itself acts as an aid in

[13] See section 1.3.2 for reference

photon collection. In this section, we will explore how the nanowire achieves this and the advantages of the nanowire environment over bulk QDs.

Photonic nanowire structures are cylindrical or hexagonal wires which can be fabricated from the bottom-up. This bottom up process is deterministic, meaning we can choose where inside the wire we want to place the QD. The structure has a wide base which tapers as you travel along the height of the wire after the QD has been placed. This taper allows for the enhanced directional coupling in the direction of the growth of the wire. This taper also results in the adiabatic expansion of the spatial mode of the strongly confined near field light as it leaves through the tapered top. This adiabatic expansion creates a highly directional Gaussian beam in the far field [69][14]. This structure is around several hundred nanometres at the base. These nanowire structures have large collection efficiencies up to 72% [70]. These nanowires, however, suffer from low visibility, likely due to charge noise of the nanowire, which can cause dephasing [1].

Growing a Nanowire

The nanowires are grown using a two-step growth process combining chemical beam epitaxy (CBE) with trimethylindium (TMI) and PH_3 and AsH_3 sources, and vapour-liquid-solid (VLS) growth method [50]. The nanowires are grown using a patterned SiO_2 mask which sits on top of the InP substrate, in which holes are etched into the SiO_2 to expose the InP substrate. Next, gold (Au) is placed in these holes, which will act as the catalyst for nanowire growth. This allows for the nanowires to be grown on predetermined positions. Next, TMI (indium source), and PH_3 (phosphorus source) are added to the chamber and the environment (temperature, pressure, vapour quantities) is kept at conditions to promote VLS growth of pure wurtzite (WZ) nanowires [50]. This happens because of supersaturation of the Au droplet (direct flux) which diffuses onto the substrate, depositing of vapour onto the sidewalls of the nanowire (direct sidewall flux), and indirect sidewall flux caused by scattering of vapour off of the SiO_2 covering the InP substrate. To incorporate the QD, a switching from PH_3 to As_3 vapour is done for a short time, around 3 seconds after 15 minutes of nanowire growth.

These bottom-up structures are generally polytypic, with alternating sections of zincblende (ZB) and WZ crystal phases along the length of the nanowire [50]. This alternating crystal phase cause stacking faults[15], which can cause background emission, i.e. multi-photon emission, due to charges trapped in these stacking fault [50]. If these stacking faults occur

[14] See chapter 4 for an in-depth explanation of how structures like the nanowire interact with light.

[15] Stacking faults are two-dimensional (planar) defects in the stacking planes of the crystalline materials.

in the vicinity of the QD, they can also contribute to charge noise, which can be a source of spectral diffusion [71]. Thus, there has been an effort to ensure that the nanowire is strictly one crystalline phase, which in the context of this thesis is WZ. WZ has a band gap energy higher than the emission of the QD, meaning the light will not be absorbed by the nanowire [53]. This allows for the nanowire structure to act as a dielectric media, similar to that of the materials mentioned in chapter 4. The taper along the length of the nanowire is a result of the finite diffusion length of the indium on the nanowire sidewall, which, based on the results from reference [72], is about 1 μm. Nanowires longer than $\approx$ 0.5 μm are slightly tapered, while shorter ones are uniform [72].

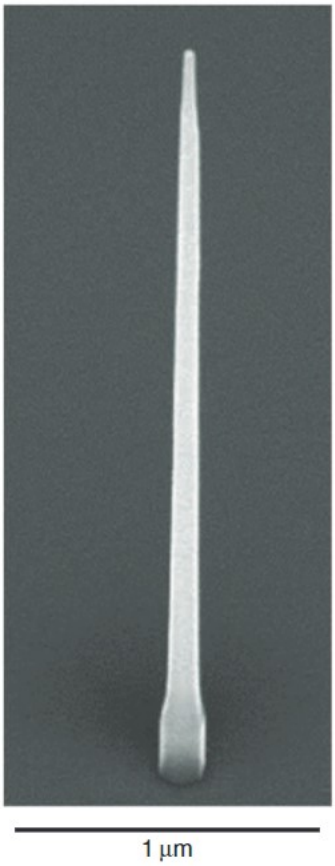

Figure 2.7: Scanning electron microscopy image of a tapered nanowire waveguide with embedded quantum dot 200 nm from nanowire base. Taken from reference [2] and reused under CC BY 4.0.

The goal of exploring these sources is to obtain an on-demand entangled photon source, shown in figure 2.8. The quality of these sources are determined by entanglement fidelity and pair extraction efficiency, which depends on a myriad of aspects associated with experimental conditions (excitation scheme, charge traps in vicinity, FSS, etc.) and internal and external efficiencies of the source (light coupling out of the nanowire, blinking, etc.). Deficiencies in these areas tend to limit the quality of the source, and the goal of this thesis is to explore how we can improve the quality of NWQDs shown in figure 2.8 to push them into the shaded on-demand region.

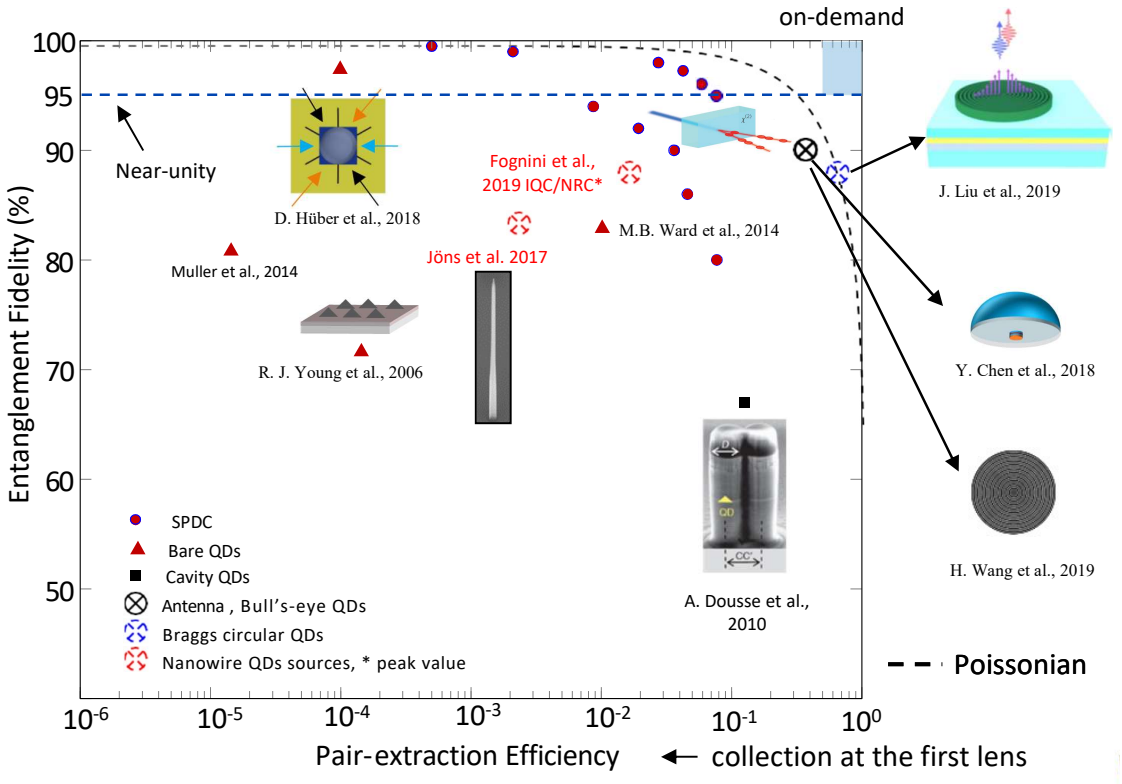

Figure 2.8: Road map towards an on-demand entangled photon source.

Chapter 3

Two Photon Excitation

Thus far we have referred to excitation as triggering events which, when performed, cause electrons to jump from the VB to the CB, leaving behind holes. This excitation event creates the XX-X cascade, making it possible to create the entangled photon pairs. There are two ways to do this: electrically [73, 74] or optically [2, 37, 75]. Electrically exciting the QD involves creating an electrical gate, such as a single electron pump or diode, to inject the charges into the appropriate energy levels inside the QD. Optical methods of exciting the QD involve using lasers tuned to the required wavelength or above the bandgap of the material surrounding the QD, so the electrons in the VB can absorb the photons. The energy absorbed from the photons causes the electrons to jump to the conduction band, thus creating the XX or X. In this section, we will explore different optical methods used to create the excitation event.

3.1 Excitation Schemes

There are a variety of optical methods we can use to drive excitation. These methods of optical excitation were created with the objective of populating the lowest energy state inside the QD, each with their benefits and drawbacks. These benefits and drawbacks refer to the quality of emission we get from the source, as they directly impact how the QD performs as a source of entangled photons[1]. Each excitation scheme uses a different optical transition within the QD when exciting charge carriers. In this section, I will describe each

[1]This refers to section 2.1 for properties of entangled photon sources.

excitation scheme and how it populates the QD with charge carriers and its impact on the quality of the QD emission.

To begin, we first need to distinguish between the types of excitation schemes, ideally the differences between "non-resonant," and "resonant" excitation schemes. Early work focused on non-resonant excitation schemes because of the ease of implementation of the method. The method involves generating charge carriers in the materials surrounding the NWQD (i.e. the nanowire) to relax via phonons into the s-shell of the NWQD to initiate the radiative recombination process [1]. Furthermore, these charge carriers generated using this scheme act via carrier-carrier scattering processes can act as sources of decoherence for subsequently emitted photons [1]. Ultimately, there are limitations placed on the indistinguishability of the photons produced by this excitation scheme due to the non-radiative relaxation processes charge carriers undergo before relaxing into the QD. This causes uncertainty in the emission process, increasing the emission timing jitter, which is a limiting factor for the aforementioned indistinguishability.

Resonant excitation schemes, however, address the radiative excitation levels (XX and X energy levels) of the NWQD directly. This scheme bypasses the need for charge carriers to be created inside the nanowire, thus eliminating a factor of dephasing. This method also allows for the generation of the XX and X states necessary for QIP applications mentioned in chapter 1.

3.1.1 Above-Bandgap

The first excitation scheme I will discuss will be the above-bandgap excitation (ABE) technique. ABE involves exciting electrons/holes in the wurtzite InP nanowire. The bandgap energy in the nanowire is higher than that of the QD, 1.49 eV, which would require a shorter excitation wavelength than 830 nm. The electrons/holes created through ABE need to make their way into the QD through interactions with lattice phonons. The electrons/holes lose energy through these interactions as they decay into the s-shell of the QD. To ensure the QD s-shell is always populated with a XX, repeated excitations are used to create the flow of charge carriers into the QD. Because of the abundance of charge carriers in the nanowire, relatively low excitation power is needed to populate the XX state in the QD compared to that of other excitation schemes, making it simpler to implement than other excitation schemes. Also, because the defects are dispersed randomly throughout the nanowire, there is no consistency in the energy levels of the charge carriers created. This allows us to use a wider bandwidth laser to excite as many charge carriers as possible to maximize the probability of XX state population, meaning there is no need for pulse

shaping techniques[2].

Although ABE is simpler than other excitation methods, one might believe this to be the ideal excitation scheme to use to excite the QD. However, the simplicity of this scheme also plays into its biggest disadvantages. ABE excites the defects in the nanowire to produce excess charge states in the nanowire. These excess charge states are physically within the vicinity of the QD, electric field fluctuations. The electric field fluctuations cause dephasing of the X spin with effective magnetic fields caused by electric fields through the spin-orbit coupling that can interact with the X spin [3]. In addition to entanglement degradation, these charge fluctuations also cause broadening of the emission wavelengths [76], which decreases indistinguishability [77, 78], and the increased probability of multi-photon emission.

An extra emission line (shown in figure 3.1) can be seen at wavelengths close to the XX and X. This is known as charged excitons, or trions (denoted as X^- or X^+), and are a result of extra charge carriers present during the X decay to the ground state. This occurs due to the excess of charge carriers from the ABE scheme and are created when either an electron (hole) decays into the X state after the XX has emitted. Either negative (positive) trions, X^- (X^+), are created depending on whether an electron (hole) is present.

With all of these downsides, ABE is not considered the ideal excitation scheme to produce entangled photon pairs with properties that correspond to the wish list established in section 2.1. However, ABE does have its advantages. For example, because of the low excitation power, this scheme can be used to identify bright QDs in sample arrays due to the higher probability of exciting charge carriers in the nanowire.

[2]See section 3.2.3 for pulse shaping techniques.

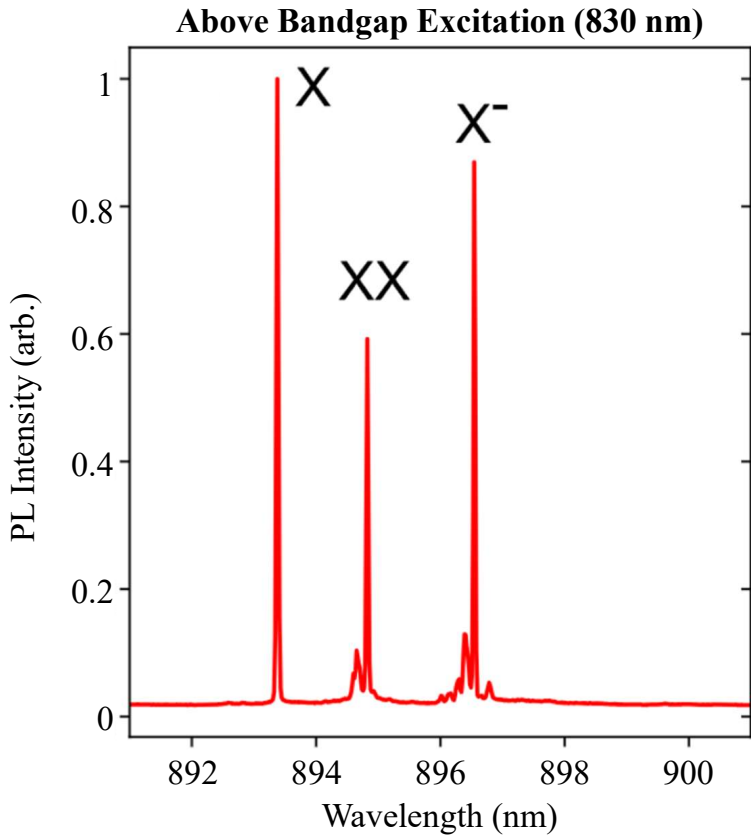

Figure 3.1: Emission spectrum of NWQD under above band excitation. Reused from reference [3], copyright 2019 by American Chemical Society (see Copyright Permission Forms 5).

3.1.2 Quasi-Resonant

The second method of excitation is called quasi-resonant excitation (QRE). Like ABE, which excites defect states in the nanowire and allows them to decay into the QD, QRE excites some donor/acceptor states in the nanowire and fills excess donor/acceptor states, causing increased stability in the electrical environment [3]. However, these charges can decay directly into the QD, as opposed to the ABE scheme where there is a "longer path" for charge carriers to reach the QD. These donor/acceptor states are closer in energy to the XX state in the QD, meaning that there will be less excess charges around the QD.

Being closer in energy to the QD, the wavelength used to excite the nanowire is longer, around 870 nm. At this wavelength, charge carriers are excited below the bandgap of the nanowire, greatly decreasing the number of charge carriers present around the QD. This decrease in charge carriers results in an environment which has higher electrical stability than that of the ABE scheme, potentially increasing photon indistinguishability. Less charge carriers also reduce the probability of re-excitation; re-exciting the XX state before the X state can decay to the ground state. Re-excitation results in multi-photon emission, which is undesirable for a single photon source.

With less free charge carriers, we see that the X^- trion emission is suppressed from the results of figures 3.1 to 3.2. However, the X^+ trion emission has increased, compared to that of the ABE scheme. An increase in the ratio of the XX-X emission compared to that of the X^- and X^+, indicating an increase in performance using QRE. However, despite the improvements, QRE still experiences some dephasing due to the excess charges in the environment, as seen by the presence of X^- and X^+ trions, as well as some multi-photon emission.

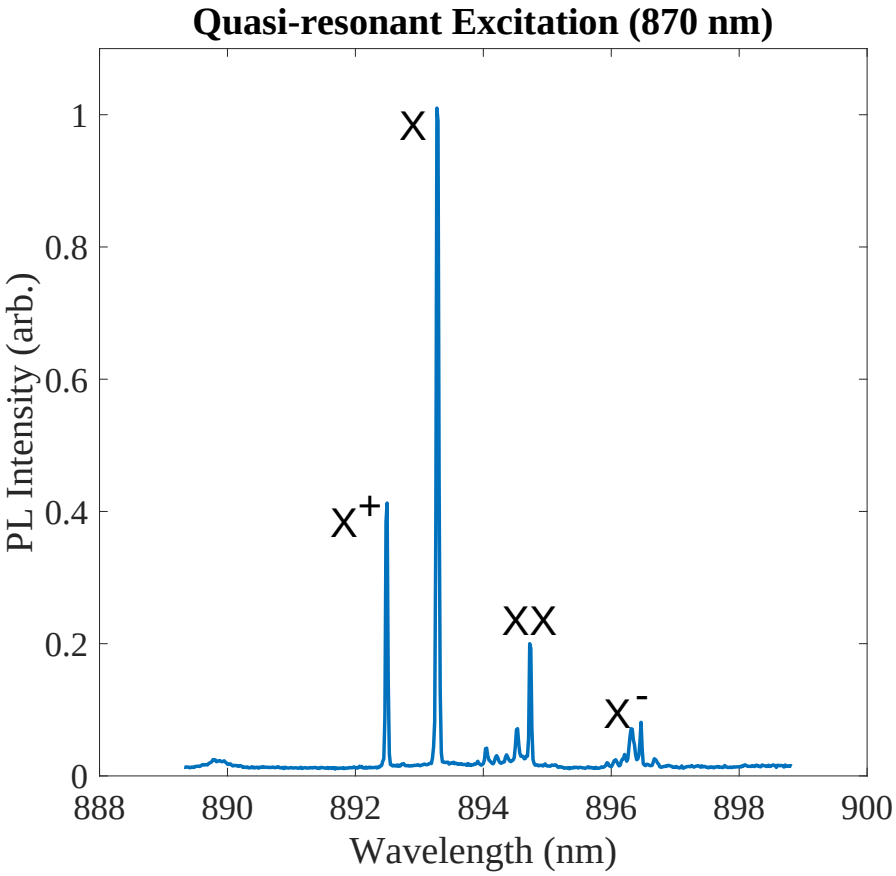

Figure 3.2: Emission spectrum of NWQD under quasi-resonant excitation at a laser power of 0.25 μW

3.1.3 Two-photon Resonant

Two-photon resonant excitation (TPRE), is an excitation technique which populates the XX state directly. The name, two-photon resonant excitation, follows from the absorption of two photons to populate the XX state directly, without the generation of free charges in the nanowire. The direct population of the XX state does not require those free charges to decay into the XX state, as they do with QRE and ABE [3]. It is for this reason that the emitted photons using this technique are of higher quality, exhibiting higher indistinguishability and single photon purity [1].

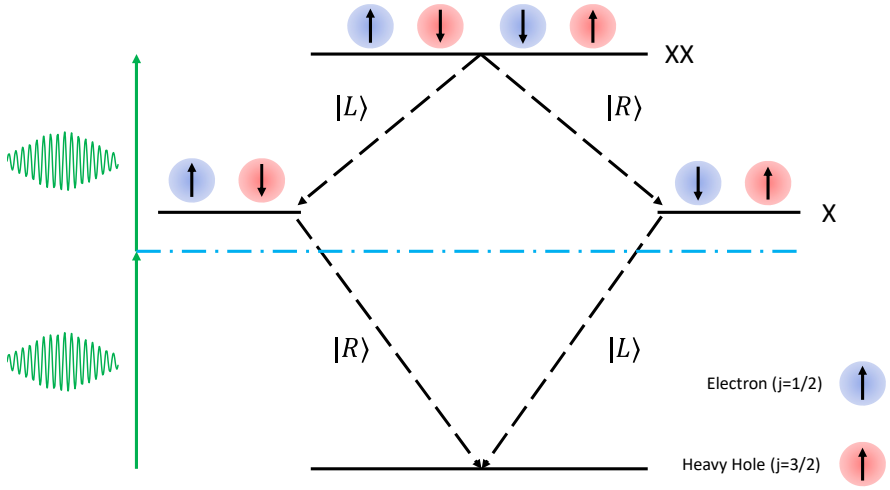

Figure 3.3: Visual representation of the TPRE process. Two photons are needed to reach the XX state due to conservation of angular momentum. The virtual intermediate level, depicted by a dashed blue line, represents the energy of one of the photons in this process.

The reason for the two photon absorption as opposed to a single photon of the appropriate energy is because of the optical selection rules, which states that the XX state has $j_z = 0$ and the photons have $j_z = \pm 1$. therefore, to directly populate the XX state, the laser pulse (which contains two photons) should be linearly polarized. This will satisfy the requirements of the photons being in a superposition of $|L\rangle$ and $|R\rangle$, having $j_z = +1$ and $j_z = -1$, respectively.

To fully understand the dynamics of TPRE, it's important to start from first principles, starting with the Hamiltonian of the form:

$$H = \frac{\hbar\Omega_1(t)}{2}(\sigma_{g,X} + \sigma^\dagger_{g,X}) + \frac{\hbar\Omega_2(t)}{2}(\sigma_{X,XX} + \sigma^\dagger_{X,XX}) + \hbar\sigma_{X,X}(\Delta_X - \Delta_{XX}) - 2\hbar\sigma_{XX,XX}\Delta_{XX} \tag{3.1}$$

where $\Omega_i(t)$ is the Rabi frequency of the driving field to either the XX or X state, $\sigma_{i,j} = |i\rangle\langle j|$ are transition operators from one state to another, Δ_X is the wavelength difference between the driving field and the X state, and Δ_{XX} is the wavelength difference between the driving field and the XX state [79]. If we perfectly couple to the XX state, making $\Delta_{XX} = 0$, the equation simplifies to:

$$H = \frac{\hbar\Omega(t)}{2}(\sigma_{g,X} + \sigma_{g,X}^{\dagger}) + \frac{\hbar\Omega(t)}{2}(\sigma_{X,XX} + \sigma_{X,XX}^{\dagger}) + \hbar\sigma_{X,X}\Delta_X \tag{3.2}$$

where $\Omega_1(t) = \Omega_2(t) = \Omega(t)$ for the two-photon absorption condition [61].

When the driving field is slightly off of resonance, there can be coupling of carriers to acoustic phonons, which can be a source of dephasing [80]. Because of the presence of phonons and their influence on the energy levels of the QD, the probability of populating the XX state is dependent on temperature. As temperature increases, the amount of phonons in the crystalline structure also increases, and thus decreases the probability of populating the XX state. The strength of phonon-carrier coupling is also dependent on the field intensity. For field intensities higher than $\Omega(t) > \pi$, the probability of populating the XX state is decreased [80]. However, with the extra energy present in the system, states are created around the QD s-shell which can also populate the XX state. This process is an incoherent process called phonon-assisted two-photon excitation (PATPRE), and can also be used to populate the XX state, and gets better with stronger phonon-carrier coupling [81]. However, in this work, we will only focus on TPRE. True TPRE requires temperature control of the QD environment, as well as maintaining a field intensity of $\Omega(t) = \pi$. This will ensure maximum probability of populating the XX state, while providing high quality photons which are indistinguishable, pure, and on-demand.

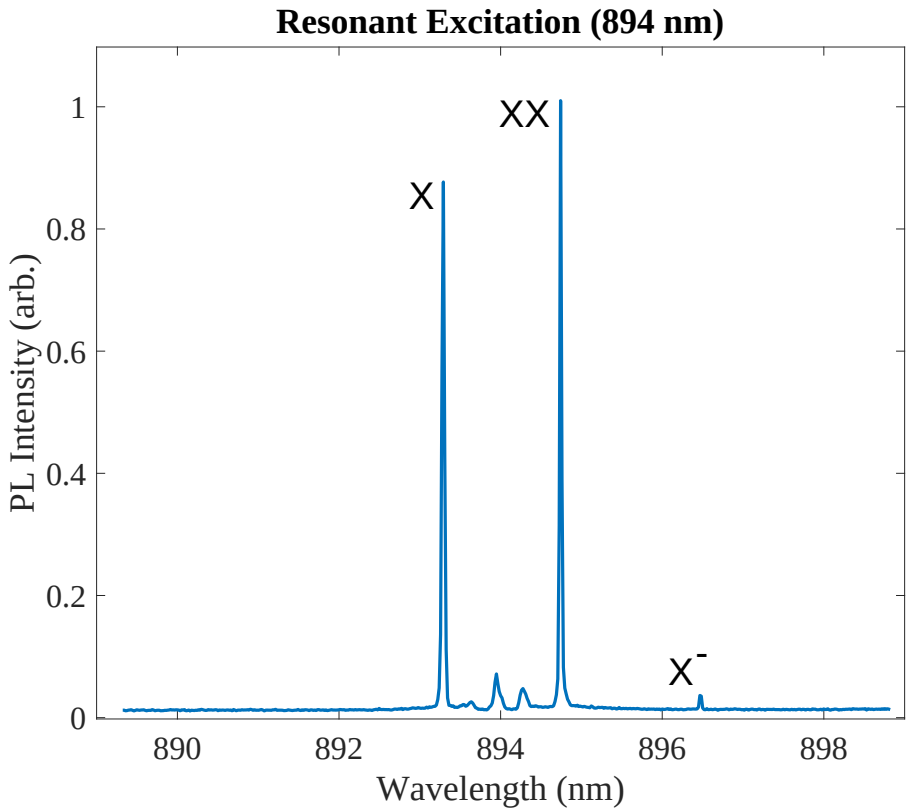

Figure 3.4: Emission spectrum of NWQD under two-photon resonant excitation. One can see an elimination of the X^+ and large suppression of the X^- compared to that of the quasi-resonant scheme. The peaks between the X and XX is laser leakage, which was unable to be filtered before entering the spectrometer.

3.2 Experimental Setup for Resonant Excitation

With the theory behind TPRE explained, the next step is to translate this theory into practice with equipment available to us in an optics lab setting. The key is understanding how these pieces of equipment work and to use that knowledge to achieve some desired functionality in some section of the experiment. To begin, we first need to list the components we have, starting with the source, followed by passive optical components.

3.2.1 Pulsed Laser Source

The laser which is used in the tomography setup is the Mira900p, which converts a continuous-wave (CW) laser into picosecond laser pulses using a cavity. The continuous wave laser enters the Mira900p, where a number of mirrors direct the light through the cavity and gain medium. The light is then reflected into the cavity, through the gain medium, where it can interfere with incoming CW light. The interference creates a standing wave inside the cavity. By adjusting the position of key mirrors inside the cavity, a sech^2 shaped pulse can be constructed[3]. The pulsed light is then focused using the gain medium, which is a Titanium-Sapphire crystal, by means of the Kerr-effect. The Kerr-effect refers to the non-linear property of some media which interacts differently to light of varying intensities. The Kerr-effect in this instance focuses light of higher intensity to a smaller spot-size than light of lower intensity. The result is that the pulses – which are created through constructive interference – are of higher intensity and are therefore focused to a smaller spot-size than the less intense CW laser. At the output of the Mira900p is a slit in which both the horizontal position and width of the opening can be adjusted. By positioning the slit at the centre of the beam and opening it to about half the beam diameter, we can ensure that only the pulsed portion of the beam exits the Mira900p.

[3] According to the Mira900p manual, auto-correlation traces for Mira Optima pulses suggest that the pulses are best described by a sech^2 function.

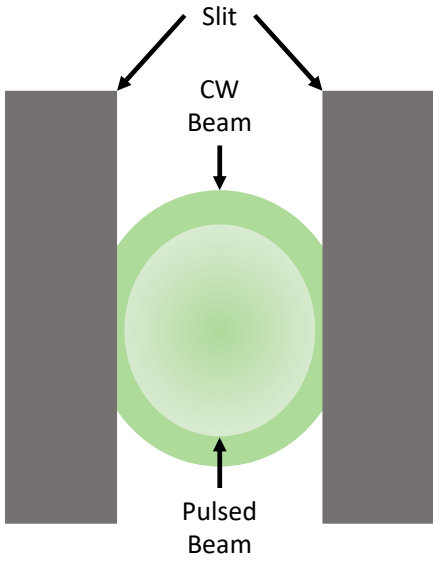

Figure 3.5: Cross-section of Mirs900p slit apparatus under operation. The slit opened as to block the larger diameter CW beam and allow the pulsed beam to pass through.

3.2.2 Passive Components

With the source established, next we will discuss the passive components needed to perform quantum state tomography – a method of reconstructing the density matrix of the source[4]. As we build upon the theory of these components, it will become clear as to why we use them, how they affect photons, and how they fit into the overall setup for reconstructing the density matrix.

Beam splitter

The first component which will be discussed is the beam splitter. Beam splitters consist of two triangular prisms, made from either glass or plastic, glued together at their base. The interface, which is responsible for transmitting/reflecting the incoming light, can be coated with either resin (which is used to glue the two prisms together) or a partially transparent coating of metal.

[4]Tomography will be fully explained in section 3.3.

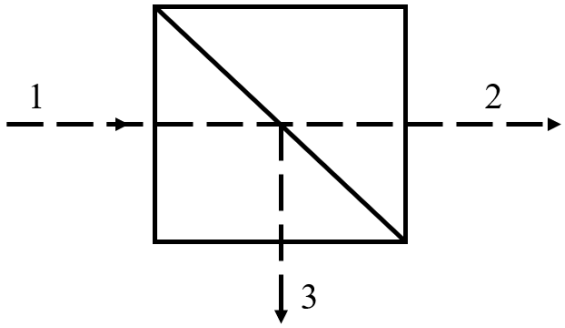

Figure 3.6: Schematic of a beam splitter. Incoming light (1) enters the splitter and is both transmitted (2) and reflected (3). The amount of light that is transmitted/reflected depends on the splitting ratio. For example, a 50:50 beam splitter will transmit/reflect equal amounts of light.

Mathematically, beam splitters can be described by analyzing what happens as an electric field interacts with it, i.e., how the beam splitter transmits/reflects the light. To start, it's useful to represent the electric field and beam splitter in matrix form.

$$\mathbf{E}_{out} = \begin{bmatrix} E_c \\ E_d \end{bmatrix} = \begin{bmatrix} r_{ac} & t_{bc} \\ t_{ad} & r_{bd} \end{bmatrix} \begin{bmatrix} E_a \\ E_b \end{bmatrix} \tag{3.3}$$

where the elements of the 2×2 matrix represent the transmitted/reflected components of the transfer matrix for the beam splitter, E_a and E_b represent the components of the input field, and E_c and E_d represent the components of the output field. Following the conservation of energy, and assuming the beam splitter is lossless, the magnitude of the input field components equal the magnitude of the output field components, i.e.

$$|E_c|^2 + |E_d|^2 = |E_a|^2 + |E_b|^2. \tag{3.4}$$

If we focus the input field to one port of the beam splitter, i.e. $E_b = 0$, this implies

$$|r_{ac}|^2 + |t_{ad}|^2 = 1 \tag{3.5}$$

and when $E_a = 0$ implies

$$|r_{bd}|^2 + |t_{bc}|^2 = 1. \tag{3.6}$$

If we expand this to include results when both E_a and E_b are non-zero, we have

$$r_{ac}t^*_{bc} + t_{ad}r^*_{bd} = 0 \tag{3.7}$$

where $r_{ac} = |r_{ac}|e^{i\phi_{ac}}$. By re-writing the previous equations in this manner, we have

$$|r_{ac}||t_{bc}|e^{i(\phi_{ac}-\phi_{bc})} + |t_{ad}||r_{bd}|e^{i(\phi_{ad}-\phi_{bd})} = 0. \tag{3.8}$$

For this to be true, $\phi_{ad}-\phi_{bd}+\phi_{bc}-\phi_{ac} = \pi$. With constraints on the phase and magnitudes of the fields, we can re-write $|r_{ac}| = |r_{bd}| = R$ and $|t_{ad}| = |t_{bc}| = T$, and thus the transfer matrix for the beam splitter becomes

$$\begin{bmatrix} Re^{i\phi_{ac}} & Te^{i\phi_{bc}} \\ Te^{i\phi_{ad}} & Re^{i\phi_{bd}} \end{bmatrix}. \tag{3.9}$$

Finally, we want to express the beamsplitter in a form which usefully describes the output magnitude and phase; to allow us to relate both the transmission/reflection ratio and the induced phase change the beam splitter has on the light. Particularly, we want a relationship between R and T which satisfies $R^2 + T^2 = 1$. If we define $T = \cos(\theta)$, $R = \sin(\theta)$, and $\theta = \tan^{-1}(R/T)$, and substitute the phase parameters $\phi_T = \frac{1}{2}(\phi_{ad} - \phi_{bc})$, $\phi_R = \frac{1}{2}(\phi_{ac}-\phi_{bd}+\pi)$, and $\phi_0 = \frac{1}{2}(\phi_{ad}+\phi_{bc})$ the full expression of the beam splitter transfer matrix [82] becomes

$$BS(\theta, \phi_0, \phi_T, \phi_R) = e^{i\phi_0}\begin{bmatrix} \sin(\theta)e^{i\phi_R} & \cos(\theta)e^{-i\phi_T} \\ \cos(\theta)e^{i\phi_T} & -\sin(\theta)e^{-i\phi_R} \end{bmatrix}. \tag{3.10}$$

If we set $\theta = \frac{\pi}{4}$ and $\phi_0 = \phi_T = \phi_R = 0$, we get a 50:50 beam splitter with the transformation matrix being

$$BS(\frac{\pi}{4}, 0, 0, 0) = \frac{1}{\sqrt{2}}\begin{bmatrix} 1 & 1 \\ 1 & -1 \end{bmatrix} \tag{3.11}$$

and if $\theta = \frac{\pi}{4}$ and $\phi_0 = \frac{\pi}{2}$, $\phi_R = -\frac{\pi}{2}$, and $\phi_T = 0$, we have

$$BS(\frac{\pi}{4}, \frac{\pi}{2}, 0, -\frac{\pi}{2}) = \frac{1}{\sqrt{2}}\begin{bmatrix} 1 & i \\ i & 1 \end{bmatrix}. \tag{3.12}$$

Other representations of beam splitters can be written by expressing them as other versions of unitary groups. One such example is the SU(2) group, in which the general expression for the beam splitter can be written as

$$BS(\theta, \phi) = \begin{bmatrix} \cos(\theta) & -e^{i\phi}\sin(\theta) \\ e^{-i\phi}\sin(\theta) & cos(\theta) \end{bmatrix} \tag{3.13}$$

where, in this instance, ϕ is some general phase.

Beam splitters can also be polarization dependent. This dependence manifests itself by selecting either $|H\rangle$ or $|V\rangle$ polarized light and deterministically sending them through different ports of the beam splitter. For example, if a beam containing equal portions $|H\rangle$ or $|V\rangle$ polarized light, the beam splitter represented in figure 3.6 will transmit $|H\rangle$ and reflect $|V\rangle$, i.e. sending $|H\rangle$ through port 2 and $|V\rangle$ through port 3.

Half Waveplate

Half waveplates (HWP) are used to change the polarization of light from one linear polarization to another or from one circular polarization to another. It does this by means of birefringence. Birefringence is a property of some materials which splits light rays into "ordinary" and "extraordinary" (parallel and perpendicular) rays, which are orthogonal to each other.

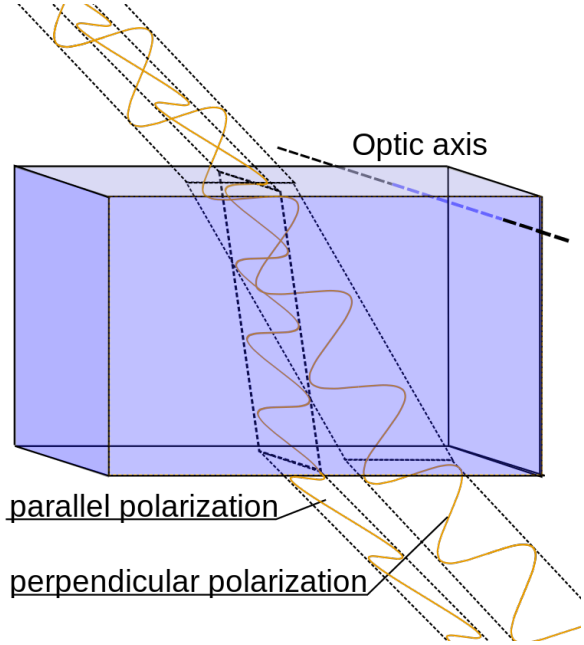

Figure 3.7: Incoming unpolarized passing through a birefringent material and being decomposed into its orthogonal components. Figure by Mikael Häggström, licensed under CC BY 4.0.

This implies that this material has different refractive indices for different polarizations. Polarizations which experience a smaller refractive index are known as "fast rays" and polarizations which experience a larger refractive index are "slow rays." Waveplates are constructed from this birefringent material, with a "fast axis" and "slow axis." This refers to the refractive index light will observe when passing through the waveplate. Light oriented along the slow axis will experience a higher refractive index, and therefore experience more polarization shifting.

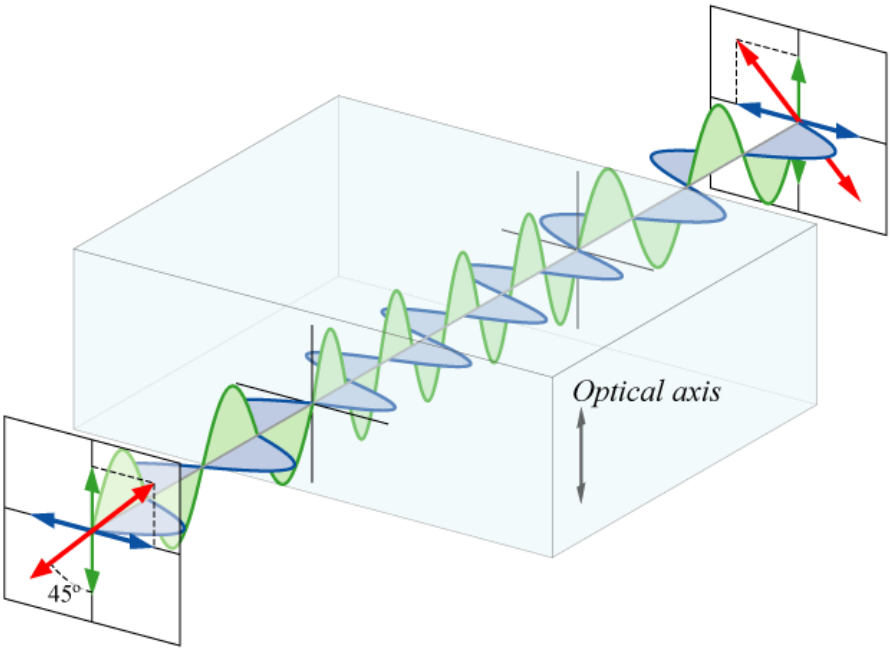

Figure 3.8: Schematic of a half waveplate. As light polarized along the red axis passes through the birefringent crystal, until upon exiting, where the polarization has been changed by 90°. Figure by Bob Mellish, licensed under CC BY 4.0.

This is a unitary transformation, meaning it's lossless, and the magnitude of the vector is maintained along the Bloch sphere. The unitary matrix representing the effect a half waveplate has on the state is

$$U_{HWP}(\theta) = \begin{bmatrix} \cos(2\theta) & -\sin(2\theta) \\ -\sin(2\theta) & -\cos(2\theta) \end{bmatrix} \tag{3.14}$$

where θ is the angle of the waveplate with respect to the vertical axis [83]. Half waveplates alone do not possess the ability to reach everywhere on the Bloch sphere, thus another device is needed.

Quarter Waveplate

Quarter waveplates (QWP) are used to change the polarization of light from linear to circular and vice versa. It works on the same principle as half waveplates: birefringence,

and fast and slow axis, but also inducing a phase shift. This action is also unitary and has a matrix of the form

$$U_{QWP}(\theta) = \frac{1}{\sqrt{2}} \begin{bmatrix} i - \cos(2\theta) & \sin(2\theta) \\ \sin(2\theta) & i + \cos(2\theta) \end{bmatrix} \tag{3.15}$$

where θ is the angle of the waveplate with respect to the vertical axis [83]. Cascading the HWQ with the QWP allows access to anywhere on the Bloch sphere.

Polarizer

Polarizers are used to transmit light of a particular polarization, while suppressing/reflecting light of other polarizations. Polarizing filters used in the experiment are a circular disk with a nanoparticle linear film deposited on it. There are transmission axes placed on the film, indicating the orientation needed to pass $|H\rangle$ polarized light. When the $|H\rangle$ light is aligned with the transmission axis, only $|H\rangle$ polarized light will pass through and all other light will be suppressed.

3.2.3 Resonant Excitation Scheme using a 4-f Pulse Shaper

To perform TPRE, a narrow band of pulsed light must be sent to the QD to maximize the likelihood of populating the XX state. How this narrow band of light is created is by sending pulsed light, which consists of a higher bandwidth than needed, through a 4-f pulse shaper.

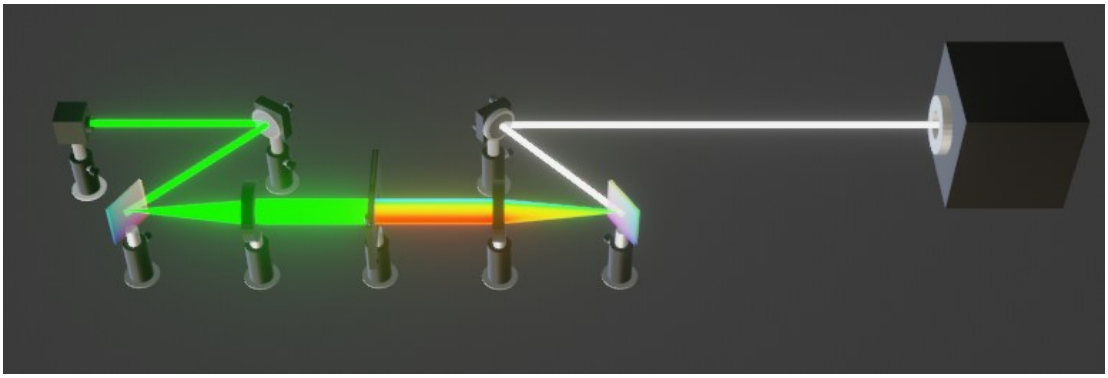

Figure 3.9: Schematic of a half 4-f pulse shaper. Light exits the Mira900p with some broad bandwidth. It is then directed to a grating which separates the light in space, depending on the wavelength; it decomposes the light into its individual spectral components. The light is then collimated and sent through a slit, which physically blocks some light from getting through. From this, the slit allows for the selecting of a narrow band of light, which is then focused back onto the grating and sent to the NWQD.

The narrow band of light must be less than the XX binding energy, ΔE_b, to avoid exciting the X state directly. The laser is tuned to about half the average wavelength of the XX and X photons, as indicated by the blue dotted line in figure 3.3. The FWHM of the linewidth of the pulsed laser directly out of the Mira900p was found to be about 0.41 nm, which means that it is too large to be used in the TPRE setup.

To decrease the bandwidth of the pulse from the Mira900p, a 4-f pulse shaper is used. The 4-f pulse shaper consists of a Newport 10HG1200-800-1 reflection grating to separate the light into its frequency components in space. A Thorlabs LA1417-B lens is placed at a focal length distance of 15 cm from the grating, which is also mounted on transnational stages for fine adjustments. The first lens focuses the split light on a Newport SV-0.5 adjustable width slit which it can then select small bandwidths of light, which has been separated by the grating. With the narrow bandwidth of about 0.07 nm selected, the second lens focuses the light onto the second reflection grating, recombining the beam, where it is then sent to the NWQD. The gratings are placed at exactly the same distance from their respective lenses, and are oriented at the same angle to reduce chirp[5], which reduces the population efficiency of the XX state [84]. The narrow pulse will now fit between the XX and X emission lines without leaking into them.

[5]Chirp is the linear increase/decrease in frequency with time.

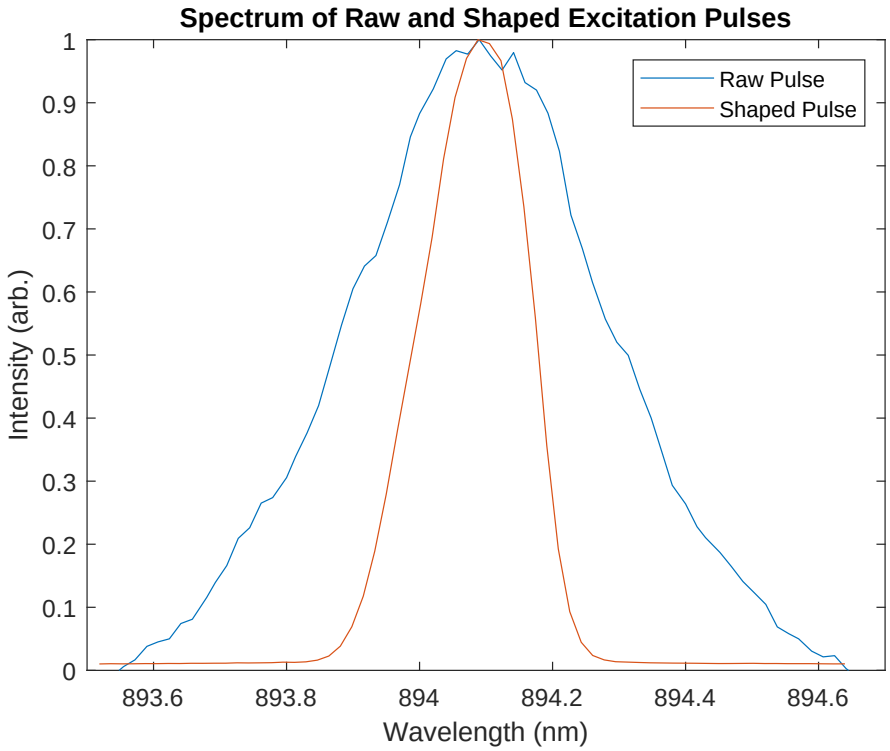

Figure 3.10: Spectrum of the raw pulse coming from the Mira900p and the shaped pulse exiting the 4-f pulse shaper. One can see an immediate reduction in the bandwidth of the shaped pulse. Both pulses have been normalized to the same value for clarity.

3.3 Tomography Using Free Space Optics and Single Photon Detectors

Tomography is a technique used to reconstruct the density matrix of a source. The goal is to determine the state of the emitted photons by projecting them onto different orthogonal states on the Poincaré sphere. The methods which are used to determine the form of the density matrix are found in [83]. The formulation of the density matrix uses measurements, combined with a "likelihood function" and standard optimization techniques, to find an optimum set of variables to best describe the most likely physical density matrix. In other words, the raw measurements are used to reconstruct a density matrix, then optimization techniques find parameters for which the likelihood function is maximized. This will return

a density matrix which is physically possible[6] and best represents the quantum state.

The density matrix can be constructed from some general matrix $\hat{T}(t)$:

$$\hat{T}(t) = \begin{bmatrix} t_1 & 0 & 0 & 0 \\ t_5 + it_6 & t_2 & 0 & 0 \\ t_{11} + it_{12} & t_7 + it_8 & t_3 & 0 \\ t_{15} + it_{16} & t_{13} + it_{14} & t_9 + it_{10} & t_4 \end{bmatrix} \tag{3.16}$$

where $t = t_i$ are a set of 16 real parameters, where 15 of them are independent. From these parameters, the density matrix can be written as

$$\hat{\rho}(t) = \frac{\hat{T}^\dagger(t)\hat{T}(t)}{Tr[\hat{T}^\dagger(t)\hat{T}(t)]}. \tag{3.17}$$

However, it is still unclear HOW we find these parameters in an experimental setting. To see how this is done, we need to understand how the measurements are done.

The setup for the TPRE experiment can be found in figure 3.11.

[6] See 1.3.1 for properties of the density matrix.

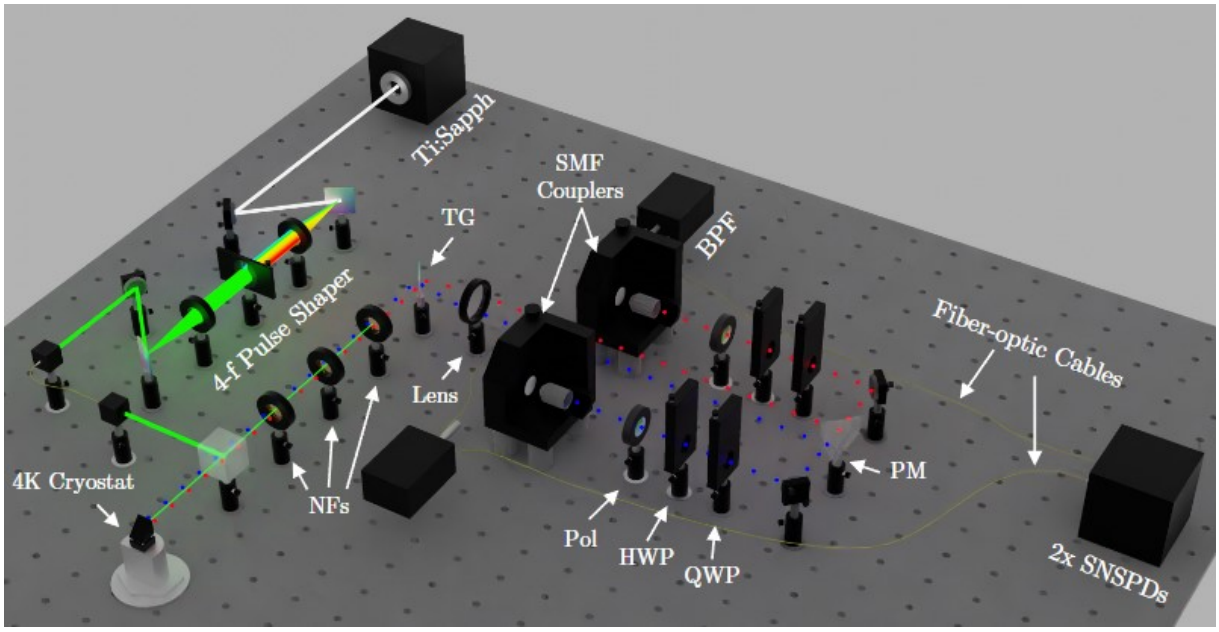

Figure 3.11: Schematic of the TPRE setup. Light emitted from the Mira900p is fed through a 4-f pulse shaper, where a narrow band of light is selected. It is then sent to the NWQD, which is held inside an AttoDry 900 cryostat, holding a constant temperature of about 4K. The NWQD emits a XX and X photon, which are sent through 3 notch filters to eliminate the laser. The XX and X are then separated in space using a transmission grating and directed to different paths via a prism. the photons are then sent through a HWP, QWP, and H-oriented polarizer, where it is then coupled to fibre and sent to the detection systems.

It can be shown that by applying the unitaries from the HWP and QWP to the state $|\psi\rangle$, we get

$$\hat{U}_{HWP}(\theta)\hat{U}_{QWP}(\phi)\,|\psi\rangle = a(\theta,\phi)\,|H\rangle + b(\theta,\phi)\,|V\rangle \tag{3.18}$$

where a and b are complex valued functions of θ and ϕ. In this instance, θ and ϕ allow us to project onto any reference linear polarization state, i.e. $|H\rangle$, which will match the orientation of the polarizer. After calibrating both the HWP and QWP to only pass $|H\rangle$ polarized light, it can be shown that for certain values of θ and ϕ, we can project $|H\rangle$ polarized light onto any of the states defined in section 1.2.1.

To ensure the swift and smooth rotation of the HWP and QWP, Zaber X-RSW60A rotary

$\|\psi\rangle$	θ	ϕ
$\|H\rangle$	0°	0°
$\|V\rangle$	45°	0°
$\|D\rangle$	22.5°	-45°
$\|A\rangle$	-22.5°	-45°
$\|R\rangle$	0°	-45°
$\|L\rangle$	-22.5°	0°

Table 3.1: Set of angles for each single-qubit projection measurement, where θ and ϕ represent the angles of the HWP and QWP, respectively.

stages were used. These stages are fully programmable and can integrate with Python packages from a desktop computer. The HWP was a Casix WPA1215-$\lambda/2$, the QWP was a Casix WPA1215-$\lambda/4$, and the polarizer was a LPNIRE100-B.

3.3.1 Single-photon Avalanche Diode Detectors

With the free space optics established, the final aspect of completing a TPRE experiment is the detection system. Detection systems are used to detect photons, in conjunction with correlation electronics to determine the photon statistics. In conjunction with the passive optics used to project photons onto the different orthogonal states and passing them through a polarizer, there are statistics which the entangled photons should follow. These statistics govern whether a photon, and its entangled counterpart, should be measured and, due to the XX and X lifetimes, should be correlated in time.

One of the devices we use to detect these photons is the single-photon avalanche diode detector, or SPAD. SPADs are a type of photodetector[7] where a high reverse bias voltage is applied. This high reverse bias voltage exceeds the breakdown voltage of the p-n junction, causing any charge carriers injected into the depletion layer (from absorbing a photon) to trigger a self-sustaining avalanche. This response is known as an avalanche current[8]. When an avalanche current is detected, the SPAD must be reset back to operation conditions

[7] A p-n junction that can be illuminated by EM radiation.

[8] Avalanche current is an electric current multiplication effect which can allow for large currents to be generated, typically in insulators or semiconductors. Like the name suggests, it can start out small and gain current as time progresses. In SPADs, this allows for small currents created by single photons via the photoelectric effect to generate larger currents which can be measured using conventional, albeit sensitive, measurement devices.

through the use of a quenching circuit. Once the SPAD is reset, it is ready to detect another photon.

The detection systems are not perfect in how they count photons. There are physical restraints to these systems which limit their accuracy, thus creating a physical limit to the photon statistics of the NWQD which can be inferred from the SPADs. These limitations are linked to the physical properties of the physics of the device, which are:

- Timing jitter — Fluctuations of the temporal correlation between photon detection and the generation of the output signal. The FWHM of the timing jitter of the detection system is 488 ± 1 ps.
- Dark counts — False detections from fluctuations in the detection system. These occur when there is no light present, and occur at an average frequency of 34 ± 18 and 306 ± 51 Hz for each individual detector, respectively.
- Efficiency — The amount of loss for a detector. It is assumed that the efficiency of both detectors are the same.

These SPADs, upon detecting a photon, send a signal to a PicoHarp300 time tagger, which creates a histogram as a function of time delay between photon detection events. It works by correlating the detected photon between two SPADs, with which the PicoHarp300 has a timing resolution of 10 ps. This will allow us to determine the photon statistics of the entangled photons from the source, which will then build the density matrix to determine the degree of entanglement. However, due to the limitations of the SPADs, we are not able to gain an accurate picture of the entanglement. Because the timing resolution is comparable to the period of the FSS ($T_s = \frac{\hbar}{\delta} = 1.26$ ns), there is a blurring effect due to phase averaging of the state [37]. This is because the oscillating state, which can be represented as

$$|\psi\rangle = \frac{1}{\sqrt{2}}(|HH\rangle + e^{\frac{i\delta\tau}{\hbar}}|VV\rangle) \tag{3.19}$$

is a function of τ and δ, which is the time delay between the XX and X emission times and the energy of the FSS, respectively. Larger timing resolutions (on the order of the FSS oscillation period, T_s) will result in an inability to distinguish the phase relationship between $|HH\rangle$ and $|VV\rangle$, which is what causes the blurring effect. To construct a more accurate representation of the time evolving state, we need detection devices with a timing resolution much smaller than the FSS oscillation period [37].

3.3.2 Superconducting Nanowire Single Photon Detectors

Superconducting Nanowire Single Photon Detectors (SNSPDs) are devices which are extremely efficient at detecting single photons. In contrast with their SPAD counterparts, SNSPDs use the property of superconductivity to detect photons. This process is extremely efficient, and allows for a more accurate reconstruction of the density matrix of the NWQD source.

These detectors work by cooling a meandering nanowire film down to just below the critical temperature[9], at around 2.5 K. A bias current just below the critical current is applied, so that when a photon is absorbed by the nanowire film, the superconductivity is broken. This is due to the increase in temperature caused by the absorption of the photon. This results in an extremely sensitive detection system, far exceeding that of the SPAD.

The SNSPDs used in this experiment were from Single Quantum, boasting the lowest timing jitter, below 20 ps [37]. Due to the steady state of the detection system, the dark counts can also be extremely low. Under optimal conditions, the dark counts can be as low as 1 ± 1 Hz, which far exceeds the SPAD performance. This will reduce the probability of a false detection event, assuring an accurate depiction of the sources' emission.

3.4 Results

With the entire setup, from the NWQD source, excitation method, passive optics, and detectors, the tomography setup is complete. We have fully explained how these building blocks have come together, and are finally ready to perform the experiment. In this section, an over-complete[10] quantum state tomography was performed. This was to ensure that the density matrix was reconstructed as accurate as possible. Through this over-complete measurement, the instantaneous density matrix was reconstructed. The term instantaneous refers to a very short time window, at around 50 ps.

The objective of the results are to determine the quality of the NWQD source, and how the measurement apparatus affects the measured entanglement fidelity. The issues with these results in the past is that there were the detection systems' inability to resolve the state of the emitted photons in time. There was significant blurring of the state due to the large timing jitter and high dark count of the detectors [37, 61, 3]. In the following sections,

[9] Critical temperature refers to the temperature at which a material becomes a superconductor.

[10] 36 different time-resolved coincidence measurements were performed, as opposed to the 16 explained in section 3.3.

we will explore the results and how they differ depending on the measurement devices used, and that the FSS is not a limiting factor for LOQC protocols when the oscillating state can be resolved in time [37].

3.4.1 Rabi Oscillations

Rabi oscillations arise from resonantly populating the excited state of a two-level system. The population of the excited state is a function of pulse area, or power, of the excitation pulse. As referenced in equation 3.2, for pulse powers greater than π, the probability of populating the excited state decreases. This becomes apparent when we treat the pulse as a perturbation and solving for the eigenstates of a Hamiltonian associated with a small dipole (hydrogen atom). This is a valid assumption because the pulse's wavelength is much larger than that of the size of the QD. The Hamiltonian has the form of

$$\hat{\mathcal{H}} = \hat{H}_0 + \hat{V}(t) \tag{3.20}$$

where $\hat{V}(t) = e\mathbf{r} \cdot \mathbf{E}_0 \cos(\omega t)$ represents the external laser field interacting with the QD. Solving for the eigenstates for a two-level system, we have a state that represents the wave-function for a two-level system:

$$\Psi(\mathbf{r}, t) = c_1(t)e^{-i\omega_1 t} |1\rangle + c_2(t)e^{-i\omega_2 t} |2\rangle \tag{3.21}$$

where $c_1(t)$ and $c_2(t)$ are time-dependent coefficients relating the probability of being in either the ground/excited state, respectively. Plugging this state into the Schrödinger equation and taking the inner product, we have a relationship between the time derivatives of these coefficients and the transition:

$$i\dot{c}_1(t) = \frac{c_2(t)\cos(\omega t)}{\hbar} \langle 1| e\mathbf{r} \cdot \mathbf{E}_0 |2\rangle e^{i\omega_0 t} \tag{3.22}$$

$$i\dot{c}_2(t) = \frac{c_1(t)\cos(\omega t)}{\hbar} \langle 2| e\mathbf{r} \cdot \mathbf{E}_0 |1\rangle e^{-i\omega_0 t} \tag{3.23}$$

where the spherical symmetry of the hydrogen atom assumed earlier means that the diagonal terms of the matrix will be 0. If we define $\Omega := \Omega_{i,j} = \frac{\langle i|e\mathbf{r}\cdot\mathbf{E}_0|j\rangle}{\hbar}$ is the "Rabi frequency".

By rewriting the equations in the rotating frame, and neglecting the fast oscillating terms[11] allows us to simplify the differential equations to

$$i\dot{c}_1(t) = \frac{\Omega c_2}{2} e^{i\Delta t} \tag{3.24}$$

$$i\dot{c}_2(t) = \frac{\Omega^* c_1}{2} e^{-i\Delta t} \tag{3.25}$$

where $\Delta = \omega - \omega_0$ where ω is the frequency of the driving field and ω_0 is the frequency which is required to populate the excited state. Because of this, the term Δ is known as the detuning parameter, and describes how far away from resonance the driving field is. Finally, if we are assuming that time starts at $t = 0$ and the state is originally in the ground state, this allows us to describe, in time, the population of the excited state. In other words,

$$|c_2(t)|^2 = \frac{\Omega^2}{\Omega^2 + \Delta^2} \sin^2\left(\frac{\sqrt{\Omega^2 + \Delta^2}t}{2}\right) \tag{3.26}$$

thus fully explaining the oscillating behaviour of Rabi oscillations. Rabi oscillations are crucial to determining whether we are resonantly driving the system, and therefore is an important result from the experiment.

[11] This is known as the Secular approximation, where the fast oscillating terms average out to 0, meaning we can neglect the $\omega + \omega_0$ terms.

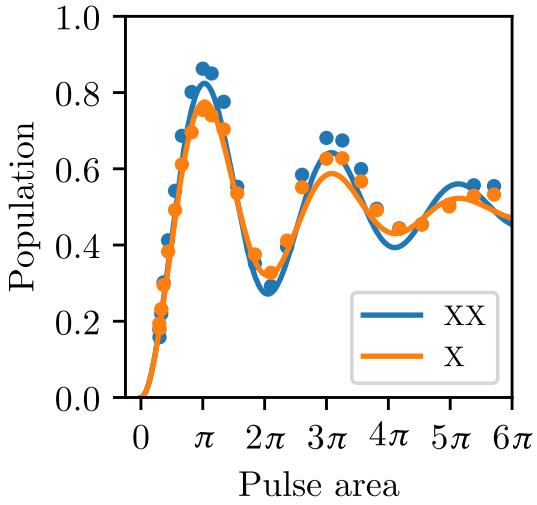

Figure 3.12: Rabi oscillations measured as a function of pulse area (power).

As alluded to in equation 3.26 and section 3.1.3, the maximum population occurs at the first π pulse and, due to increasing interactions with X-phonons, reduce the probability of state population for pulse areas larger than π [85]. It becomes clear in figure 3.12 that this is the case, as the population peaks at the π power and gradually decrease for odd π-integer, i.e., $(2m+1)\pi$, values of power. This confirms that the source is resonantly excited, with differences between the population of the XX and X photons can be attributed to loss in the system.

3.4.2 Single Photon Purity

Single photon purity is another property which describes the quality of a single photon source. The applications which require single photon sources to be highly pure, such as quantum key distribution, rely on only the desired qubits being sent, when you want to send them. Multi-photon emission can lead to undesirable outcomes, such as eavesdropping, which can steal information. Because TPRE excites the XX level directly, there are no excess charges created around the QD inside the nanowire or at higher energies. Therefore, there is a minimal chance of re-exciting the XX energy level under TPRE. To quantify the single photon purity of the source, a Hanbury-Brown-Twiss (HBT) experiment was carried out for both the XX and X photons.

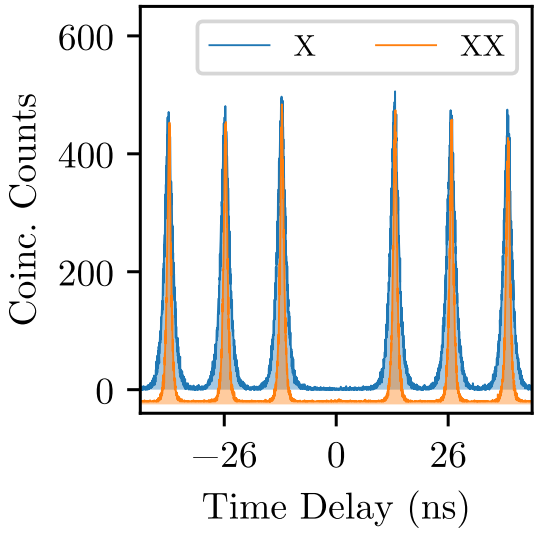

Figure 3.13: Measured XX and X HBT auto-correlation experiment as a function of time delay, τ, under resonant excitation.

The HBT experiment correlates the incoming photons from an emission line (XX or X) with subsequent photons as a function of time delay, τ. There should be one XX and one X photon per excitation pulse, which is quantified by the $g^{(2)}(\tau)$ measurement, as laid out in section 2.1.3. The peaks are occurring at $\tau = 13.2$ ns intervals, which are from correlations between photons from subsequent pulses, occurring every 13.2 ns. For no multi-photon emission, the value of the $g^{(2)}(\tau = 0)$ function should be 0, meaning that there are no coincidence counts for a time delay of 0.

With the method for measuring multi-photon emission established, how does the data portrayed in figure 3.13 translate into a value for $g^{(2)}(0)$? To answer that, there must be assumptions made about the measurement apparatus, with a slight modification made to equation 2.1. The reason for this modification is that the data presented in figure 2.1.3 are coincidence counts for a time-bin of a particular duration, meaning that there is no way to resolve the number of photons detected. This means that there could be multiple photons per detection event. To model this, the equation used is

$$g^{(2)}(n) = \frac{< n_1(m) n_2(m+n) >}{< n_1(m) >< n_2(m) >} \tag{3.27}$$

where $n_i(m)$ is the number of photons measured on detector i from pulse m [86]. For this to be true, there are a number of assumptions that need to be made. Firstly, the light source is assumed to be stationary, i.e., a shift in m does not change the expectation values in the numerator or denominator [86]. Second, the histogram peak areas are approximately proportional to the numerator as long as the mean count rates are small compared with the inverses of the relevant dead times[12] [86]. For the SNSPDs, the dead time is 15 ns (67 MHz), and the count rates were about 150 kHz, meaning this approximation holds. Finally, to produce a $g^{(2)}(0)$ value from the data, the area of the nearest neighbouring peaks is compared to the area of the peaks at $\tau = 0$. This is proportional to the probability of detecting a photon from pulse $m + n$, given that a photon was previously detected from pulse m [86]. By performing this analysis using the data from figure 3.13, $g_X^{(2)}(0) = 0.0055 \pm 0.0003$ and $g_{XX}^{(2)}(0) = 0.0028 \pm 0.0003$, which is an order of magnitude greater than the QRE method, with $g_{XX}^{(2)}(0) = 0.1 \pm 0.01$ [3].

Figure 3.13 also a tapering in the height of the peaks as τ increases. This provides evidence of luminescence blinking in the QD [37]. Blinking is a phenomenon that refers to some duty cycle in which the QD is optically active. This means that the QD can only produce photons when it is "ON'. This is likely due to charges tunnelling into the QD and being trapped in the ground state. This will result in the inability to create a XX photon [87], which is referred to the QD being "OFF". To return to the ON state, the charges must tunnel out of the QD. This ON-OFF cycle, between the optically active and inactive states of the QD, is what causes the probability of detecting photons at larger time delays τ decreases. This is apparent when modelling the blinking as a telegraph ON-OFF. If we define β as the probability of the QD being ON, we can write the $g^{(2)}(\tau)$ as

$$g^{(2)}(\tau) = 1 + \frac{1-\beta}{\beta} e^{-\frac{\tau}{\tau_b}} \tag{3.28}$$

where $\frac{1}{\tau_b} = \frac{1}{\tau_g} + \frac{1}{\tau_c}$, which represent the transition rate between the ground state being occupied and filled by charges [87]. To maximize the probability of exciting the XX state, blinking must be mitigated by neutralizing or preventing the charges from occupying the QD.

[12] Is a property of the detector referring to the minimum possible time interval between two separate detection events, defined by the time it takes for the detector to register an event and prepare for another. All photons which arrive in this dead time interval are registered as a single event.

3.4.3 Quantum State Tomography

Quantum state tomography (QST) will allow us to reconstruct the density matrix of the source. To reconstruct the density matrix, methods from 3.3 are used, which involves taking correlation measurements in 36 different polarization bases corresponding to all possible pairs of combinations of the set of {H, V, D, A, R, L}. From this, we can extract the concurrence and fidelity to quantify the entanglement, which are described in section 1.3.2.

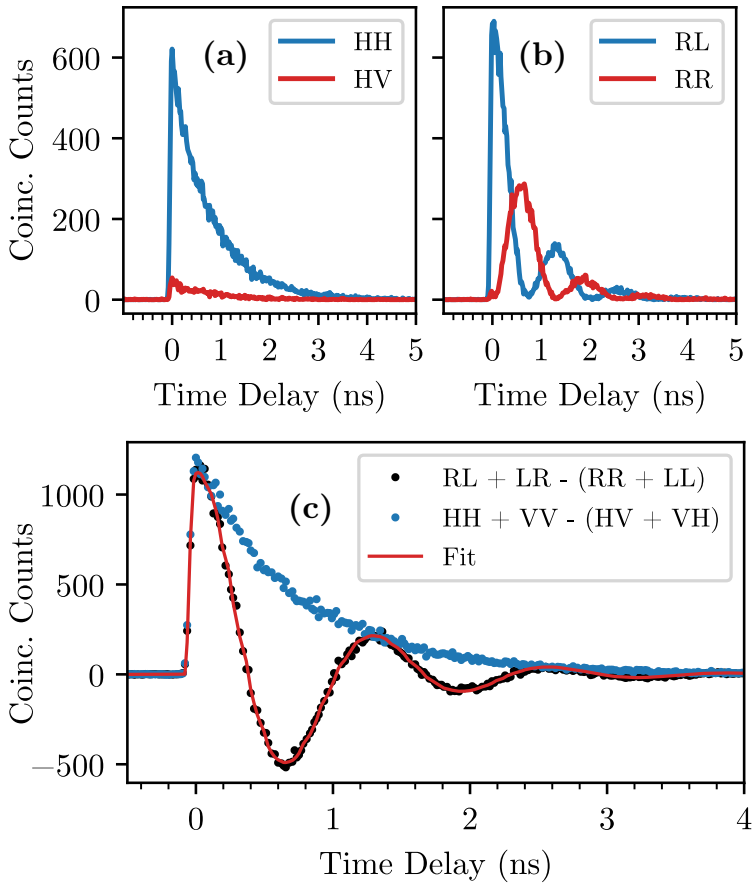

Figure 3.14: Projection measurements taken using the SNSPDs. a) In the linear basis, one can see that the bulk of the initial coincidence counts are at time $\tau = 0$. The coincidence counts also decrease exponentially in this basis. b) In the circular basis, the fine structure can be seen in the oscillations of the coincidences, contained within the exponential decaying envelope. The RL and RR states are out of phase by $\frac{\pi}{2}$. c) Overlay of the difference between the maximally entangled states, $|\Phi^+\rangle$ and $|\Psi^+\rangle$ minus the minimally entangled states, $|\Phi^-\rangle$ and $|\Psi^-\rangle$. The red curve is the best fit of the circular basis projections to some function $\cos\left(\frac{\delta\tau}{\hbar}\right)$ convolved with a Gaussian with a FWHM of 30ps to account for the small amount of blurring from the timing jitter of the SNSPDs.

By analyzing the projections, information about the QD can be extrapolated. The coincidence counts decrease exponentially as the exciton state is a stationary state of the exchange Hamiltonian when FSS is present [37, 64]. We also see minimal counts in the HV

basis, compared to the HH basis. This is expected, as the entangled state emitted from the QD oscillates between is $|\psi\rangle = \frac{1}{\sqrt{2}}(|HH\rangle + exp(\frac{i\delta\tau}{\hbar})\,|VV\rangle)$. In the circular basis, the FSS can be observed by the presence of oscillations of the coincidences, contained within the exponential decaying envelope. This oscillating behaviour is because of the oscillation between the two Bell states, $|\Phi^+\rangle$ and $|\Phi^+\rangle$, predicted by equation 2.9. The FSS frequency is determined by fitting the curve for the combined projections $|RL\rangle+|LR\rangle-(|RR\rangle+|LL\rangle)$ (both Bell states) from figure 3.15 and extracting the oscillation period, which is determined to be $T_s = 1.26$ns $(780.0 \pm 1.0$MHz).

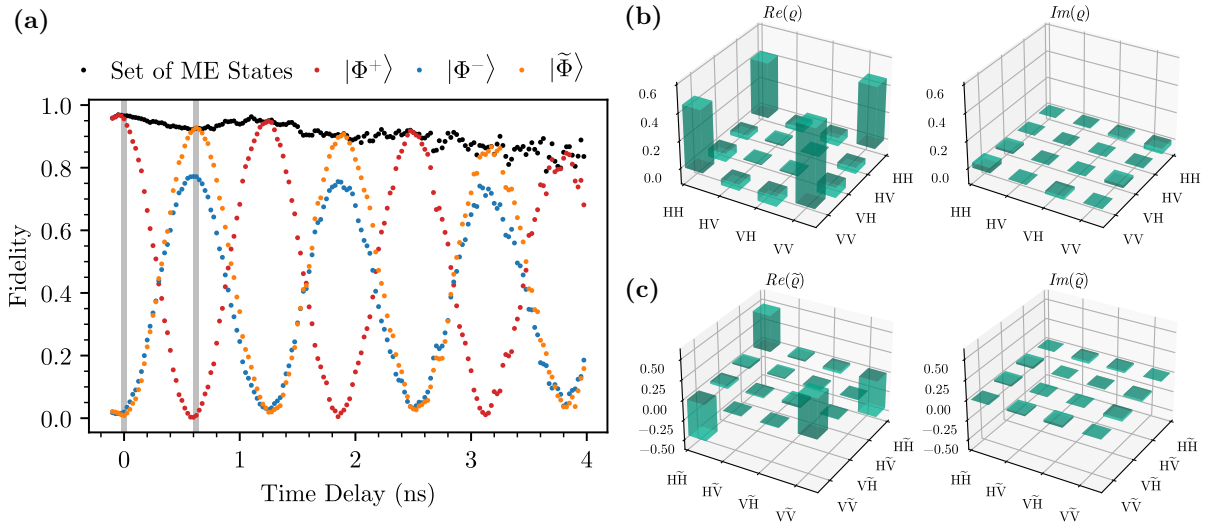

Figure 3.15: a) Maximum fidelity and fidelity to the $|\Phi^+\rangle$ (red), $|\Phi^-\rangle$ (blue), and $|\Phi^-\rangle$ after unitary rotations to both photons (yellow). Because of the FSS present, $|\psi\rangle = |\psi(t)\rangle$, where $|\psi(t)\rangle$ describes the state at any given time t, which oscillates between $|\Phi^+\rangle$ and $|\Phi^-\rangle$. b) The instantaneous density matrix reconstructed at $\tau = 0$ns, and c) instantaneous density matrix reconstructed at $\tau = 0.625$ns after applying unitary rotations to both photons to more closely represent the ideal $|\Phi^-\rangle$.

The ensemble of the projection measurements taken can be compiled and analyzed to construct the density matrix of the source. The density matrix contains all the information that describes the source. Since we have coincidence counts over the entire emission lifetime of the QD, we have a semi-continuous density matrix, $\rho = \rho(\tau)$, where τ is in 30 ps time slices. This becomes evident when looking at figure 3.15, where two different density matrices have been constructed at different times, $\tau = 0$ ns and $\tau = 0.625$ ns, were selected

because they represent time slices where the photons correspond to both the $|\Phi^+\rangle$ and $|\Phi^-\rangle$ respectively.

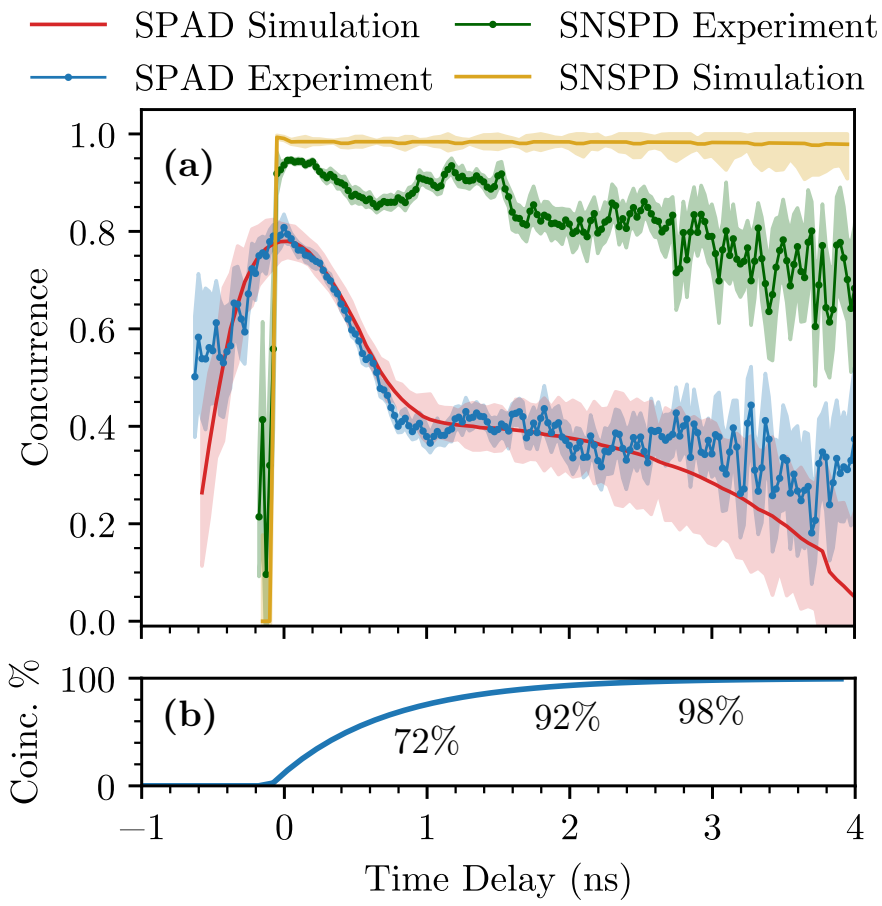

Figure 3.16: a) Compilation of both the simulation and measured data for both SPAD and SNSPD measurement systems, for the same NWQD source. One can immediately see the improvements in concurrence due to the ability to resolve the oscillating state in time. b) A measure of the percentage of coincidence counts, which is required for a TPRE experiment, over the lifetime of the emission. Over 90% of the concurrences are measured before 2 ns, which is why the concurrence curves become noisier as time progresses after this. This is because the number of dark counts become comparable to the number of single photons arriving at the detector, thus this random process becomes more dominant.

Finally, it is important to stress the difference between the results using the SPADs and

SNSPDs. Figure 3.16 overlays both the theory and data for the SPADs and SNSPDs. For the SPADs, the shape of the curve is much different than the SNSPDs. This is because of the large timing jitter of the SPADs, resulting in detections before $\tau < 0$. As τ increases, there is a slow rise in concurrence as more coincidences are measured. The increase in concurrence reaches a peak of $\mathcal{C}$ =80±3%. The concurrence then steadily declines until it reaches a "flat" region where the detection response function has sampled the temporal evolution of the entangled state [37]. The slow rise, low peak concurrence[13], and fall of the concurrence is due to phase averaging. Conversely, there are no slow rise/fall regions in the concurrence curve for the SNSPDs, which appear to peak instantaneously at $\tau = 0$ and remain flat. We measured a peak concurrence (fidelity) of $\mathcal{C}$ =95.6±0.7% ($\mathcal{F}$ =97.7±0.4%). The lifetime-weighted values of concurrence (fidelity) for the SNSPDs are $\tilde{\mathcal{C}}$ =90.2±0.2% ($\tilde{\mathcal{F}}$ =94.0±0.1%), which is far larger than the lifetime-weighted concurrence measurement of $\tilde{\mathcal{C}}$ =50.8±0.2% collected using the SPADs. Thus, simply by changing the measurement apparatus and excitation technique provides a better picture of the true quality of the source, which has wider implications for the QD community.

However, with the SNSPD, there seems to be a larger discrepancy between the simulation and data as opposed to the SPADs. The smaller measured peak concurrence could be because of laser light used in the excitation scheme leaking into the emission lines of the XX or X photons, causing correlations not associated with the QD emission. The lower "flat" region also contains some oscillations, which occur at around the FSS period, were not predicted in the model. The reason for this is unknown, but the likely cause is an error in the projection measurements. This could occur due to small deviations in the waveplate angles, which, when compounded with the increased resolution of the detection system, are not averaged out into a flat region. This means that to obtain a perfectly flat curve like in the model, near perfect projection precision is needed. We also note that the roll-off region can be explained by spin-scattering of the X spin before recombination [37], which was observed with the SNSPDs. It's also worth noting that in the area where the roll-off region occurs, that only 8% of the X photons are emitted after this point, meaning higher uncertainty values are present.

With the improvement in entanglement fidelity from previous works, it has become clear that NWQDs are a promising candidate for the title of "on-demand entangled photon source." This work has shown that these sources can provide "near unity" entangled pairs, as shown on figure 3.17. However, there is still work to be done to improve the pair extraction efficiency. One way to do this is to eliminate blinking. Blinking infers that, due to the background n-doping of the nanowire, the s-shell of the QD is occupied for some time, making the population of the XX levels impossible. There are two methods

[13]With respect to the SNSPDs.

to mitigate this issue: 1) place gates around the nanowire to pull charges away from the QD [42], and 2) two-colour excitation. Two-colour excitation refers to using lasers of two different wavelengths to excite different transitions. For example, with one laser tuned to the XX level and another tuned to some energy transition from the XX to an available level in the conduction band, the XX level can be emptied before direct population [88].

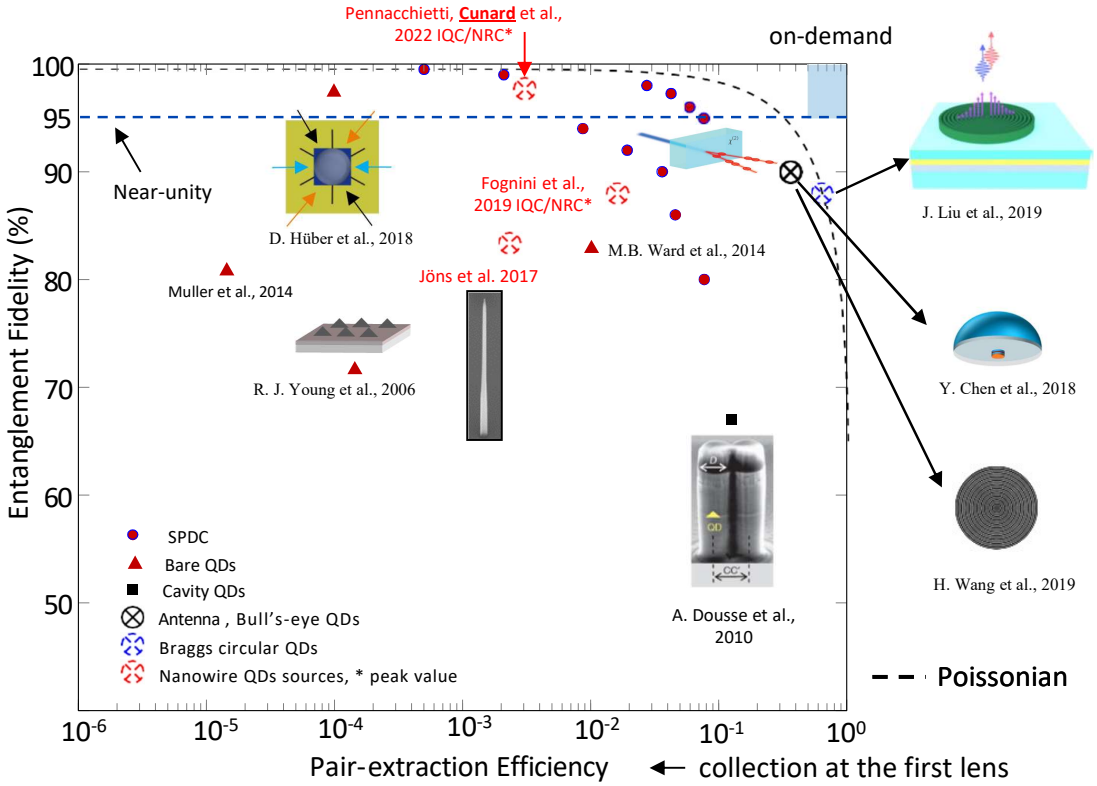

Figure 3.17: Road map towards an on-demand entangled photon source, with the results from this thesis juxtaposed with results from previous works.

Chapter 4

Photonic Integrated Circuits

Photonic integrated circuits (PICs) are a promising technology that aims to encapsulate the complex and bulky world of free space optics and condense it into a smaller footprint. PICs are analogous to their analogue counterparts, the MOSFET chip used in today's computers, but instead of using electrons to control information flow, processing, and storage, they use light. Because of the different information carriers, methods of manipulating that information has to change. However, despite this difference, there are components that both mimic the information manipulation and go beyond; harnessing the wave-like behaviour of light to create superposition and interference.

One of the main advantages of PIC technology today is the CMOS manufacturing process. This allows for the use of foundries to mass produce chips in a relatively short period of time. The current state-of-the-art foundries, Advanced Micro Foundry (AMF), and Applied Nanotools Inc (ANT), are capable of fast turnarounds, producing and shipping hundreds of chips within months.

The current state of PIC technology is underdeveloped because of the material commonly used to manufacture them: silicon. Silicon is easy to work with because of its compatibility with CMOS technology. Silicon also supports light at C and O band telecom wavelengths. However, silicon does not support wavelengths which many QDs emit. The NWQD studied in this thesis emits at around 894 nm, and silicon's transparency window is 1.1 μm to 3.7 μm, meaning it will absorb all light outside this range. This chapter will explore a material which does support light at the desired wavelength, and the associated components needed to perform rudimentary QIP operations.

4.1 Confinement in Dielectric Media

Confinement refers to the ability of some dielectric media to constrain light in certain directions. A great example of this is fibre optic cables. Fibre optic cables operate on the principal of total internal reflection. The condition for total internal reflection depends on the refractive indices of the respective materials. For an in-depth visual explanation, please see figure 4.1.

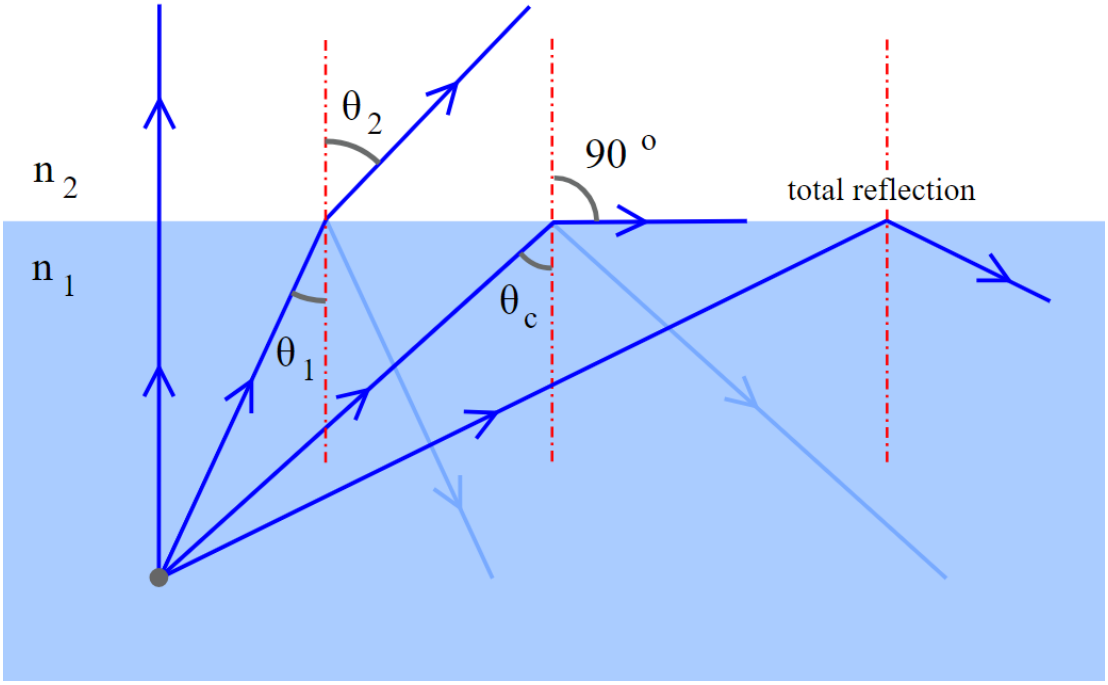

Figure 4.1: Visual representation of total internal reflection at the surface of two transparent media with two different indices of refraction, n_1 and n_2 where $n_1 > n_2$. Light travels through medium 1 at some angle θ_1 and strikes the interface of the two media. If the angle of incidence is less than the critical angle, θ_c, light will propagate into medium 2 at some angle θ_2 where $\theta_2 > \theta_1$. As θ_1 increases towards θ_c, θ_2 will increase until $\theta_2 = \theta_c$. It is at this point, where $\theta_1 \geq \theta_c$, that light in medium 1 will be reflected at the interface of the two media and will never propagate into media 2, meeting the criteria for total internal reflection. Figure by Gavin R Putland, licensed under CC BY 4.0.

Confinement is a property which, when utilized, can be used to route light in dielectric

semiconductor waveguides[1]. For this to work, the light being confined has to have a greater wavelength than the bandgap of the material. This ensures that the light is not absorbed and can propagate through the material. This concept of light seeing a material as transparent is known as the "transparency window", and is an important property in designing PICs around a source which emits single photons of a specific wavelength.

4.1.1 Electromagnetic Waves in Dielectric Media

The aforementioned transparency window requires that light is not absorbed by the material. Therefore, we need to design the waveguide material to have a bandgap that is larger than the wavelength of the light. Having a bandgap larger than the energy of the photons will result in the light not being absorbed by the material, as it does not possess enough energy to cause a transition [89]. However, for an increase in band gap energy there is a decrease in refractive index [89], which will increase the footprint of the components [90]. The reason for this can be seen in figure 4.1 in conjunction with Snell's law

$$\frac{n_1}{n_2} = \frac{\sin(\theta_2)}{\sin(\theta_1)} \tag{4.1}$$

where the conditions for total internal refraction are that $\theta_1 = \theta_c$ and $\theta_2 = \frac{\pi}{2}$. As the index of refraction decreases for material 1 (the material in which light propagates), this must be compensated by an increase in θ_c. Thus, any components we design for a material with a lower index of refraction must account for this increase in the critical angle. This can manifest itself in an increased bend radii for waveguides. Higher index of refraction also means higher loss due to nanometer-scale roughness on the interfaces of the dielectric media [90]. Because we are dealing with single photons i.e. the amount of light we have is small compared to the conventional laser, we need to optimize the loss as best as we can. It is for all the aforementioned reasons we decided to use silicon nitride as the dielectric media, which has an index of $n_{SiN} = 2$ and bandgap energy of $E_g = 3.10$ eV, making it transparent to wavelengths of from 400 nm to 2 μm [91]. This is in contrast to what is typically used for PIC design, silicon which has an index of refraction of $n_{Si} = 3.5$ with a bandgap energy of $E_g = 1.12$ eV, making it transparent to wavelengths of from 1.1 μm to 3.7 μm [91].

[1]See section 4.2.1 for an in-depth discussion on what waveguides are and how they work.

4.2 Passive Components

Passive components are designed with the intent that the material and geometry itself will provide the desired properties. For example, a waveguide will confine and guide light without external interaction from other components such as heaters or electrodes; the purpose of the waveguide is enacted by the waveguide itself. Another example of a passive component is the beam splitter. The beamsplitter can be manufactured to transmit and reflect light by any ratio of the incoming beam. For example, a 50:50 beamsplitter will transmit 50% of the light and reflect the other 50%. The work of splitting the light is done solely by the light-matter interaction of the material. In the following sections, I will explain the principles of common passive components used in PIC design and the typical roles in which they are used.

4.2.1 The Waveguide

Waveguides have been previously mentioned for their ability to confine and guide light on a PIC. Because of this, waveguides are the basic building block for any PIC. Since we are working with photons, aspects like polarization, wavelength, and spacial mode become important considerations when designing these waveguides. To understand how these criteria can be considered when designing the waveguides, it's important to make decisions on what kind of light will be supported in the waveguides. To answer this question, a systematic checklist, like the one found in ref [92], must be followed.

1. Waveguide geometry: this involves how the waveguide will be shaped. Shapes include planar, slab, and strip waveguides.
2. Guiding mechanism: how will light be confined and guided in the waveguide. This can be done by total internal reflection or photonic bandgap method[2].
3. Mode structure: what spacial modes do we want supported in the waveguide for a particular wavelength of light? Single-mode or multi-mode?
4. Refractive index distribution: step or gradient index?

[2]Refers to the engineering of allowable spacial modes in which light can exist. Everywhere light of a particular spacial mode is allowed, light will travel. Light is bound between areas where the bandgap does not allow for light of a particular wavelength to exist, meaning the only path where light can travel is in the allowable bandgap.

5. Waveguide material: glass, polymer, semiconductor, metal, others.

By answering these questions, we can narrow the search to a waveguide which will best fit the needs.

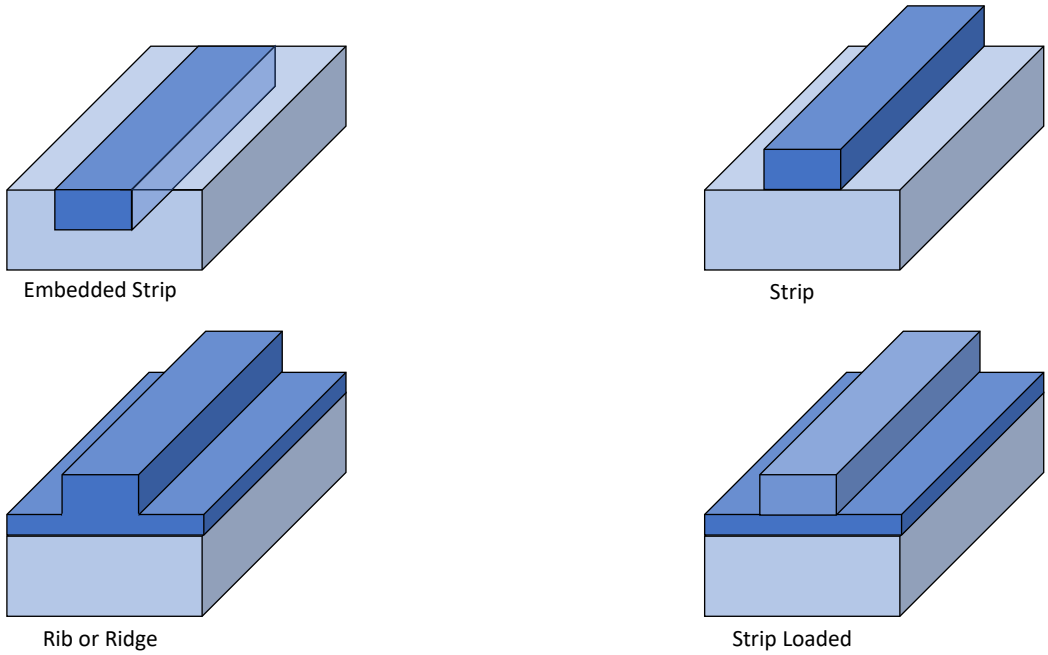

Figure 4.2: The various types of waveguides offered in PIC design platforms. The darker shade of blue indicate the dielectric material which will confine the light.

Waveguides are the building blocks for many components in PIC design. Components such as ring resonators, Mach-Zehnder interferometers, directional couplers, and Y-branches use waveguides arranged in different orientations to achieve different effects. Before we delve into other components, we will establish how waveguides work to gain an understanding of other components moving forward.

Fundamentals of Waveguides

As with all electromagnetic analysis, we begin with Maxwell's equations similar to the ones introduced in chapter 1, but in a different form:

$$\nabla \times \vec{E} = -\frac{\partial \vec{B}}{\partial t} \tag{4.2}$$

$$\nabla \times \vec{H} = \vec{J} - \frac{\partial \vec{D}}{\partial t} \tag{4.3}$$

$$\nabla \cdot \vec{B} = 0 \tag{4.4}$$

$$\nabla \cdot \vec{D} = \rho \tag{4.5}$$

where $\vec{E}$ (V/m) is the electric field vector, $\vec{H}$ (A/M) is the magnetic field vector, $\vec{B}$ (Wb/m^2) is the magnetic induction vector, $\vec{D}$ (C/m^2) is the electric displacement vector, $\vec{J}$ (A/m^2) is the current density vector, and ρ (C/m^3) is the volume charge density. Intuitive explanations of each of these equations can be found in chapter 1. Here, we can establish further relations,

$$\vec{D} = \varepsilon \vec{E} \tag{4.6}$$

$$\vec{B} = \mu \vec{H} \tag{4.7}$$

where $\varepsilon = \varepsilon_0 \varepsilon_r$ and $\mu = \mu_0 \mu_r$. Here, ε_0 and μ_0 are the permittivity and permeability of free space and ε_r and μ_r are the relative permittivity and permeability of a material, which is some factor in which to multiply their respective free space variables[3].

Firstly, we need to establish boundary conditions at the edge of the waveguides. To do this, we need to first establish allowable modes which we want supported in the waveguides. In formal language, these modes, and by extension boundary conditions, are as follows:

1. TEM waves: waves with no electric or magnetic field in the direction of propagation ($H_z = E_z = 0$). For example, plane waves.
2. TM waves: waves with no magnetic field in the direction of propagation ($H_z = 0, E_z \neq 0$).
3. TE waves: waves with no electric field in the direction of propagation ($H_z \neq 0, E_z = 0$).

[3]Interestingly, one can see from Maxwell's equations that refractive index, n, is defined as $n = \sqrt{\mu_r \varepsilon_r}$ and is inversely proportional to the speed of light in some material.

4. Hybrid waves: boundary conditions require all field components, ($H_z \neq 0, E_z \neq 0$). These waveguides can couple both TE and TM waves.

Note that these boundary conditions assume that light is propagation, electric field, and magnetic field are in the z, y, and x directions respectively. For the convention, the y direction is in-plane with the substrate and will be associated with TE modes or TM modes, depending on if the electric or magnetic field will be oscillating in that direction respectively. For example, if the electric field is oscillating in the y direction, these will be the TE modes [92]. With these conventions in mind, it is time to delve into a mathematical description of how electromagnetic waves behave while propagating through waveguides.

Since TE and TM modes are symmetrical in how they behave, we will derive the behaviour of light in waveguides based on TE modes. First, we assume that there is no loss and the waveguides is a dielectric medium. This is as an ideal case as to describe how the electric field behaves and then introduce where loss can occur later. Because this is a lossless dielectric medium, the light-matter interaction depends on ε and μ_0. Next, we assume no variation in the y direction and the electric field is periodic in time and dependent on angular frequency. With this in mind, the wave equation becomes:

$$\nabla^2 \vec{E} = \mu_0 \varepsilon \frac{\partial^2 \vec{E}}{\partial t^2} \tag{4.8}$$

If we expand the above equation into its Cartesian components, we can simplify the equation by applying the boundary conditions, i.e. the electric field oscillates in the y direction only.

$$\frac{\partial^2 \vec{E_y}}{\partial x^2} + \frac{\partial^2 \vec{E_y}}{\partial y^2} + \frac{\partial^2 \vec{E_y}}{\partial z^2} = \mu_0 \varepsilon_0 \varepsilon_r \frac{\partial^2 \vec{E_y}}{\partial t^2} \tag{4.9}$$

In the TE mode, the $\vec{E}$ vector is polarized along the y axis, with no longitudinal component in the z axis. Another way of viewing this with respect to the waveguide is that the electric field is transverse to the plane of incidence established by the normal to the surface, and by the wavevector, k [92]. If we assume that the light inside the waveguide is of some source frequency ω_0 with some vacuum wavevector magnitude, k_0, then we can say that $|k_0| = \frac{\omega_0}{c}$ where c is the speed of light, and k_0 is related to the wavelength, λ, of the light source by the relation $k_0 = \frac{2\pi}{\lambda}$. We can also introduce a propagation constant in the z direction, β, because there is no transnational variance of the structure of the waveguide. With all of these assumptions and variables in place, equation 4.9 becomes

$$\frac{\partial^2 \vec{E}_y}{\partial x^2} + (k_0^2 n_i^2 - \beta^2)\vec{E}_y = 0 \tag{4.10}$$

where $n_i = n_f, n_s$ or n_c[4] depending on the location.

Now, we have a way of describing the TE modes supported in the waveguide in terms of fundamental constants. The value of the constants will determine if the propagating light will simply refract ($\beta < k_0 n_c$), refracting at one interface but not confined ($k_0 n_c < \beta < k_0 n_s$), and totally confined ($k_0 n_s < \beta < k_0 n_f$) [92].

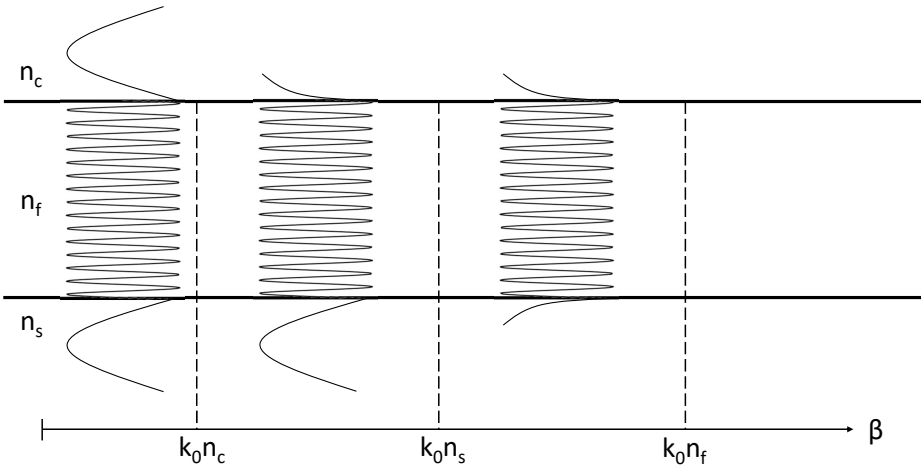

Figure 4.3: EM field confined inside of waveguides, for different propagation constants.

The field exponentially decaying outside the waveguide in the wave picture is known as the evanescent field. This is the fraction of the field located outside the waveguide, but is still part of the propagating wave. This will become an important property as we introduce more components to the PIC toolbox.

Next, it is important to describe other modes of light which can exist in the waveguide described above. So far, we have assumed no particular mode to be supported in the waveguide, only light described by the fundamental constants introduced in equation 4.10. By analyzing the conditions laid the in figure 4.3, we can establish conditions which lead to the lowest order and highest order modes allowed based on the incident angle in which

[4]Indices of the cladding, guiding, and substrate layers are n_f, n_s and n_c respectively. Light can only be guided if $n_f > n_s > n_c$ [92].

the light strikes the interfaces of the waveguide. From figure 4.1, we know that there is a limit to how large the angle of incidence can be before total internal reflection no longer occurs, i.e. $\theta \leq \theta_c$. Similarly, since higher order modes penetrate deeper into the cladding than lower order modes, there must be a relation between the angle of incidence and the highest order modes supported in the waveguides. Formally, the higher order mode has a larger angle which is nearly the critical angle and the lowest order mode is nearly parallel to the propagation axis,

$$\beta_{LowestOrder} < k_0 n_f \tag{4.11}$$

$$\beta_{HighestOrder} \approx k_0 n_f cos(\theta) \approx k_0 n_s \tag{4.12}$$

where θ is the angle of incidence. The cutoff thickness, t_{co} of the TE_m mode, i.e. the thickness of the waveguide needed to support m modes of TE light, is

$$t_{co} = \frac{\lambda}{2\pi\sqrt{(n_f^2 - n_s^2)}}\left[m\pi + arctan\left(\frac{n_s^2 - n_c^2}{n_f^2 - n_s^2}\right)\right] \tag{4.13}$$

where $m = 0$ (fundamental mode), $1, 2, 3....$ By calculating the cutoff thickness for the required mode, the thickness of the waveguide can be determined. This is important when designing single mode waveguides [92].

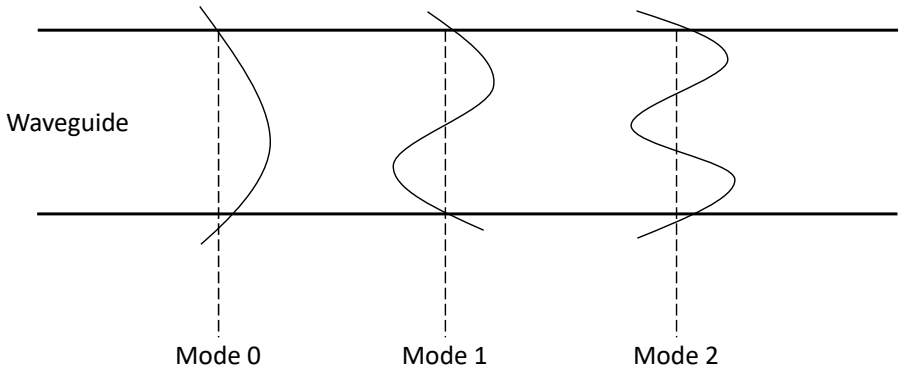

Figure 4.4: Various types of EM modes supported in a waveguide for various values of m. In this instance, "Mode 0" corresponds to $m = 0$, "Mode 1" corresponds to $m = 1$, and so on.

4.2.2 Waveguide Simulation and Results

Although the equations and models are a great guideline to get an approximate geometry for the waveguide, it is not the only tool. Other tools exist which can simulate scenarios more accurately. One such tool which was used in my research was Lumerical. Lumerical is a simulation software which allows for the modelling and simulation of optical, electrical, thermal and quantum effects at the physical level [4]. Lumerical is an extremely powerful and useful tool that allows for the sweeping of parameters for optimization. The software allows for the initialization of the typical scenario to ensure maximum accuracy for real world experiments. For more information on the specifics of Lumerical simulations as they relate to your specific experiment, please visit ref [4].

The simulation for the waveguide was done using Lumerical MODE Solutions, which solves for the eigenmodes in a cross-section of an arbitrary waveguide geometry (or a 3D geometry) at a particular frequency by solving for time-harmonic solutions to Maxwell's equations [93, 4]. The wavelength of the light is fixed at $\lambda = 894$ nm because it is the wavelength of light that is emitted from the NWQD source. the goal is to sweep the dimensions of the waveguide (within the limits of AMF) to determine which geometry is suitable to support single mode light at the wavelength. We desire single mode coupling because the light emitted from the NWQD source is a Gaussian profile, meaning it will have its highest coupling efficiency to single mode confinement structures. After setting up the strip waveguide shown in figure 4.2, we determined the best geometry for the waveguide is 450 nm x 400 nm for coupling TE modes while staying within the design restrictions of AMF.

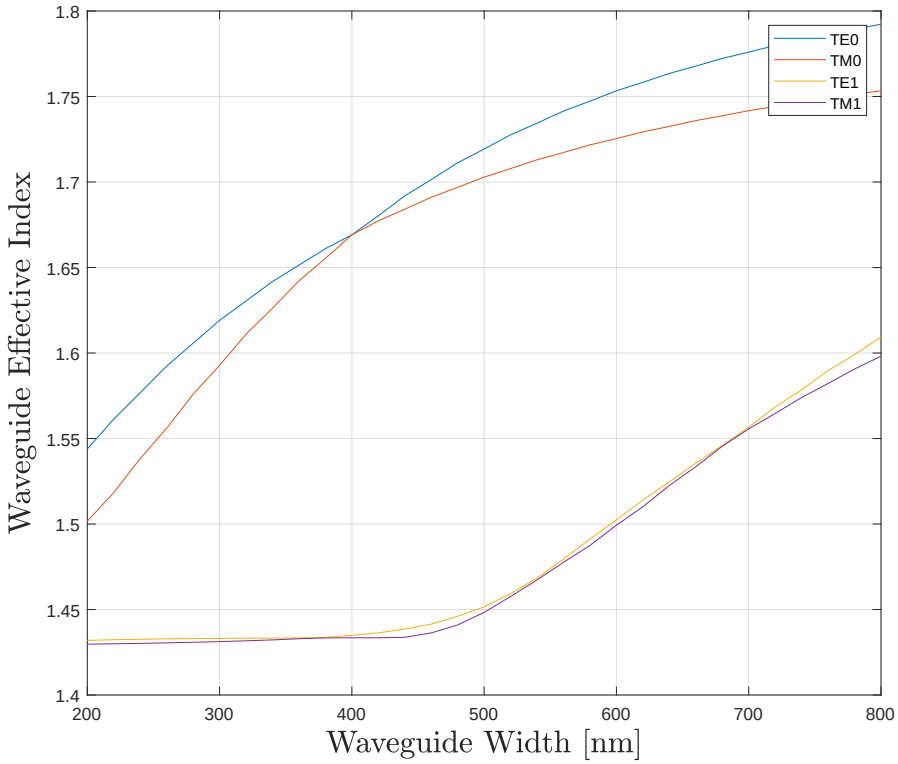

Figure 4.5: Waveguide width vs effective index, as a function of the supported waveguide polarization modes.

The next step was to determine the bend radius of the waveguides to minimize loss as the light changes direction. With Si having a higher refractive index than SiN_x, bend radii can be smaller due to the higher confinement. Many simulations and studies have been done on Si waveguides to determine the optimum bend radius, however, since Si is not transparent at the wavelengths, we need to use a lower refractive index material, SiN_x. With the optimal waveguide dimensions determined from the previous simulation, the next step was to determine how large the bend radius could be to minimize loss from factors such as scattering losses and substrate leakage, radiative loss, and mode mismatch losses due to differences between the modes of the straight vs bend waveguides. The simulation is shown in figure 4.5 and simulated using the 3D Finite-Difference Time-Domain (FDTD) method. This method solves Maxwell's equations directly without approximations, making it an extremely powerful tool. Using this, we determined that the bend radius should be at least 50 μm.

4.2.3 Directional Coupler

Directional couplers are among the most common methods for splitting and combining light on a PIC. The directional coupler consists of two parallel waveguides in proximity, where the evanescent fields of the desired modes overlap. The strength of the coupling, or the "coupling coefficient," is determined by both the spacing between the waveguides and the length at which they maintain this gap. The concept of waveguide-to-waveguide coupling will be a fundamental concept and building block to explain the behaviours of all passive components moving forward. Because of this, it is imperative to fully explain the physics behind how they work and how we can tailor their design to get the desired responses.

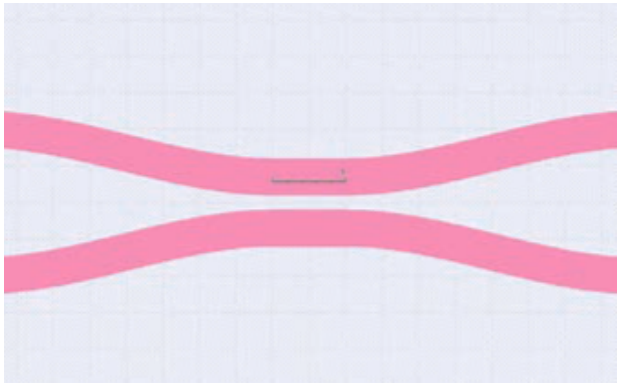

Figure 4.6: KLayout representation of a directional coupler.

To begin, we will establish the method, coupled mode theory [94], which states that power is exchanged between modes in the presence of perturbation[5]. The coupled mode theory states that the power coupled from one waveguide to the other can be shown as

$$\kappa^2 = \frac{P_{cross}}{P_0} = \sin^2(CL) \tag{4.14}$$

where κ^2 is the ratio of coupled light that crossed over into the empty waveguide, P_0 is the input power, P_{cross} is the power of the coupled light that crossed over into the empty waveguide, C is the coupling coefficient, and L is the length of the coupling region. Because power and energy are related, we can apply the conservation of energy, and by extension

[5]The perturbation in question is the presence of coupling between the two waveguides due to the evanescent fields.

the conservation of power, to determine the amount of power which was not coupled to the empty waveguide. This relation states that $\kappa^2 + t^2 = 1$ where t^2 is the aforementioned remaining power not coupled to the other waveguide in the directional coupler. By using the relation $\sin^2(\theta) + \cos^2(\theta) = 1$, we know the form of t^2 must be

$$t^2 = \frac{P_{through}}{P_0} = \cos^2(CL) \tag{4.15}$$

where $P_{through}$ is the power not coupled to the other waveguide. This relation holds for any lossless couplers.

Now that we have derived models relating the output power of both ports of the directional coupler, the next steps are to determine both the coupling coefficient, C and the coupling length, L in terms of physical variables related to the system. These physical variables are the wavelength of the light, λ, and the refractive indices of the material, n_1 and n_2 where $n_1 > n_2$.

The first step is to determine the analytical method. From reference [93], the method used is the "supermode" analysis method, which is based on numerical calculations based on the refractive indices n_1 and n_2. Next, the "eigenmode expansion method" (EME) is used to determine C. By using these methods, C can be found to be

$$C = \frac{\pi \Delta n}{\lambda} \tag{4.16}$$

where $\Delta n = n_1 - n_2$ [93].

Now that we have an expression for the coupling coefficient, next we need to determine the coupling region length. We can do this by examining the relation between the propagation constants for the two modes in the directional coupler after some light has been coupled.

$$\beta_1 = \frac{2\pi n_1}{\lambda} \tag{4.17}$$

$$\beta_2 = \frac{2\pi n_2}{\lambda} \tag{4.18}$$

Interestingly, as the modes travel through the waveguides, they oscillate between the waveguides, as shown in figure 4.7.

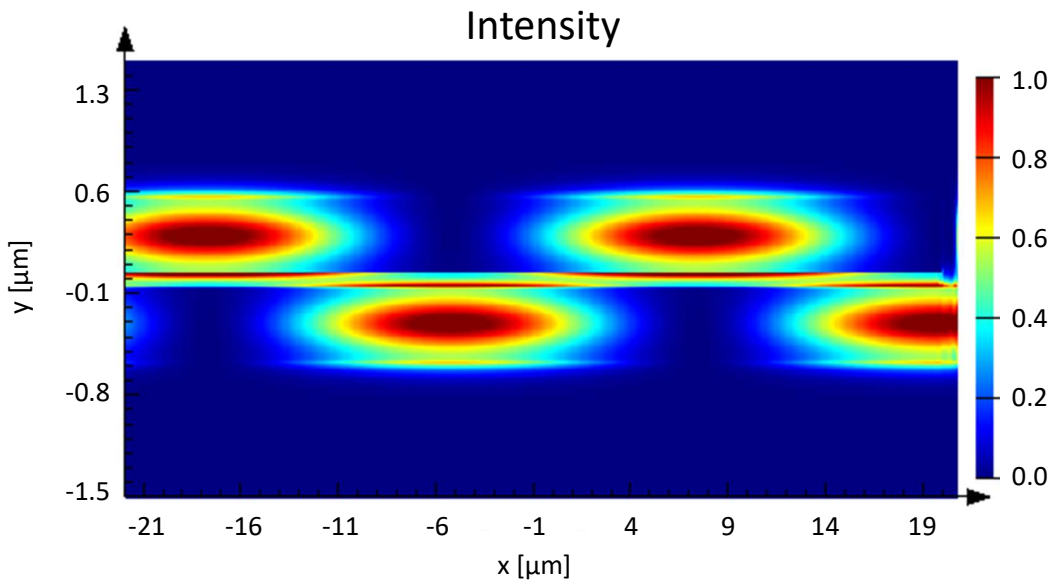

Figure 4.7: Lumerical simulation of light travelling through two parallel waveguides. The light oscillates π out of phase in each waveguide, indicated by the varying intensities. Image taken from [4] and licensed under CC BY 4.0.

From this, we can infer that the phase difference between the light in the two waveguides is π. With this knowledge, we can find the crossover length, L_x, which defines when there is a π phase shift between the modes and the power becomes localized in the second waveguide. In other words, this is the length needed for the power to be completely transferred to the other waveguide. With this, we can find L_x:

$$\begin{aligned} \beta_1 L_x - \beta_2 L_x &= \pi \\ [\beta_1 - \beta_2] L_x &= \pi \\ \left[\frac{2\pi n_1}{\lambda} - \frac{2\pi n_2}{\lambda}\right] L_x &= \pi \\ L_x &= \frac{\lambda}{2\Delta n} \end{aligned} \tag{4.19}$$

Despite clear models to describe the coupling of light between two waveguides, there is a clear aspect missing from this: how far/close the waveguides need to be, and how does

this affect what we have already found? Unfortunately, the answer is far less simple than previous methods, in the sense that there are no direct equations we can draw from to make the model. The method that was used in ref [93] was a numerical fit based on simulated data. They fit data taken from various simulations to some exponential function:

$$C = Be^{-Ag} \tag{4.20}$$

where C is the coupling coefficient, g is the gap distance, and A and B are "catch-all" terms to encapsulate the geometry, optical wavelength, and other physical properties of the coupler. By performing Lumerical simulations and performing a fit to the exponential function listed earlier, a relation between the gap distance and crossover length was determined to be

$$L_x = 10^{(0.0026084+g[nm]+0.657094)}[\mu m]. \tag{4.21}$$

From the fit equation, the field coupling coefficient for any gap or length can be determined to be

$$\kappa = \left(\frac{P_{coupled}}{P_0}\right)^{\frac{1}{2}} = \left|\sin\left(\frac{\pi\Delta n}{\lambda}L\right)\right|$$
$$\kappa = \left|\sin\left(\frac{\pi\Delta n}{\lambda}\frac{z}{L_x}\right)\right| \tag{4.22}$$

where z is the gap distance between the two waveguides.

Finally, the light at the output of the directional coupler, E_{wgA} and E_{wgB}, assuming we want 50% of the light in each port, can be described by the following equations:

$$E_{wgA} = \frac{1}{\sqrt{2}}\left(e^{(i\beta_1 L)} + e^{(i\beta_2 L)}\right) \tag{4.23}$$

$$E_{wgB} = \frac{1}{\sqrt{2}}\left(e^{(i\beta_1 L)} + e^{(i\beta_2 L - i\pi)}\right) \tag{4.24}$$

where the phase of the light in each waveguide can be found through

$$phase(E_{wgA}) = \frac{\beta_1 + \beta_2}{2} L \tag{4.25}$$

$$phase(E_{wgB}) = \frac{\beta_1 + \beta_2}{2} L - \frac{\pi}{2}. \tag{4.26}$$

Notice how there is a $\frac{\pi}{2}$ phase difference between the light in wgA and wgB. This is an important property when cascading directional couplers in more complicated structures, like Mach-Zehnder interferometers.

4.2.4 Directional Coupler Simulation and Results

Similar to the waveguides, the simulations for the directional couplers were done in Lumerical's eigenmode solver. This allows us to determine how the modes propagate through a directional coupler as we vary some key aspects of the coupler, such as gap between the waveguides and coupler length. To maximize the coupling coefficient, i.e. the strength of the coupling, we decided to place the waveguides as close as AMF would allow. This will allow us to fix one of the parameters, reducing the time it will take to completely simulate the directional coupler. The gap was held at a distance of 400 nm.

Next we varied the coupling length. We started by placing two SiN_x waveguides parallel to each other at the minimum gap distance specified by AMF. Then we placed a source in one of the waveguides which will emit into the fundamental mode of the waveguide which we designed for in section 4.2.1. Power monitors were placed at the output of each waveguide to provide a detailed view of the mode profile and intensity of the light passing through the structures. Finally, a sweep of the coupling length was performed. The coupling length was determined by monitoring the output power monitors until each monitor registered half of the initial intensity. Figure 4.8 shows the amount of light coupled to each waveguide in the directional coupler, and for a 50:50 splitting ratio the coupling length was determined to be 18μm. This means that we have effectively created a 50:50 beamsplitter, an important building block for PIC design.

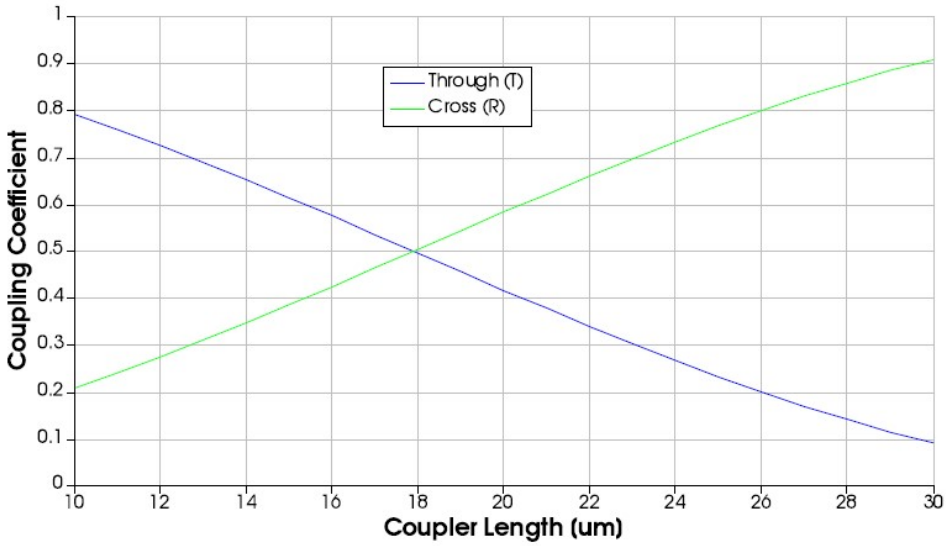

Figure 4.8: Splitting ratio as a function of coupler length.

4.2.5 Mach–Zehnder Interferometer

Mach–Zehnder interferometers (MZIs), at their most basic function, are used to determine the relative phase differences between two beams of light. They have a variety of applications across many disciplines in physics and engineering. Some applications include quantifying quantum entanglement [95], visualizing air flow in wind tunnels [96], heat transfer [97], and many others. Their role in experimental physics and engineering is ever-growing and has no indication of slowing down. In this section, we will discuss the basic topology of a free space and PIC MZI and explore how they work.

The simplest free space MZIs consist of a light source, collimator lens, two beamsplitters, two mirrors, and two detectors. The light travels from the source, through the collimator, where it is then split into two paths by the beamsplitter. One path is denoted as the reference path, the other contains some "sample" which the light will interact with, effectively changing its path length[6] and phase. The light is then reflected onto another beamsplitter where the two beams will interfere, which will then be seen at the detectors. The interference pattern seen at the detectors will give you information about the material.

[6]Remember, $v = \frac{c}{n}$ where c is the speed of light and n is the refractive index.

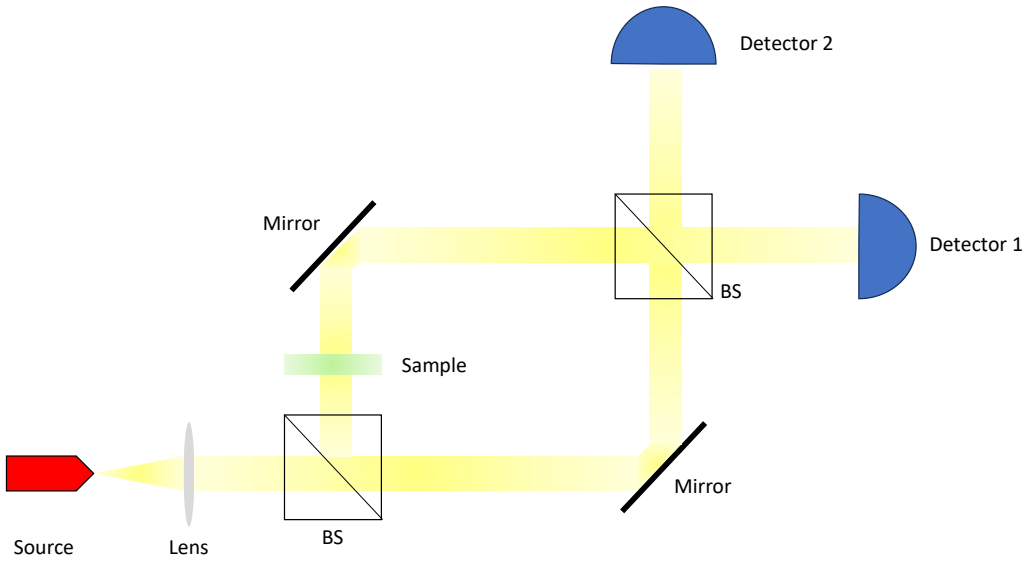

Figure 4.9: Schematic of a MZI. Light is emitted from the source and collimated by the lens. The collimated light travels through both ports of the beamsplitter, where one arm travels through a sample with refractive index n_{sample}, which effectively changes the path length. Both beams interfere at the second beamsplitter, and travel to both detectors where the interference pattern can be analyzed.

Now that we understand how the free space MZI works, now we need to explore how we can translate the free space components to the PIC. With the waveguides supporting certain confined modes and guiding the light through the PIC, we do not need to design for them. Another way of viewing this is that the waveguides, which we have already designed, will carry the functionality of the mirrors and collimating lens. The detectors will not be needed on the chip, as we will explore ways of getting light in and out of the chip in section 4.4. The remaining two components we need to emulate are the sample path, which allow us to change relative the path length and phase of the light, and the beamsplitters.

To begin, we will explore the easiest option: the sample path. The sample path simply requires the paths to be of different lengths, since the phase of the light depends directly on the path length, as seen in equations 4.25 and 4.26. However, if we choose to vary the length of the second path of the paths by some length ΔL, The resulting path length of the second path $L_2 = L_1 + \Delta L$. Thus, by changing the length of the second path, we can cause a phase shift of the light relative to the light in the first path. Thus, we have created a "phase shifter," which has the unitary matrix

$$P(\phi) = \begin{pmatrix} 1 & 0 \\ 0 & e^{i\Delta\phi} \end{pmatrix} \tag{4.27}$$

where $\Delta\phi$ is the relative phase difference induced by the asymmetrical path.

Next, we will explore how we can recreate the beamsplitter by using the components we've already discussed. To begin, we first need to determine which component we need that allows us to split the light, and then prove that its behaviour mimics that of a free space beamsplitter. One of the components we have already discussed is the directional coupler. The directional coupler has either one or two input ports, a coupling region where interference can occur, and two output ports. This makes it a prime candidate for the beamsplitter.

Following the coupled mode theory for a lossless directional coupler as laid out in reference [98], the coupled mode equation described by the supported modes in each waveguide is:

$$a_1(L)e^{i\frac{\beta_1+\beta_2}{2}L} = u(L)a_1(0) + v(L)a_2(0) \tag{4.28}$$

$$a_2(L)e^{i\frac{\beta_1+\beta_2}{2}L} = v(L)a_1(0) + u^*(L)a_2(0) \tag{4.29}$$

where $a_1(L)$ and $a_2(L)$ are the annihilation operators for each of the waveguides in the coupling region of length L, and $u(L)$ and $v(L)$ are some coefficients to encapsulate all interactions between the mode overlap between the two waveguides. With these equations, the transfer matrix for the beamsplitter is

$$T(L) = \begin{pmatrix} u(L) & v(L) \\ v(L) & u^*(L) \end{pmatrix} \tag{4.30}$$

where

$$T(L)T^{-1}(L) = I. \tag{4.31}$$

Thus, if we were to act on the annihilation operators of each mode, we would get

$$T(L)^\dagger a_1(0)T(L) = u(L)a_1(0) + v(L)a_2(0) \tag{4.32}$$

$$T(L)^\dagger a_2(0)T(L) = v(L)a_2(0) + u^*(L)a_2(0) \tag{4.33}$$

which is by definition a beamsplitter. further proof can be found in references [99, 100, 101] which also work on this principle of the transfer matrix method to prove beamsplitter behaviour. Thus, by setting the coefficients to achieve 50/50 splitting, the transfer matrix becomes

$$B(\frac{\pi}{2}) = \frac{1}{\sqrt{2}} \begin{pmatrix} 1 & i \\ i & 1 \end{pmatrix} \tag{4.34}$$

or more generally,

$$B(\theta, \phi) = \begin{pmatrix} \cos(\theta) & -e^{i\phi}\sin(\theta) \\ e^{-i\phi}\sin(\theta) & \cos(\theta) \end{pmatrix} \tag{4.35}$$

where ϕ is the phase induced by the beamsplitter and θ controls the splitting ratio [22]. Furthermore, if we cascade these beamsplitters and phase shifters as shown in figure 4.10, the transfer matrix becomes:

$$\begin{aligned} U &= \frac{1}{2} \begin{pmatrix} 1 & 0 \\ 0 & e^{i\Delta\phi} \end{pmatrix} \begin{pmatrix} 1 & i \\ i & 1 \end{pmatrix} \begin{pmatrix} 1 & 0 \\ 0 & e^{i\Delta\theta} \end{pmatrix} \begin{pmatrix} 1 & i \\ i & 1 \end{pmatrix} \begin{pmatrix} 1 & 0 \\ 0 & e^{i\Delta\chi} \end{pmatrix} \\ U &= \underbrace{\begin{pmatrix} 1 & 0 \\ 0 & e^{i\Delta\phi} \end{pmatrix} \begin{pmatrix} \cos\left(\frac{\theta}{2}\right) & -\sin\left(\frac{\theta}{2}\right) \\ \sin\left(\frac{\theta}{2}\right) & \cos\left(\frac{\theta}{2}\right) \end{pmatrix}}_{\text{single qubit rotation}} \begin{pmatrix} 1 & 0 \\ 0 & e^{i\Delta\chi} \end{pmatrix}. \end{aligned} \tag{4.36}$$

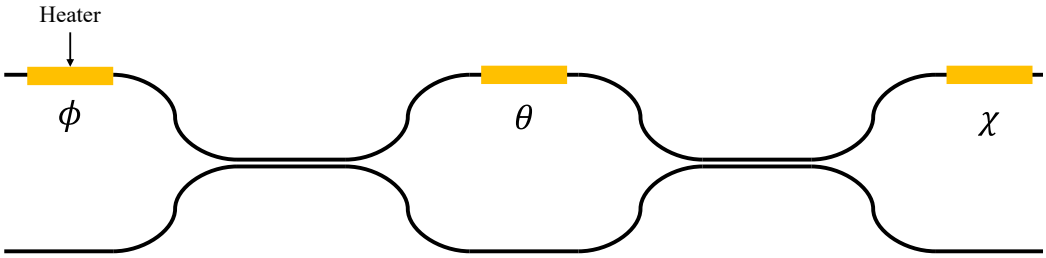

Figure 4.10: Tomography PIC schematic. The yellow blocks represent a resistive heater used to change the index of the waveguide by dissipating heat. Each heater induces a phase, indicated by ϕ, θ, and χ. As indicated by equation 4.36, this structure is capable of performing single qubit rotations, acting as the waveplates in the tomography setup in figure 3.11

This allows us to reach anywhere on the Bloch sphere given any input state. This will become useful when constructing the tomography circuit.

4.2.6 Ring Resonator

So far, we have described methods to guide and split broad bandwidths of light. The dependence on wavelength is important as far as the ability of the waveguide to support particular wavelengths. However, to achieve all the functionality required to perform optical experiments like in the lab, we need the ability to filter narrow bandwidths of light. The chosen method of doing this is by using a structure known as a ring resonator, which uses the principles of coupling and confinement to select specific wavelengths. To understand how they work, we must first describe their geometry and how EM waves interact with a ring, where the rounded portions are of a fixed radius and the portion parallel to the input waveguide is of some coupling length.

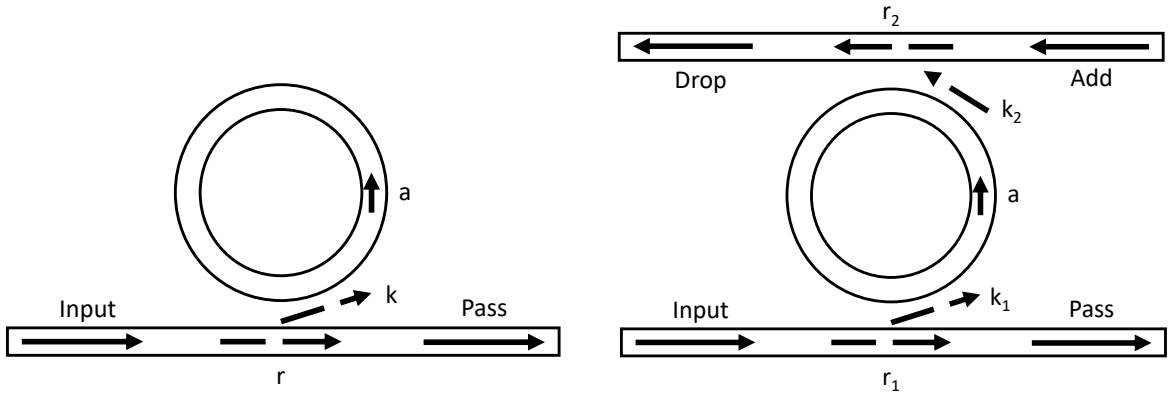

(a) All-pass ring resonator

(b) Add-drop ring resonator

Figure 4.11: Schematic of an a) all-pass and b) add-drop ring resonator.

For simplicity, let's set $L_x = 0$ so the ring resonator becomes a circle. When the waves in the loop build up a round trip phase shift, ϕ, that equals $2\pi m$, where m is some integer, the waves interfere constructively, and the cavity is in resonance [102]. This is a fundamental property of ring resonators oriented in any configuration. To further explore ring resonators, we need to split them into two categories: all-pass, and add-drop resonators, both of which are depicted in figure 4.11.

All-pass Ring Resonator

To derive the basic properties of the all-pass ring resonator, let's assume a continuous wave operation and matching fields, with the assumption of no reflection back into the waveguide from the coupling region. From these assumptions, the ratio of the electric field which does not couple to the ring and the input electric field as:

$$\frac{E_{pass}}{E_{input}} = e^{i(\pi+\phi)}\frac{a - re^{-i\phi}}{1 - rae^{i\phi}}, \tag{4.37}$$

where $\phi = \beta L$. In this instance, ϕ is the single-pass phase shift, L is the round trip length, β is the propagation constant, r is the self-coupling coefficient (more on this shortly), and a is the single-pass amplitude transmission. a is a catch-all term that describes the amplitude of the electric field in the presence of loss. a is related to the power attenuation coefficient, $\alpha[\frac{1}{cm}]$, and the round trip length of the ring through the exponential function:

$$a^2 = e^{-\alpha L}. \tag{4.38}$$

Notice that by squaring equation 4.37, we get the intensity of the transmission, T_n:

$$T_n = \frac{I_{pass}}{I_{input}} = \frac{a^2 - 2ra\cos(\phi) + r^2}{1 - 2ra\cos(\phi) + (ra)^2} \tag{4.39}$$

similar to how we found the transfer function for the directional coupler. Notice that we only have one term to describe the amount of light which pass through the ring resonator uncoupled (or self-coupled), r. If we follow the same steps as with the directional coupler, we can assert that the cross coupling coefficient, k, or the amount of light that couples to the ring, is $r^2 + k^2 = 1$ [102].

With the established relation that the ring is said to be on resonance if the phase is an integer multiple of 2π, we can use the relationship $\phi = \beta L$ to establish a resonance wavelength, i.e. wavelengths that the ring will best couple to.

$$\begin{aligned} \phi &= \beta L \\ 2\pi m &= \frac{2\pi n_{eff}}{\lambda_{res}} L \end{aligned}$$

$$\lambda_{res} = \frac{n_{eff}L}{m}, \qquad m = 1, 2, 3, ... \tag{4.40}$$

where λ_{res} denotes the resonant wavelength, and n_{eff} is the effective refractive index, i.e. the overall refractive index of the component. For completeness, one can also complete the description of the all-pass ring resonator by analyzing equation 4.37 to find

$$\varphi = \pi + \phi + \arctan\left(\frac{r\sin(\phi)}{a - r\cos(\phi)}\right) + \arctan\left(\frac{ra\sin(\phi)}{1 - ra\cos(\phi)}\right). \tag{4.41}$$

Here, we can see that at $r = a$ (critical coupling), the transmission experiences an abrupt π phase shift at the resonance wavelength. For $r < a$ (overcoupling) the transmission experiences a continuous positive phase delay. And finally, for $r > a$ (undercoupling), the phase shift near the resonances shows a strong decrease (2π phase shift) [102].

Finally, it is imperative to find a way to describe the ring in terms of its transmission spectrum. For this, we need to introduce the quantities of full width at half maximum (FWHM) of the resonance spectrum, free spectral range (FSR), finesse, and quality factor (Q-factor). First, we will derive the FWHM, which determines the shape of the resonance spectrum. It describes the range of wavelengths that can couple into the ring resonator. The larger the FWHM, the wider the resonance spectrum. The FWHM is derived in reference [102] and is determined to be:

$$FWHM = \frac{(1 - ra)\lambda_{res}^2}{\pi n_g L\sqrt{ra}}, \tag{4.42}$$

where n_g is the group index (corresponding to the group velocity, $v_g = \frac{c}{n_g}$) and is described by the equation [102, 93]

$$n_g = n_{eff} - \lambda_0\frac{dn_{eff}}{d\lambda} = \frac{\lambda^2}{L\Delta\lambda}. \tag{4.43}$$

Continuing with the derivations, next we will derive the FSR for the ring. FSR is defined as the wavelength range between two resonances. Essentially, it relates the geometry of the waveguide to the resonance wavelengths the ring was designed for. One can describe the FSR by the equation

$$FSR = \frac{\lambda^2}{n_g L}. \tag{4.44}$$

Using the definition of FSR and FWHM, we can define both of the remaining quantities: Finesse and Quality factor. Physically, Finesse describes the sharpness of resonances relative to their spacing [102], and is defined quantitatively by the equation

$$Finesse = \frac{FSR}{FWHM} = \frac{\pi\sqrt{ra}}{1-ra}. \tag{4.45}$$

The quality factor is a measure of the sharpness of the resonance relative to its central frequency and can be described quantitatively by the equation

$$Q - factor = \frac{\lambda_{res}}{FWHM} = \frac{\pi n_g L\sqrt{ra}}{\lambda_{res}(1-ra)}. \tag{4.46}$$

The physical meaning of Finesse relates the number of round trips the light can make before its energy is reduced to $\frac{1}{e}$ or its original value (within a factor of 2π). The Q-factor represents the number of oscillations the light field makes before the energy drops to $\frac{1}{e}$ of its original value. There are two different quantities for the Q-factor: "loaded" and "unloaded" Q-factor. Loaded Q-factor represents the Q-factor of the ring and bus waveguide. Unloaded Q-factor represents the Q-factor of the ring itself. Typically, unless otherwise specified, all mentions of Q-factor will refer to the loaded Q-factor. Because of the extra loss induced by the waveguide and coupling, $Q_{unloaded} > Q_{loaded}$ [102]. With these four quantities, we have everything we need to describe the ring resonator.

Add-drop Ring Resonator

This section heavily piggybacks off the previous section, where all the analysis is the same. The difference being that there are two extra ports where light can leave the ring (drop port), or extra light can be added in (add port). With this in mind, the two transfer functions for the pass and drop ports become:

$$T_p = \frac{I_{pass}}{I_{input}} = \frac{r_2^2a^2 - 2r_1r_2a\cos\phi + r_1^2}{1 - 2r_1r_2a\cos\phi + (r_1r_2a)^2} \tag{4.47}$$

$$T_d = \frac{I_{drop}}{I_{input}} = \frac{(1-r_1^2)(1-r_2^2)a}{1 - 2r_1r_2a\cos\phi + (r_1r_2a)^2} \tag{4.48}$$

where r_1 and r_2 are the self coupling coefficients of the bottom and top waveguide buses, respectively. If there is no attenuation, $a = 1$ and critical coupling will occur when the

cross coupling for both the top and bottom bus is the same. When loss is not negligible, critical coupling occurs when the losses match the coupling in such a way that $r_2 a = r_1$ [102].

Finally, we can derive the four quantitative properties, FWHM, FSR, Finesse, and Q-factor which allow us to completely describe the spectral performance of the ring. First, the FWHM. Like the all-pass ring, the FWHM will consist of the same parameters except with a dependence on the self coupling coefficients for both the top and bottom buses, r_1 and r_2. With this in mind, the FWHM for the add-drop ring looks like:

$$FWHM = \frac{(1 - r_1 r_2 a)\lambda_{res}^2}{\pi n_g L \sqrt{r_1 r_2 a}}. \tag{4.49}$$

Similarly, since the FSR does not depend on the self coupling coefficients, the FSR for bot the all-pass and add-drop rings will be the same:

$$FSR = \frac{\lambda^2}{n_g L}. \tag{4.50}$$

Finally, the Finesse and Q-factor have the same relations as the all-pass ring, but again with a dependence on both self coupling coefficients.

$$Finesse = \frac{FSR}{FWHM} = \frac{\pi\sqrt{r_1 r_2 a}}{1 - r_1 r_2 a}. \tag{4.51}$$

$$Q - factor = \frac{\lambda_{res}}{FWHM} = \frac{\pi n_g L \sqrt{r_1 r_2 a}}{\lambda_{res}(1 - r_1 r_2 a)}. \tag{4.52}$$

With these four quantities for both the all-pass and add-drop rings at the disposal, we now have everything we need to describe passive ring resonators as components used in PIC design.

Ring Resonators Simulation and Results

The ring resonators were simulated using Lumerical's FDTD method. We chose this method because of the ring's importance, and difficulty extrapolating behaviour from any simplified model. We began by placing an add-drop ring of diameter of 120.5 μm, which

was calculated using equation 4.40. The bend radius calculations were needed as a guideline to ensure that there was no loss inside the ring due to the reasons laid the in section 4.2.2. With a value determined from the theory as a reference point, we would vary the radius of the ring until we saw a complete transfer of light from the ring to the drop port. from this, we can conclude that the ring could couple all the light from the input port, support it inside the ring, and complete the transfer to the drop port. Based on the simulation results shown in figures 4.12a and 4.15b, the optimal ring radius was 60.25 μm.

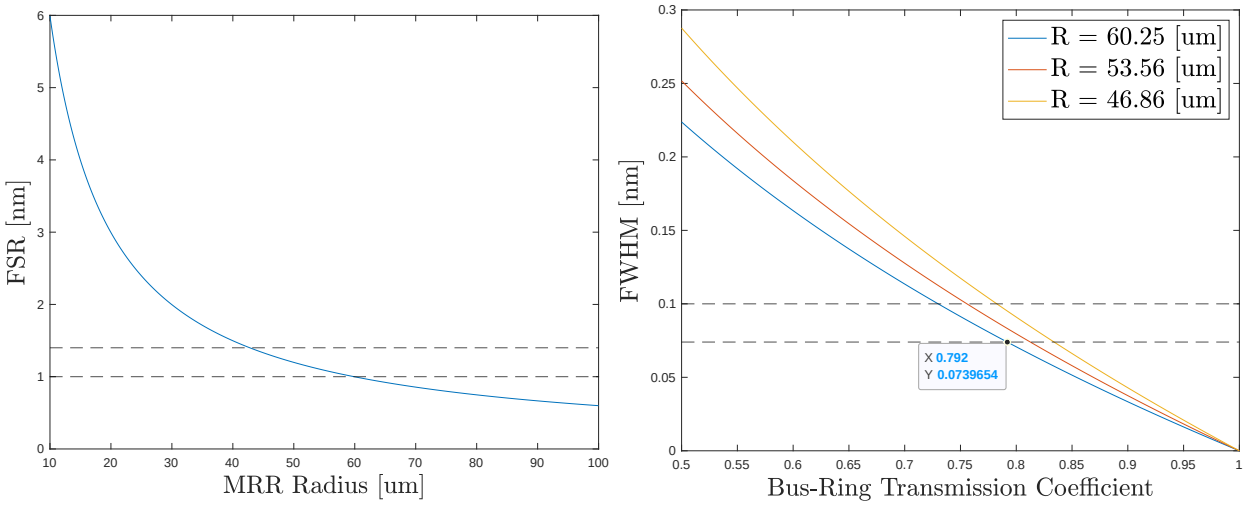

(a) (b)

Figure 4.12: Simulated results for the ring resonator. Both the FSR (a) and FWHM (b) have been simulated, and values were picked based on the performance required for coupling to the QD.

The values were chosen due to a variety of reasons. The first reason being the FSR. The goal of choosing a radius with an appropriate FSR is to ensure the resonances are sufficiently far away as to not couple unwanted light at integer multiple wavelengths from the wavelength of the source. potential sources of this could be white ambient light or scattered light from the excitation laser. The FWHM was chosen to be the same as the XX and X emissions to capture as much light as possible at the emission wavelengths.

4.3 Active Components

The components which have been introduced thus far have assumed a constant environment. This means that the temperature of the PIC will be kept constant to ensure the consistent operation of the components at the desired wavelengths that we designed them for. However, there are some situations in which deviating from the designed wavelengths is desired.

Because the PICs are designed to work with the NWQD source, the components, particularly MZIs and ring resonators, need to work for both wavelengths. One way to address this issue is to induce heat to the components to change the n_{eff} of the material, effectively changing the speed of light in that material. This will artificially increase the path length of the light and will allow us to have a smaller footprint. The smaller footprint comes from the ability to change the n_{eff} at will, as well as having some robustness against factory imperfections. These imperfections can cause deviations in the expected performance of the device. These deviations can be corrected by finding the temperature at which the device was designed to operate and maintain that temperature. Thus, by introducing a method of temperature control, we can greatly reduce the circuit footprint and also have a method of controlling the performance of the devices. Before we delve into the individual components and how they are affected by temperature change, we first need to describe how changing the temperature affects the material in which they are made of.

Firstly, we start with the steady-state heat equation, also known as Poisson's equation:

$$-\nabla \cdot (k\nabla T) = Q \tag{4.53}$$

where k is the heat conduction coefficient, T is the temperature, and Q is the heat source in units of $\frac{W}{m^3}$. However, we do not want the volumetric power, as it is not a quantity that is directly measurable using standard lab equipment. We need to know the power dissipated by the heater to change the temperature the required amount to induce a phase shift, i.e. $Q_{tot} = QV$. From this, we can find the voltage needed to change the refractive index of the waveguide. If we assume a Neumann type boundary condition, the heat flux is $-n \cdot (k\nabla T)$. Finally, by using the definition of FSR being equivalent to a 2π phase shift, we can determine the efficiency of the heater [93]. in other words, combining all the assumptions and assertions, we have:

$$efficiency\left[\frac{mW}{FSR}\right] = \frac{Q_{tot}\lambda}{\frac{dn}{dT}\Delta T} \tag{4.54}$$

where $\frac{dn}{dT}$ is an intrinsic property of the material and tells us how the refractive index changes as a function of temperature. This can be found in various online material databases.

Finding V_π

Before we delve into the active components section, it is important to state that no simulations were done on these components directly. Instead, the simulation was focused on determining the amount of heat that was needed to be transferred to the waveguide to change the refractive index enough to induce a π phase shift. This simulation was carried out using Lumerical's HEAT simulation environment, which allows for the modelling of such situations.

The simulation begins with the initialization of the components. This is realized by a cross-section of the heater, waveguide, substrate, and cladding. Because AMF has hard limitations on which materials can be deposited on which layers, the waveguide, and heater distance is fixed. Lumerical's material database has most of the necessary constants associated with this simulation, however, the change in refractive index with respect to temperature for SiN_x, $\frac{dn_{eff}}{dT}$ was not. The value for $\frac{dn_{eff}}{dT} = 2.51e^{-5}$ for SiN_x was found in reference [103]. After running the simulation, it can be determined the power needed to be dissipated by the heater to induce the required phase shift, P_π. By using the equation $P = \frac{V^2}{R}$, where R can be measured, therefore V_π can be determined.

4.3.1 Heated Mach-Zehnder Interferometer

The purpose of the MZIs in the circuit is to induce qubit rotation around the Bloch sphere. This allows is to effectively replicate the tomography setup. However, static MZIs are not useful, since they would only allow us to deterministically rotate the state to a singular point on the Bloch sphere. The heated MZIs are needed to dynamically change the state we are rotating to anywhere on the Bloch sphere. By placing heaters in the locations as shown in figure 4.10, we will have full control to rotate the entangled photons onto any state we desire.

4.3.2 Heated Ring Resonator

The primary purpose of a ring resonator in the circuits is for filtering photons of different wavelengths. With a high enough Q-factor and Finesse, we can design the ring resonators

to only couple the XX or X photons from the NWQD. By using the add-drop configuration, we can use this filtering for routing of photons into different parts of the tomography setup. However, like the MZIs, the rings are also not immune to manufacturer defects, which can cause deviations from the desired performance. For example, the typical wavelengths of the XX and X photons are 894.67 nm and 893.25 nm, with FWHM linewidths of 0.07 nm. A deviation from the centre wavelength, Q-factor and Finesse may cause the rings to couple to both the XX and X photons, resulting in an inability to filter one from the other.

Similar to the heated MZI, heating a ring resonator can also add resilience to their design. Because the allowed modes inside the ring depend on integer multiples of the lights' wavelength, changing the temperature of the rings can change it's n_{eff}, changing the travel distance relative to the light in the unheated waveguide, effectively changing the supported wavelengths inside the ring. This allows us to actively select either the XX or X photons, depending on where we want to route the photons.

4.4 Circuit I/O

Thus far, we have discussed how we can manipulate light that was already on the chip, without wondering how it got there. However, this overlooks one of, if not the most important steps in PIC design. And that is "how do we get light onto the chip in the first place"? That is what we will be addressing in this section.

Waveguides are typically in the hundreds of nanometres in width and height, resulting in a tiny mode size. Typically, before the light has entered into the PIC, it was generated and transported in free space or coupled into fibre. One way around this is to place the source on the PIC and generate the light on-chip [104, 105, 106]. However, growing many sources on a chip can be difficult to scale due to the light from the QDs being unpolarized[7] and the techniques used to suppress the excitation laser result in half of the photons unable to couple to the waveguides fundamental mode [107]. To mitigate this, we take on three approaches:

1. Coupling in plane,
2. Coupling out of plane, and
3. Convert polarization entanglement to path entanglement.

[7] Emitting $|H\rangle$ and $|V\rangle$ light with equal probability.

These methods assume that the waveguides are optimized to support both TE and TM modes, and no excitation light will be entering the chip. The first method involves some processing of the light to be done before reaching the chips to separate the $|H\rangle$ and $|V\rangle$ light. the second method requires no separation of the $|H\rangle$ and $|V\rangle$ light. The next sections will be exploring each of these methods.

4.4.1 Grating Coupler

A grating couplers' objective is to diffract light from free space (out of plane) onto the waveguide (in plane) and vice versa. It consists of periodic structures typically made of the waveguide material. These gratings work on the Bragg grating principal, which can be visualized in figure 4.13

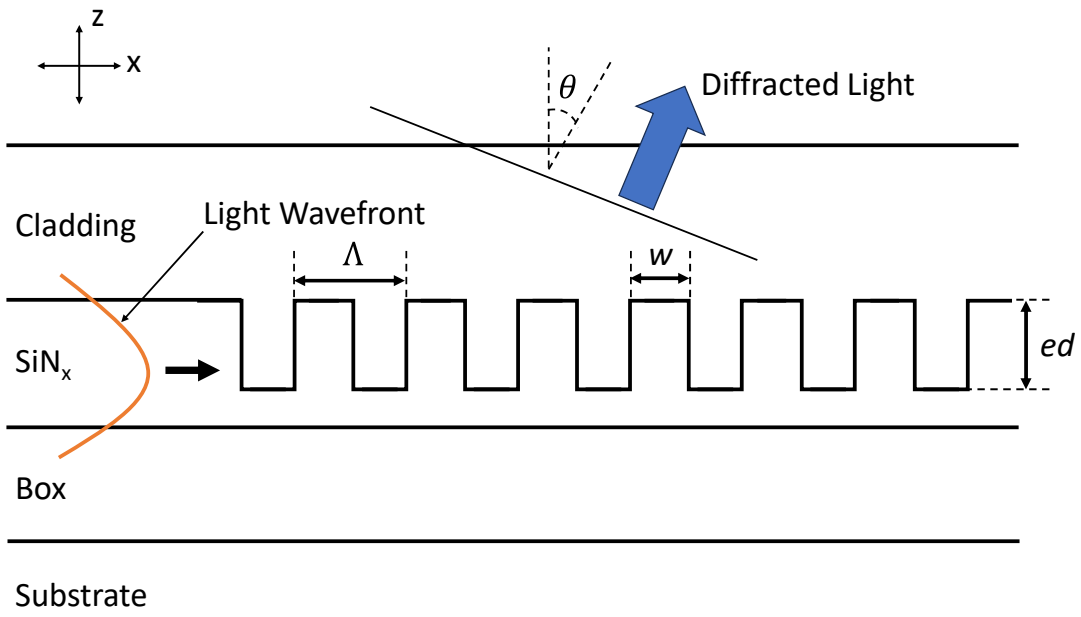

Figure 4.13: Cross-section schematic of a grating coupler, with all important variables to be considered in a design process labeled.

where each of the labelled variables represent design parameters for the grating. The design parameters are as follows:

1. Cladding/BOX: SiO_2 layers to protect the waveguide structures.

2. SiN_x: The layer where the dielectric material will be deposited. Light is confined in this layer.

3. Λ: Period of the grating.

4. W: Width of the grating teeth.

5. ff: Fill factor (or duty cycle) of the grating. This is defined as $f = \frac{W}{\Lambda}$.

6. ed: Etch depth of the grating teeth.

7. θ_c: The angle between the surface and the propagation direction of the diffracted light in the cladding.

8. θ_{air}: The angle between the surface and the propagation direction of the diffracted light in the air.

9. θ_{fibre}: The angle between the surface and the propagation direction of the diffracted light in the fibre, corresponding to the polish angle of the fibre array[8].

With the design parameters identified, next we can talk about the theory of how Bragg gratings work.

Grating couplers can be understood in terms of the Huygens-Fresnel principal [93]. This principle describes the constructive and destructive interference that occurs when light travels through a grating structure. With this, in conjunction with the Bragg Law, we can fully describe the light-matter interactions happening inside the one-dimensional grating shown in figure 4.13.

The propagation constant inside the waveguide can be described by

$$\beta = \frac{2\pi n_{eff}}{\lambda_0} \tag{4.55}$$

where λ_0 is the optical wavelength of the light. The Bragg Law allows us to describe how light propagates through a grating structure. This relation can be expressed as

$$\beta - k_x = mK \tag{4.56}$$

[8]This refers to a device known as a v-groove. V-grooves are devices which contain an array of equally spaced fibre cores which can be used to couple vertically into grating couplers.

where k_x is the component of the wave vector of the diffracted wave in the direction of the incident wave (horizontal component), K is the periodicity of the grating and can be described as $K = \frac{2\pi}{\Lambda}$, and m is the diffraction order. You can consider the zeroth order diffraction to represent no diffraction, i.e. a reflection. Thus, we are only interested in conditions where $m > 0$. However, we can further narrow the values of m by analyzing what happens to the diffracted beam for different values of m.

We can use Snell's Law to show the relation between the period of the grating and the wavevectors of the light. By drawing a k-diagram to show the wavevectors for the Bragg grating, we can determine that the diffracted angle of light in the cladding (incident to the grating), θ_c, is:

$$\sin(\theta_c) = \frac{k_x}{k} = n_{eff}\frac{\lambda}{\Lambda}. \tag{4.57}$$

By substituting in $k = \frac{2\pi n_c}{\lambda}$, the Bragg condition can be simplified to

$$n_{eff} - n_c \sin(\theta_c) = \frac{\lambda}{\Lambda}. \tag{4.58}$$

Thus, by having knowledge of the indices of refraction of the system, the period of the grating, and the wavelength of the light, we have equations that fully describe how light will interact with the grating.

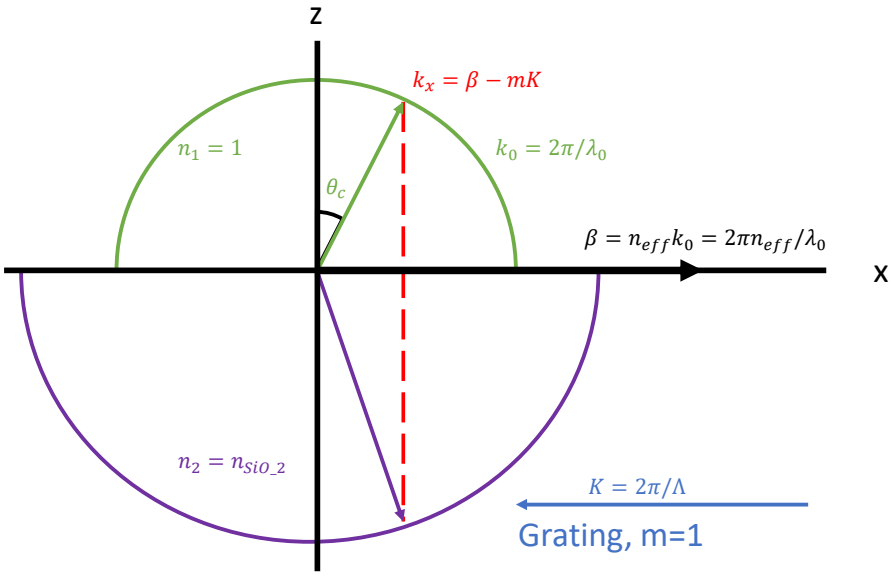

Figure 4.14: K-diagram showing the Bragg conditions for the grating in figure 4.15a

The Bragg condition states that the first order refraction will propagate vertically, while the second order refraction will propagate back into the waveguide. This is undesired back reflection, which can lead to Fabry-Perot oscillations between the input coupler and output coupler [93]. To avoid this, we can tune the gratings to slightly mismatch the Bragg condition for the wavelength of the source. The desired condition to prevent back reflection is $\frac{\lambda_0}{n_{eff}} < \Lambda$, which will result in the first order refraction (which used to be straight up) to diffract at some angle. This also means that if we want to couple the emission into fibre, we also have to polish the fibres at this angle to maximize the coupling. This angle can be designed for using Lumerical, which we will explore in the next section.

4.4.2 Grating Coupler Simulation Results

Before the grating coupler could be simulated, there needed to be an understanding of the limitations of the AMF platform. These limitations drastically shape the geometry of the grating coupler, as it will typically limit its performance in some way. For example, the minimum spacing between components in the AMF platform is 400 nm. This limits the spacing of the grating teeth to a minimum of 400 nm. For example, if it was found that the optimum coupling occurs when the teeth spacing of the gratings is 300 nm, it will be impossible to fabricate because of AMF specifications.

With the geometry limitations due to AMF established, we can begin designing the grating coupler. The grating coupler was designed as per figure 4.13, with some modifications. the first modification is with the grating teeth. Due to the limitations of SiN_x deposition, there will be either SiN_x at a fixed thickness (400 nm) or no SiN_x. Meaning, the teeth are separated by oxide with no thin layer at the base of each of the teeth to connect them, like in figure 4.13. The second feature which we deviated from is the fill factor. Because of the minimum feature size (300 nm) and minimum spacing requirement (400 nm), we have decided to fix the fill factor.

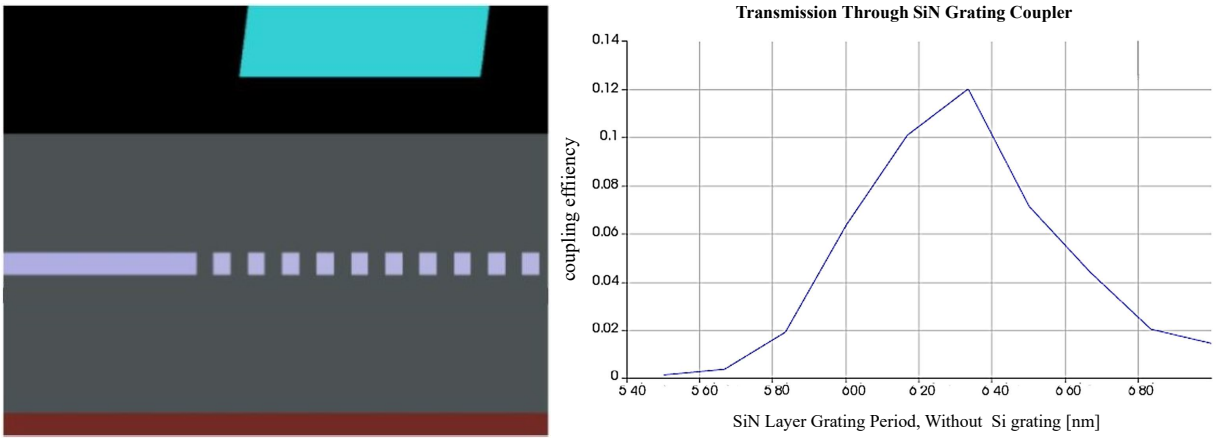

(a) (b)

Figure 4.15: 2D FDTD simulation (a) and data (b) for a SiN_x grating coupler. The fibre core (teal) is polished at an angle of 10°, which is typical of fibre arrays used in these situations. This is also to improve the grating coupler efficiency. The fibre is placed at some distance away from the grating coupler, separate by air (black). The grating coupler is clad in SiO_2 (grey) which both protects the waveguide and provides an interface which aids in the confinement of light. The SiN_x grating (purple) is placed above the Si substrate (red), which the entire circuit sits upon.

The period of the grating, however, is perfectly acceptable to vary. After varying the period, we found the optimum transmission occurs at $\Lambda = 0.63\mu m$. Finally, we varied the angle of the fibre to see the optimum position which the fibre would have to be polished in an experimental setup to achieve maximum coupling, which was determined to be $\theta = 10°$. Ultimately, the maximum coupling efficiency of the grating coupler in figure 4.15a was 12% at a wavelength of 894 nm, which is far too low to perform experiments with single photons in a reasonable amount of time.

With low transmission, we were looking for another way to improve the performance while adhering to AMF design limitations. It was found that by placing a Si "mirror" underneath the SiN_x grating could improve coupling performance [108, 109]. However, at the wavelengths, the spacing between the Si mirror and the SiN_x grating is smaller than the wavelength of the source. This would result in the light seeing the entire structure, creating a single n_{eff} for both gratings as a whole. With this in mind, we added a second grating underneath the initial SiN_x grating and performed the same parameter sweep on this grating too.

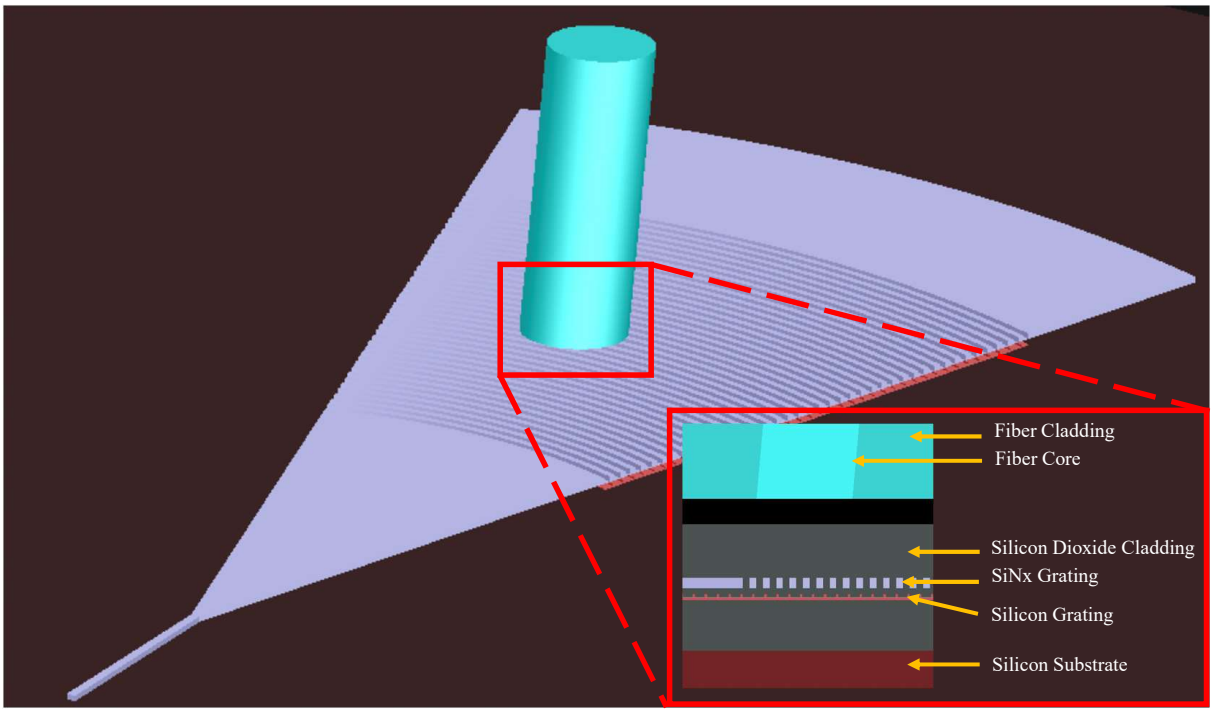

Figure 4.16: 3D FDTD simulation of a dual-layered grating coupler. A cross-section can be seen in the bottom right corner of the image, where each of the components which the grating coupler consists of can be seen.

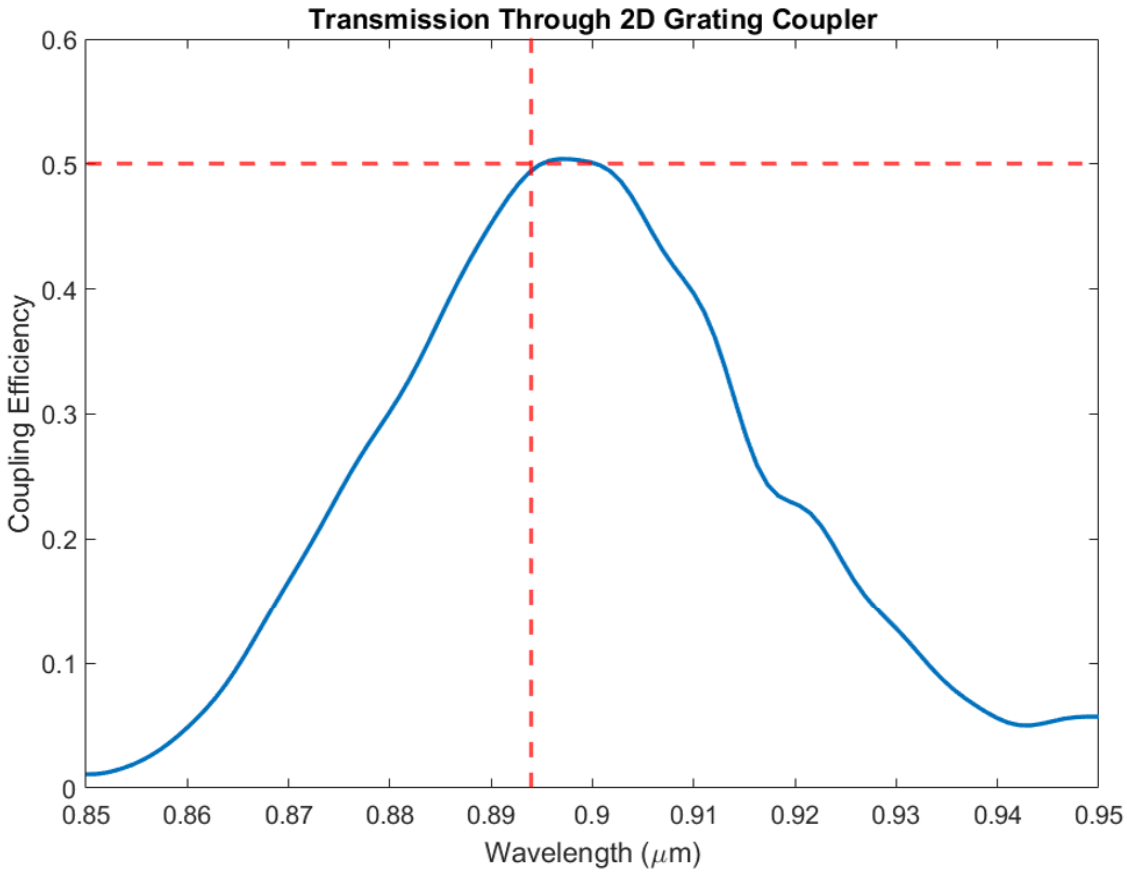

Figure 4.17: 3D FDTD results for dual-layered grating coupler. Dashed red lines have been added to indicate the coupling efficiency at the operating wavelength, 50% coupling efficiency at 894nm.

To increase the efficiency of the simulation, a 3D FDTD was performed. The Lumerical model is shown in figure 4.16, with the data being shown in 4.17. This will give us maximum accuracy to what we expect to see in experimental settings. With the Si grating structure underneath the SiN_x grating, the transmission efficiency increased from 12% to 50% at the desired wavelength.

4.4.3 Edge Coupler

Edge couplers allow us to couple in-plane light onto the chip, as seen in figure 4.18. It works on the same principal as the nanowire; adiabatically expanding/contracting the mode of the light until it can be coupled to either a fibre, objective lens (in the case of the NWQD), or the chip. What allows for the adiabatic of the edge coupler is the tapered design, as shown in figure 4.19, in which the mode from the waveguide can gradually become less confined as it travels down a gradually tapered waveguide, as shown in figure 4.20. Being an adiabatic process, the amount of loss for edge coupling onto the chip is low, often below 0.5dB [110, 111], and polarization invariant [93].

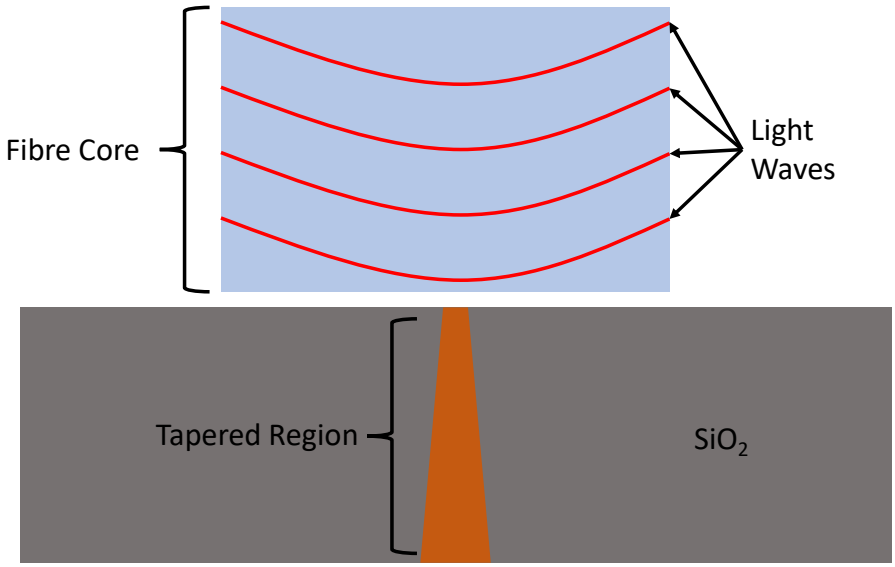

Figure 4.18: Schematic of optical fibre coupled to an edge coupler. The fibre is placed close to the edge of the chip to ensure maximum coupling. Light propagates from the fibre, in which its spacial mode is much larger than that of the waveguide, to the edge coupler where it can be adiabatically confined to the waveguide.

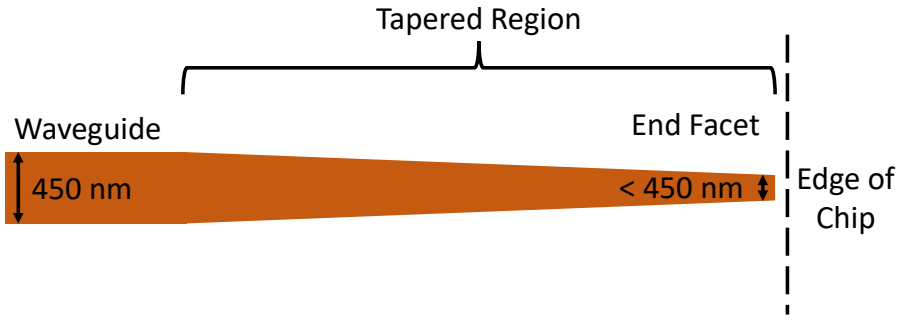

Figure 4.19: Sample design of an edge coupler. An edge coupler is placed at the edge of the chip. The edge coupler consists of the waveguide, tapered region, and end facet.

For the purposes of simulation, we will assume the same initial conditions for the light as we did with the grating coupler; light begins inside the waveguide and couples to the fibre after leaving the chip. Ideally, the taper will converge to a knife-edge like end facet width, but due to manufacturing restraints[9] it is unfeasible. Thus, we need to design for these restrictions. Also, being in plane with the light, there is also the probability of back-reflection due to the refractive index mismatch between the air and waveguide. However, this can be mitigated with anti-reflection coatings. This will contribute to loss, however, but will mitigate any Fabry-Perot behaviour which can happen as light continuously reflects between the fibre and chip surfaces.

[9]Will be discussed further in the simulation section.

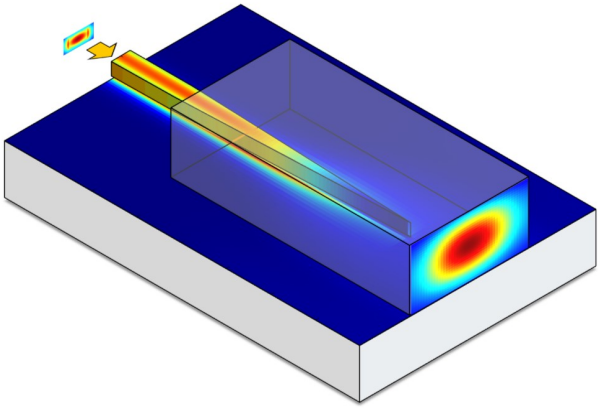

Figure 4.20: Lumerical image of how the mode of the waveguide is adiabatically expanded to match the mode of a fibre. Image taken from [4] and licensed under CC BY 4.0.

4.4.4 Edge Coupler Simulation Results

The edge couplers were simulated using Lumerical's eigenmode expansion solver, which is shown in figure 4.21. The simplicity of the edge coupler design makes the simulation rather trivial; vary the length of the tapered region for a fixed facet width of 300 nm, which is AMFs' minimum feature size. In conjunction with this, a 3 μm waveguide was overlaid on the edge coupler with a 3% index contrast which is deposited to the end of the chip. Finally, coupling to a Gaussian beam with a numerical aperture of 0.4 is performed, which emulate insertion loss to a high-NA optical fibre.

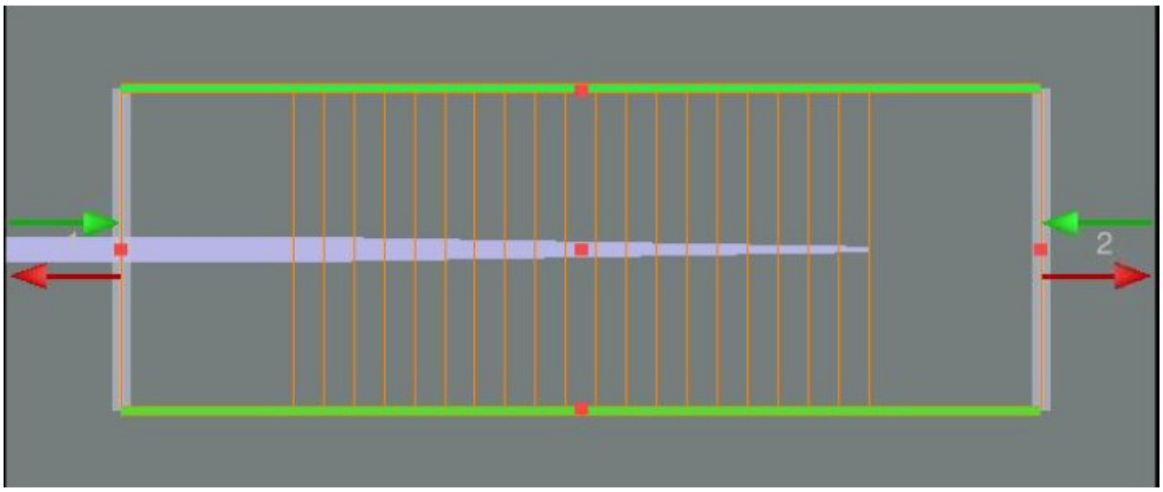

Figure 4.21: Lumerical EME design for an edge coupler. Various end facet widths were used to determine the best dimensions for maximum transmission.

Figure 4.22 shows that as the end facet of the edge coupler becomes thinner, in conjunction with the longer taper length, the transmission into the fibre is increased. This is because the process of expanding the mode becomes more adiabatic, allowing a seamless (and lossless) change in mode size. However, the AMF limitations on feature size limits the end facet width to 300 nm, meaning post-processing must be done to shape the edge couplers to the appropriate size to maximize transmission. Choosing a taper length of 300 μm, combined with post-processing the end facet down to 50 nm, will allow for the near 100% transmission value shown in figure 4.22.

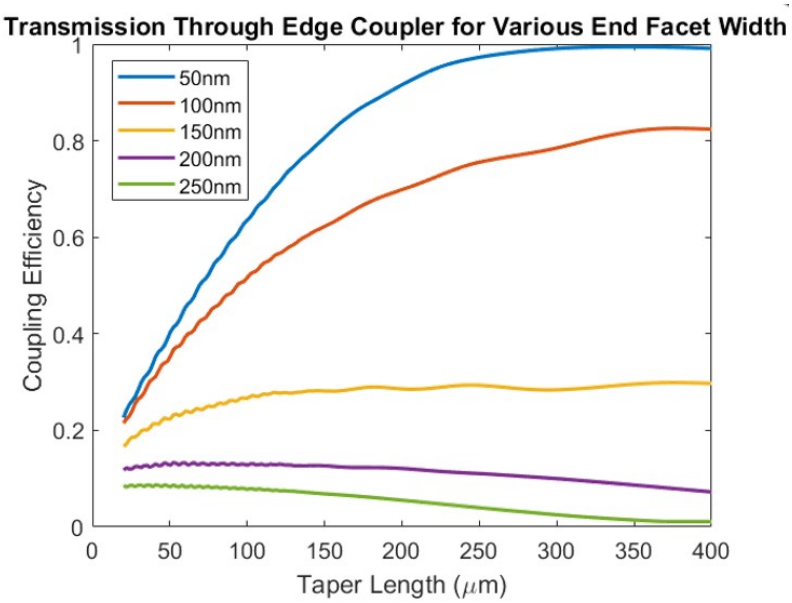

Figure 4.22: Simulation data of edge coupler for various end facet widths (shown in the varying colours). One can see that as the end facet width shrinks, the coupling of the Gaussian mode light is higher. This is because of the adiabatic transition between the size of the free space and confined modes.

Chapter 5

Conclusion and Future Work

Single photon sources are increasing in quality, and the detection systems used to measure the single photons are also improving. This work has provided ample evidence that NWQDs are a viable platform for generating highly entangled pairs of photons with high single photon purity through means of TPRE. This thesis shows that TPRE is the optimum method of generating entangled photons because of its low probability of generating charges near the QD, resulting in high values of concurrence and fidelity which maintain its coherence for longer times than that of other excitation methods. This work also shows that by using faster detection systems with lower timing jitter provide more accurate representations of the state of the QD, with higher values of concurrence and fidelity. This increase in entanglement quantities are simply from a change in excitation technique and measurement apparatus, meaning QDs may be of a higher quality than originally theorized. Even in the presence of FSS, if the detection system is fast enough to resolve the oscillating state in time, the state can still be highly entangled.

With the ever-growing field of single photon sources and PICs, it is becoming evident that marrying the two technologies can provide some promising results. Other materials are being developed, such as SiN_x, which are capable of supporting wavelengths outside the typical Si platform, opening new avenues for future experimentation with other QDs. In this work, we proposed various components which are used in a wide variety of PIC experiments, which are compatible with QDs emitting in the NIR spectrum, given that the devices are shown to provide adequate suppression (>100dB) [112] of unwanted light.

Future work will focus on improving the pair extraction efficiency of the NWQD by building gates around the nanowire to drag charges away from the QD or by optically emptying the XX state to mitigate blinking, and characterizing and testing these circuits

with our NWQD source. First, a sweep of the transmission spectrum will be done for the passive components, and then the active components. Voltages will be applied to the active components to determine the true V_π, as there are likely manufacturing deviations. Finally, when the PICs have been fully tested and characterized, the next step will be integrating our NWQD emissions onto the chip and performing basic experiments, such as two-photon interference and basic state projection, before leading into a full on-chip version of QST.

Letters of Copyright Permission

RightsLink

Sign in/Register

Dephasing Free Photon Entanglement with a Quantum Dot

Author: A. Fognini, A. Ahmadi, M. Zeeshan, et al
Publication: ACS Photonics
Publisher: American Chemical Society
Date: Jul 1, 2019

Quick Price Estimate

This service provides permission for reuse only. If you do not have a copy of the portion you are using, you may copy and paste the content and reuse according to the terms of your agreement. Please be advised that obtaining the content you license is a separate transaction not involving RightsLink.

If credit is given to another source for the material you requested from RightsLink, permission must be obtained from that source.

Note: Individual Scheme and Structure reuse is free of charge and does not require a license. If the scheme or structure is identified as a Figure in the article, permission is required.

Permission for this particular request is granted for print and electronic formats, and translations, at no charge. Figures and tables may be modified. Appropriate credit should be given. Please print this page for your records and provide a copy to your publisher. Requests for up to 4 figures require only this record. Five or more figures will generate a printout of additional terms and conditions. Appropriate credit should read: "Reprinted with permission from {COMPLETE REFERENCE CITATION}. Copyright {YEAR} American Chemical Society." Insert appropriate information in place of the capitalized words.

I would like to...	reuse in a Thesis/Dissertatio	Format	Print and Electronic
Requestor Type	Non-profit	Select your currency	CAD - $
Portion	Table/Figure/Micrograph	Quick Price	Click Quick Price
Number of Table/Figure/Micrograp	1		

QUICK PRICE CONTINUE

To request permission for a type of use not listed, please contact the publisher directly.

Marketplace

Order Confirmation

Thank you, your order has been placed. An email confirmation has been sent to you. Your order license details and printable licenses will be available within 24 hours. Please access Manage Account for final order details.

This is not an invoice. Please go to manage account to access your order history and invoices.

CUSTOMER INFORMATION

Payment by invoice: You can cancel your order until the invoice is generated by contacting customer service.

Billing Address

Mr. Brady Cunard
University of Waterloo
200 University Ave W
Waterloo, ON N2L3G1
Canada

(519) 888-4567
blscunar@uwaterloo.ca

Customer Location

Mr. Brady Cunard
University of Waterloo
200 University Ave W
Waterloo, ON N2L3G1
Canada

PO Number (optional)

N/A

Payment options

Invoice

PENDING ORDER CONFIRMATION

Confirmation Number: Pending

Order Date: 14-Jan-2024

References

[1] Peter Michler. *Quantum dots for quantum information technologies*, volume 237. Springer, 2017.

[2] Marijn AM Versteegh, Michael E Reimer, Klaus D Jöns, Dan Dalacu, Philip J Poole, Angelo Gulinatti, Andrea Giudice, and Val Zwiller. Observation of strongly entangled photon pairs from a nanowire quantum dot. *Nature communications*, 5(1):5298, 2014.

[3] A Fognini, A Ahmadi, M Zeeshan, JT Fokkens, SJ Gibson, N Sherlekar, SJ Daley, D Dalacu, PJ Poole, KD Jöns, et al. Dephasing free photon entanglement with a quantum dot. *ACS Photonics*, 6(7):1656–1663, 2019.

[4] Ansys Lumerical. https://www.lumerical.com/, 2023.

[5] Jonathan A Jones. Nmr quantum computation. *Progress in Nuclear Magnetic Resonance Spectroscopy*, 38(4):325–360, 2001.

[6] Colin D Bruzewicz, John Chiaverini, Robert McConnell, and Jeremy M Sage. Trapped-ion quantum computing: Progress and challenges. *Applied Physics Reviews*, 6(2), 2019.

[7] Xin Zhang, Hai-Ou Li, Gang Cao, Ming Xiao, Guang-Can Guo, and Guo-Ping Guo. Semiconductor quantum computation. *National Science Review*, 6(1):32–54, 2019.

[8] JR Weber, WF Koehl, JB Varley, Anderson Janotti, BB Buckley, CG Van de Walle, and David D Awschalom. Quantum computing with defects. *Proceedings of the National Academy of Sciences*, 107(19):8513–8518, 2010.

[9] B Gouraud, D Maxein, A Nicolas, O Morin, and J Laurat. Demonstration of a memory for tightly guided light in an optical nanofiber. *Physical review letters*, 114(18):180503, 2015.

[10] Peter W Shor. Algorithms for quantum computation: discrete logarithms and factoring. In *Proceedings 35th annual symposium on foundations of computer science*, pages 124–134. Ieee, 1994.

[11] PG Kwiat, JR Mitchell, PDD Schwindt, and AG White. Grover's search algorithm: an optical approach. *Journal of Modern Optics*, 47(2-3):257–266, 2000.

[12] Albert Einstein. Über einen die erzeugung und verwandlung des lichtes betreffenden heuristischen gesichtspunkt, 1905.

[13] William K Wootters. Entanglement of formation of an arbitrary state of two qubits. *Physical Review Letters*, 80(10):2245, 1998.

[14] Ingemar Bengtsson and Karol Życzkowski. *Geometry of quantum states: an introduction to quantum entanglement*. Cambridge university press, 2017.

[15] Wang An-Min. A simplified and obvious expression of concurrence in wootters' measure of entanglement of a pair of qubits. *Chinese physics letters*, 20(11):1907, 2003.

[16] Frank Verstraete and Henri Verschelde. Fidelity of mixed states of two qubits. *Physical Review A*, 66(2):022307, 2002.

[17] Lucas Schweickert, Klaus D Jöns, Katharina D Zeuner, Saimon Filipe Covre da Silva, Huiying Huang, Thomas Lettner, Marcus Reindl, Julien Zichi, Rinaldo Trotta, Armando Rastelli, et al. On-demand generation of background-free single photons from a solid-state source. *Applied Physics Letters*, 112(9), 2018.

[18] Inbal Friedler, Christophe Sauvan, Jean-Paul Hugonin, Philippe Lalanne, Julien Claudon, and Jean-Michel Gérard. Solid-state single photon sources: the nanowire antenna. *Optics express*, 17(4):2095–2110, 2009.

[19] Chong-Ki Hong, Zhe-Yu Ou, and Leonard Mandel. Measurement of subpicosecond time intervals between two photons by interference. *Physical review letters*, 59(18):2044, 1987.

[20] Kazuya Takemoto, Yoshihiro Nambu, Toshiyuki Miyazawa, Yoshiki Sakuma, Tsuyoshi Yamamoto, Shinichi Yorozu, and Yasuhiko Arakawa. Quantum key distribution over 120 km using ultrahigh purity single-photon source and superconducting single-photon detectors. *Scientific reports*, 5(1):14383, 2015.

[21] F Basso Basset, Michele B Rota, Christian Schimpf, Davide Tedeschi, Katharina D Zeuner, SF Covre Da Silva, Marcus Reindl, Val Zwiller, Klaus D Jöns, Armando Rastelli, et al. Entanglement swapping with photons generated on demand by a quantum dot. *Physical Review Letters*, 123(16):160501, 2019.

[22] Emanuel Knill, Raymond Laflamme, and Gerald J Milburn. A scheme for efficient quantum computation with linear optics. *nature*, 409(6816):46–52, 2001.

[23] Pieter Kok, William J Munro, Kae Nemoto, Timothy C Ralph, Jonathan P Dowling, and Gerard J Milburn. Linear optical quantum computing with photonic qubits. *Reviews of modern physics*, 79(1):135, 2007.

[24] Joël Bleuse, Julien Claudon, Megan Creasey, Nitin S Malik, Jean-Michel Gérard, Ivan Maksymov, Jean-Paul Hugonin, and Philippe Lalanne. Inhibition, enhancement, and control of spontaneous emission in photonic nanowires. *Physical review letters*, 106(10):103601, 2011.

[25] Feng Liu, Alistair J Brash, John O'Hara, Luis MPP Martins, Catherine L Phillips, Rikki J Coles, Benjamin Royall, Edmund Clarke, Christopher Bentham, Nikola Prtljaga, et al. High purcell factor generation of indistinguishable on-chip single photons. *Nature nanotechnology*, 13(9):835–840, 2018.

[26] JC Loredo, MA Broome, P Hilaire, O Gazzano, I Sagnes, A Lemaitre, MP Almeida, P Senellart, and AG White. Boson sampling with single-photon fock states from a bright solid-state source. *Physical review letters*, 118(13):130503, 2017.

[27] Pascale Senellart, Glenn Solomon, and Andrew White. High-performance semiconductor quantum-dot single-photon sources. *Nature nanotechnology*, 12(11):1026–1039, 2017.

[28] Peter Grünwald. Effective second-order correlation function and single-photon detection. *New Journal of Physics*, 21(9):093003, 2019.

[29] Peter Michler, Alper Kiraz, Christoph Becher, WV Schoenfeld, PM Petroff, Lidong Zhang, Ella Hu, and A Imamoglu. A quantum dot single-photon turnstile device. *science*, 290(5500):2282–2285, 2000.

[30] Sonia Buckley, Kelley Rivoire, and Jelena Vučković. Engineered quantum dot single-photon sources. *Reports on Progress in Physics*, 75(12):126503, 2012.

[31] R Hanbury Brown and Richard Q Twiss. Correlation between photons in two coherent beams of light. *Nature*, 177(4497):27–29, 1956.

[32] Adrien Dousse, Jan Suffczyński, Alexios Beveratos, Olivier Krebs, Aristide Lemaître, Isabelle Sagnes, Jacqueline Bloch, Paul Voisin, and Pascale Senellart. Ultrabright source of entangled photon pairs. *Nature*, 466(7303):217–220, 2010.

[33] N Akopian, NH Lindner, E Poem, Y Berlatzky, J Avron, D Gershoni, BD Gerardot, and PM Petroff. Entangled photon pairs from semiconductor quantum dots. *Physical review letters*, 96(13):130501, 2006.

[34] Robert J Young, R Mark Stevenson, Paola Atkinson, Ken Cooper, David A Ritchie, and Andrew J Shields. Improved fidelity of triggered entangled photons from single quantum dots. *New Journal of Physics*, 8(2):29, 2006.

[35] R Hafenbrak, SM Ulrich, P Michler, L Wang, A Rastelli, and OG Schmidt. Triggered polarization-entangled photon pairs from a single quantum dot up to 30 k. *New Journal of Physics*, 9(9):315, 2007.

[36] Andreas Muller, Wei Fang, John Lawall, and Glenn S Solomon. Creating polarization-entangled photon pairs from a semiconductor quantum dot using the optical stark effect. *Physical review letters*, 103(21):217402, 2009.

[37] Matteo Pennacchietti, Brady Cunard, Shlok Nahar, Mohd Zeeshan, Sayan Gangopadhyay, Philip J Poole, Dan Dalacu, Andreas Fognini, Klaus D Jöns, Val Zwiller, et al. Oscillating photonic bell state from a semiconductor quantum dot for quantum key distribution. *arXiv preprint arXiv:2307.06473*, 2023.

[38] Michael A Nielsen and Isaac L Chuang. *Quantum computation and quantum information*. Cambridge university press, 2010.

[39] Lars S Madsen, Fabian Laudenbach, Mohsen Falamarzi Askarani, Fabien Rortais, Trevor Vincent, Jacob FF Bulmer, Filippo M Miatto, Leonhard Neuhaus, Lukas G Helt, Matthew J Collins, et al. Quantum computational advantage with a programmable photonic processor. *Nature*, 606(7912):75–81, 2022.

[40] Frédéric Bouchard, Alicia Sit, Yingwen Zhang, Robert Fickler, Filippo M Miatto, Yuan Yao, Fabio Sciarrino, and Ebrahim Karimi. Two-photon interference: the hong–ou–mandel effect. *Reports on Progress in Physics*, 84(1):012402, 2020.

[41] Benjamin Kambs and Christoph Becher. Limitations on the indistinguishability of photons from remote solid state sources. *New Journal of Physics*, 20(11):115003, 2018.

[42] Natasha Tomm, Alisa Javadi, Nadia Olympia Antoniadis, Daniel Najer, Matthias Christian Löbl, Alexander Rolf Korsch, Rüdiger Schott, Sascha René Valentin, Andreas Dirk Wieck, Arne Ludwig, et al. A bright and fast source of coherent single photons. *Nature Nanotechnology*, 16(4):399–403, 2021.

[43] Liang Zhai, Matthias C Löbl, Giang N Nguyen, Julian Ritzmann, Alisa Javadi, Clemens Spinnler, Andreas D Wieck, Arne Ludwig, and Richard J Warburton. Low-noise gaas quantum dots for quantum photonics. *Nature communications*, 11(1):4745, 2020.

[44] Peter Lodahl, Arne Ludwig, and Richard J Warburton. A deterministic source of single photons. *Physics Today*, 75(3):44–50, 2022.

[45] Luca Sapienza, Marcelo Davanço, Antonio Badolato, and Kartik Srinivasan. Nanoscale optical positioning of single quantum dots for bright and pure single-photon emission. *Nature communications*, 6(1):7833, 2015.

[46] Sebastian Tamariz, Gordon Callsen, Johann Stachurski, Kanako Shojiki, Raphaël Butté, and Nicolas Grandjean. Toward bright and pure single photon emitters at 300 k based on gan quantum dots on silicon. *Acs Photonics*, 7(6):1515–1522, 2020.

[47] Satoshi Kako, Charles Santori, Katsuyuki Hoshino, Stephan Götzinger, Yoshihisa Yamamoto, and Yasuhiko Arakawa. A gallium nitride single-photon source operating at 200 k. *Nature materials*, 5(11):887–892, 2006.

[48] Amanuel M Berhane, Kwang-Yong Jeong, Zoltán Bodrog, Saskia Fiedler, Tim Schröder, Noelia Vico Triviño, Tomás Palacios, Adam Gali, Milos Toth, Dirk Englund, et al. Bright room-temperature single-photon emission from defects in gallium nitride. *Advanced Materials*, 29(12):1605092, 2017.

[49] Ivan Karomi, Peter M Smowton, Samuel Shutts, Andrey B Krysa, and Richard Beanland. Inasp quantum dot lasers grown by movpe. *Optics Express*, 23(21):27282–27291, 2015.

[50] Dan Dalacu, Khaled Mnaymneh, Jean Lapointe, Xiaohua Wu, Philip J Poole, Gabriele Bulgarini, Val Zwiller, and Michael E Reimer. Ultraclean emission from

inasp quantum dots in defect-free wurtzite inp nanowires. *Nano letters*, 12(11):5919–5923, 2012.

[51] P Kuyanov and RR LaPierre. Photoluminescence and photocurrent from inp nanowires with inasp quantum dots grown on si by molecular beam epitaxy. *Nanotechnology*, 26(31):315202, 2015.

[52] Ting-Yuan Chang, Hyunseok Kim, William A Hubbard, Khalifa M Azizur-Rahman, Jung Jin Ju, Je-Hyung Kim, Wook-Jae Lee, and Diana Huffaker. Inasp quantum dot-embedded inp nanowires toward silicon photonic applications. *ACS Applied Materials & Interfaces*, 14(10):12488–12494, 2022.

[53] Moritz Cygorek, Marek Korkusinski, and Pawel Hawrylak. Atomistic theory of electronic and optical properties of inasp/inp nanowire quantum dots. *Physical Review B*, 101(7):075307, 2020.

[54] Michael E Reimer, Gabriele Bulgarini, Nika Akopian, Moïra Hocevar, Maaike Bouwes Bavinck, Marcel A Verheijen, Erik PAM Bakkers, Leo P Kouwenhoven, and Val Zwiller. Bright single-photon sources in bottom-up tailored nanowires. *Nature communications*, 3(1):737, 2012.

[55] Klaus D Jöns, Lucas Schweickert, Marijn AM Versteegh, Dan Dalacu, Philip J Poole, Angelo Gulinatti, Andrea Giudice, Val Zwiller, and Michael E Reimer. Bright nanoscale source of deterministic entangled photon pairs violating bell's inequality. *Scientific reports*, 7(1):1700, 2017.

[56] Mohd Zeeshan, Nachiket Sherlekar, Arash Ahmadi, Robin L Williams, and Michael E Reimer. Proposed scheme to generate bright entangled photon pairs by application of a quadrupole field to a single quantum dot. *Physical Review Letters*, 122(22):227401, 2019.

[57] M Van Weert. Quantum dots in vertical nanowire devices. 2010.

[58] Leslie Allen, Stephen M Barnett, and Miles J Padgett. *Optical angular momentum*. CRC press, 2016.

[59] Takeshi Inoshita and Hiroyuki Sakaki. Electron relaxation in a quantum dot: Significance of multiphonon processes. *Physical Review B*, 46(11):7260, 1992.

[60] Oliver Gywat, Hubert J Krenner, and Jesse Berezovsky. *Spins in optically active quantum dots: concepts and methods*. John Wiley & Sons, 2009.

[61] Arash Ahmadi. Towards on-demand generation of entangled photons with quantum dots. 2020.

[62] HY Ramirez, CH Lin, CC Chao, Y Hsu, WT You, SY Huang, YT Chen, HC Tseng, Wen-Hao Chang, Sheng-Di Lin, et al. Optical fine structures of highly quantized ingaas/gaas self-assembled quantum dots. *Physical Review B*, 81(24):245324, 2010.

[63] R Seguin, A Schliwa, S Rodt, K Pötschke, UW Pohl, and D Bimberg. Size-dependent fine-structure splitting in self-organized inas/gaas quantum dots. *Physical review letters*, 95(25):257402, 2005.

[64] M Bayer, G Ortner, O Stern, A Kuther, AA Gorbunov, A Forchel, Pawel Hawrylak, S Fafard, K Hinzer, TL Reinecke, et al. Fine structure of neutral and charged excitons in self-assembled in (ga) as/(al) gaas quantum dots. *Physical Review B*, 65(19):195315, 2002.

[65] R Mark Stevenson, Andrew J Hudson, Anthony J Bennett, Robert J Young, Christine A Nicoll, David A Ritchie, and Andrew J Shields. Evolution of entanglement between distinguishable light states. *Physical review letters*, 101(17):170501, 2008.

[66] A Fognini, A Ahmadi, SJ Daley, ME Reimer, and V Zwiller. Universal fine-structure eraser for quantum dots. *Optics express*, 26(19):24487–24496, 2018.

[67] TM Stace, Gerard J Milburn, and CHW Barnes. Entangled two-photon source using biexciton emission of an asymmetric quantum dot in a cavity. *Physical Review B*, 67(8):085317, 2003.

[68] R Mark Stevenson, Robert J Young, Paola Atkinson, Ken Cooper, David A Ritchie, and Andrew J Shields. A semiconductor source of triggered entangled photon pairs. *Nature*, 439(7073):179–182, 2006.

[69] Gabriele Bulgarini, Michael E Reimer, Maaike Bouwes Bavinck, Klaus D Jöns, Dan Dalacu, Philip J Poole, Erik PAM Bakkers, and Val Zwiller. Nanowire waveguides launching single photons in a gaussian mode for ideal fiber coupling. *Nano letters*, 14(7):4102–4106, 2014.

[70] Julien Claudon, Joël Bleuse, Nitin Singh Malik, Maela Bazin, Périne Jaffrennou, Niels Gregersen, Christophe Sauvan, Philippe Lalanne, and Jean-Michel Gérard. A highly efficient single-photon source based on a quantum dot in a photonic nanowire. *Nature Photonics*, 4(3):174–177, 2010.

[71] Gregory Sallen, Adrien Tribu, Thomas Aichele, Régis André, Lucien Besombes, Catherine Bougerol, Maxime Richard, Serge Tatarenko, Kuntheak Kheng, and J-Ph Poizat. Subnanosecond spectral diffusion of a single quantum dot in a nanowire. *Physical Review B*, 84(4):041405, 2011.

[72] Dan Dalacu, Alicia Kam, D Guy Austing, Xiaohua Wu, Jean Lapointe, Geof C Aers, and Philip J Poole. Selective-area vapour–liquid–solid growth of inp nanowires. *Nanotechnology*, 20(39):395602, 2009.

[73] T Heindel, C Schneider, M Lermer, SH Kwon, T Braun, S Reitzenstein, S Höfling, M Kamp, and A Forchel. Electrically driven quantum dot-micropillar single photon source with 34% overall efficiency. *Applied Physics Letters*, 96(1), 2010.

[74] Maarten P van Kouwen, Michael E Reimer, Anne W Hidma, Maarten HM Van Weert, Rienk E Algra, Erik PAM Bakkers, Leo P Kouwenhoven, and Val Zwiller. Single electron charging in optically active nanowire quantum dots. *Nano letters*, 10(5):1817–1822, 2010.

[75] Gabriele Bulgarini, Michael E Reimer, Tilman Zehender, Moïra Hocevar, Erik PAM Bakkers, Leo P Kouwenhoven, and Valery Zwiller. Spontaneous emission control of single quantum dots in bottom-up nanowire waveguides. *Applied Physics Letters*, 100(12), 2012.

[76] AJ Bennett, Y Cao, DJP Ellis, I Farrer, DA Ritchie, and AJ Shields. Combining fast electrical control and resonant excitation to create a wavelength-tunable and coherent quantum-dot light source. In *Quantum Dots and Nanostructures: Synthesis, Characterization, and Modeling XII*, volume 9373, page 937302. SPIE, 2015.

[77] Michael E Reimer and Catherine Cher. The quest for a perfect single-photon source. *Nature Photonics*, 13(11):734–736, 2019.

[78] Niccolo Somaschi, Valerian Giesz, Lorenzo De Santis, JC Loredo, Marcelo P Almeida, Gaston Hornecker, S Luca Portalupi, Thomas Grange, Carlos Anton, Justin Demory, et al. Near-optimal single-photon sources in the solid state. *Nature Photonics*, 10(5):340–345, 2016.

[79] Ana Predojević. Resonant excitation and photon entanglement from semiconductor quantum dots. *Engineering the Atom-Photon Interaction: Controlling Fundamental Processes with Photons, Atoms and Solids*, pages 303–324, 2015.

[80] AJ Ramsay, TM Godden, SJ Boyle, Erik M Gauger, Ahsan Nazir, Brendon William Lovett, AM Fox, and MS Skolnick. Phonon-induced rabi-frequency renormalization of optically driven single ingaas/gaas quantum dots. *Physical review letters*, 105(17):177402, 2010.

[81] Martin Glässl, Andreas M Barth, and Vollrath Martin Axt. Proposed robust and high-fidelity preparation of excitons and biexcitons in semiconductor quantum dots making active use of phonons. *Physical review letters*, 110(14):147401, 2013.

[82] Rodney Loudon. *The quantum theory of light*. OUP Oxford, 2000.

[83] Daniel FV James, Paul G Kwiat, William J Munro, and Andrew G White. Measurement of qubits. *Physical Review A*, 64(5):052312, 2001.

[84] DE Reiter. Influence of acoustic phonons on the optical control of quantum dots driven by adiabatic rapid passage. *Physical Review B*, 85(12):121302, 2012.

[85] Sebastian Lüker and Doris E Reiter. A review on optical excitation of semiconductor quantum dots under the influence of phonons. *Semiconductor Science and Technology*, 34(6):063002, 2019.

[86] Charles Santori, David Fattal, Jelena Vučković, Glenn S Solomon, Edo Waks, and Yoshihisa Yamamoto. Submicrosecond correlations in photoluminescence from inas quantum dots. *Physical Review B*, 69(20):205324, 2004.

[87] Jingzhong Yang, Tom Fandrich, Frederik Benthin, Robert Keil, Nand Lal Sharma, Weijie Nie, Caspar Hopfmann, Oliver G Schmidt, Michael Zopf, and Fei Ding. Photoneutralization of charges in gaas quantum dot based entangled photon emitters. *Physical Review B*, 105(11):115301, 2022.

[88] Dharmendar Kumar Sharma, Shuzo Hirata, Lukasz Bujak, Vasudevanpillai Biju, Tatsuya Kameyama, Marino Kishi, Tsukasa Torimoto, and Martin Vacha. Single-particle spectroscopy of i–iii–vi semiconductor nanocrystals: spectral diffusion and suppression of blinking by two-color excitation. *Nanoscale*, 8(28):13687–13694, 2016.

[89] Olaf Stenzel. Light-matter interaction. *Cham: Springer Nature*, 2022.

[90] Roel Baets, Ananth Z Subramanian, Stéphane Clemmen, Bart Kuyken, Peter Bienstman, Nicolas Le Thomas, Günther Roelkens, Dries Van Thourhout, Philippe Helin, and Simone Severi. Silicon photonics: Silicon nitride versus silicon-on-insulator. In *Optical Fiber Communication Conference*, pages Th3J–1. Optica Publishing Group, 2016.

[91] René Heideman, Arne Leinse, Willem Hoving, Ronald Dekker, Douwe Geuzebroek, Edwin Klein, Remco Stoffer, Chris Roeloffzen, Leimeng Zhuang, and Arjan Meijerink. Large-scale integrated optics using triplex waveguide technology: from uv to ir. In *Photonics Packaging, Integration, and Interconnects IX*, volume 7221, pages 203–217. SPIE, 2009.

[92] Xingcun Colin Tong Ph. D and Xingcun Colin Tong. Fundamentals and design guides for optical waveguides. *Advanced Materials for Integrated Optical Waveguides*, pages 1–51, 2014.

[93] Lukas Chrostowski and Michael Hochberg. *Silicon photonics design: from devices to systems*. Cambridge University Press, 2015.

[94] Coupled-mode theory for guided-wave optics. *IEEE Journal of Quantum Electronics*, 9(9):919–933, 1973.

[95] Matteo GA Paris. Entanglement and visibility at the output of a mach-zehnder interferometer. *Physical Review A*, 59(2):1615, 1999.

[96] R Chevalerias, Y Latron, and C Veret. Methods of interferometry applied to the visualization of flows in wind tunnels. *JOSA*, 47(8):703–706, 1957.

[97] D Naylor. Recent developments in the measurement of convective heat transfer rates by laser interferometry. *International Journal of Heat and Fluid Flow*, 24(3):345–355, 2003.

[98] WK Lai, V Buek, and PL Knight. Nonclassical fields in a linear directional coupler. *Physical Review A*, 43(11):6323, 1991.

[99] Herwig Kogelnik and R V Schmidt. Switched directional couplers with alternating $\delta\beta$. *IEEE Journal of Quantum Electronics*, 12(7):396–401, 1976.

[100] Daoxin Dai, Zhi Wang, and John E Bowers. Considerations for the design of asymmetrical mach–zehnder interferometers used as polarization beam splitters on a submicrometer silicon-on-insulator platform. *Journal of Lightwave Technology*, 29(12):1808–1817, 2011.

[101] Mingbo Pu, Na Yao, Chenggang Hu, Xuecheng Xin, Zeyu Zhao, Changtao Wang, and Xiangang Luo. Directional coupler and nonlinear mach-zehnder interferometer based on metal-insulator-metal plasmonic waveguide. *Optics Express*, 18(20):21030–21037, 2010.

[102] Wim Bogaerts, Peter De Heyn, Thomas Van Vaerenbergh, Katrien De Vos, Shankar Kumar Selvaraja, Tom Claes, Pieter Dumon, Peter Bienstman, Dries Van Thourhout, and Roel Baets. Silicon microring resonators. *Laser & Photonics Reviews*, 6(1):47–73, 2012.

[103] Ali W. Elshaari, Iman Esmaeil Zadeh, Klaus D. Jöns, and Val Zwiller. Thermo-optic characterization of silicon nitride resonators for cryogenic photonic circuits. *IEEE Photonics Journal*, 8(3):1–9, 2016.

[104] Zhiping Zhou, Bing Yin, and Jurgen Michel. On-chip light sources for silicon photonics. *Light: Science & Applications*, 4(11):e358–e358, 2015.

[105] Zhaohui Ma, Jia-Yang Chen, Zhan Li, Chao Tang, Yong Meng Sua, Heng Fan, and Yu-Ping Huang. Ultrabright quantum photon sources on chip. *Physical Review Letters*, 125(26):263602, 2020.

[106] Ali W Elshaari, Iman Esmaeil Zadeh, Andreas Fognini, Michael E Reimer, Dan Dalacu, Philip J Poole, Val Zwiller, and Klaus D Jöns. On-chip single photon filtering and multiplexing in hybrid quantum photonic circuits. *Nature communications*, 8(1):379, 2017.

[107] Xingyu Chen, Rongbin Su, Jin Liu, Juntao Li, and Xue-Hua Wang. Scalable and highly efficient approach for an on-chip single-photon source. *Photonics Research*, 10(9):2066–2072, 2022.

[108] Jason CC Mak, Quentin Wilmart, Ségolène Olivier, Sylvie Menezo, and Joyce KS Poon. Silicon nitride-on-silicon bi-layer grating couplers designed by a global optimization method. *Optics express*, 26(10):13656–13665, 2018.

[109] Min Liu, Daigao Chen, Xiao Hu, Peng Feng, and Xi Xiao. Efficient silicon nitride grating coupler with silicon reflector at near-infrared wavelengths. In *Asia Communications and Photonics Conference*, pages M4A–166. Optica Publishing Group, 2020.

[110] Na Fang, Zhifeng Yang, Aimin Wu, Jing Chen, Miao Zhang, Shichang Zou, and Xi Wang. Three-dimensional tapered spot-size converter based on (111) silicon-on-insulator. *IEEE Photonics Technology Letters*, 21(12):820–822, 2009.

[111] Minhao Pu, Liu Liu, Haiyan Ou, Kresten Yvind, and Jørn M Hvam. Ultra-low-loss inverted taper coupler for silicon-on-insulator ridge waveguide. *Optics Communications*, 283(19):3678–3682, 2010.

[112] Qing Li, Marcelo Davanço, and Kartik Srinivasan. Efficient and low-noise single-photon-level frequency conversion interfaces using silicon nanophotonics. *Nature Photonics*, 10(6):406–414, 2016.

APPENDICES

Projection Measurements

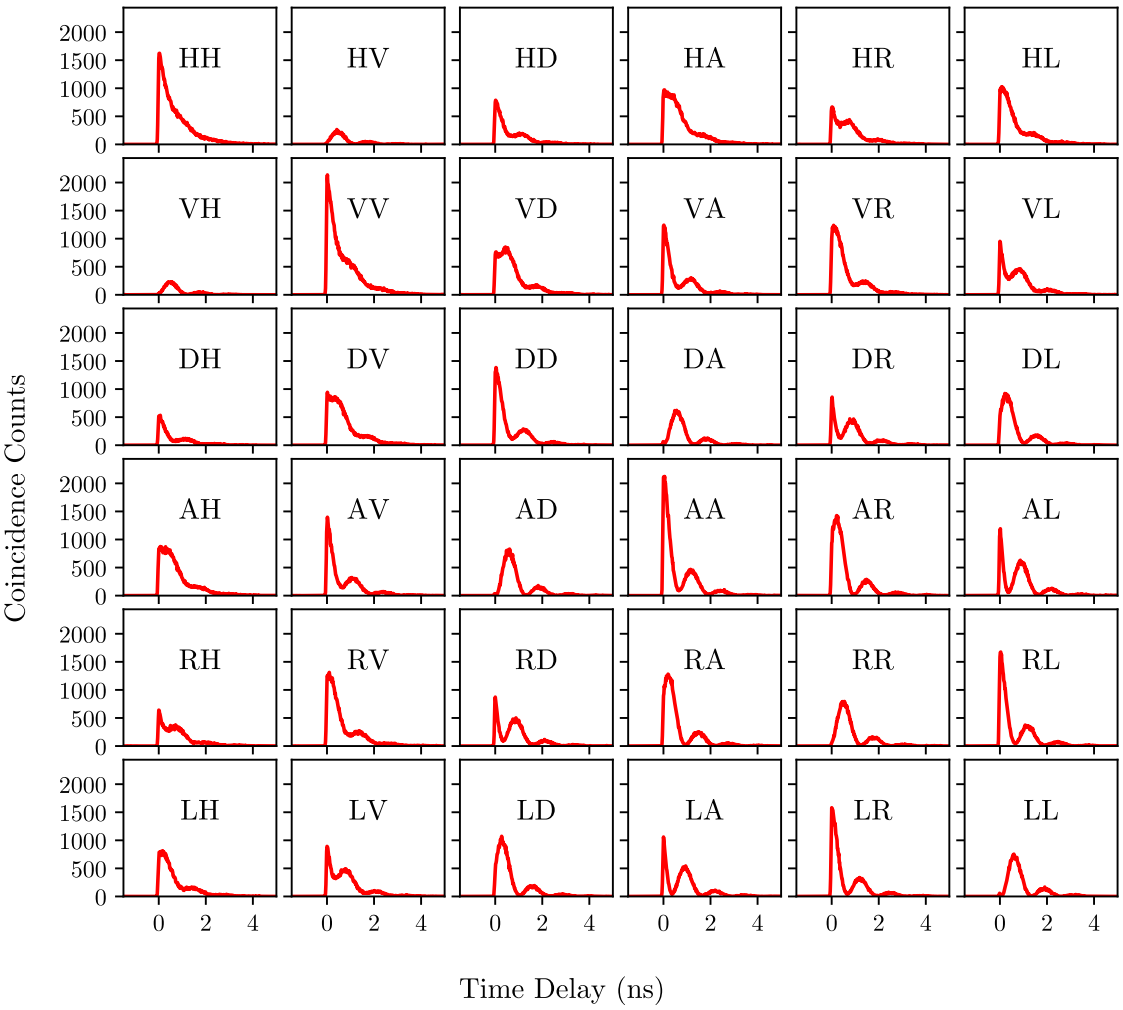

Figure 1: Raw projection measurements captured by the SNSPDs used in the reconstruction of the density matrix, as part of the quantum state tomography experiment. The well-defined oscillations shows that the SNSPDs are capable of resolving the fss, thus leading to a more accurate reconstruct

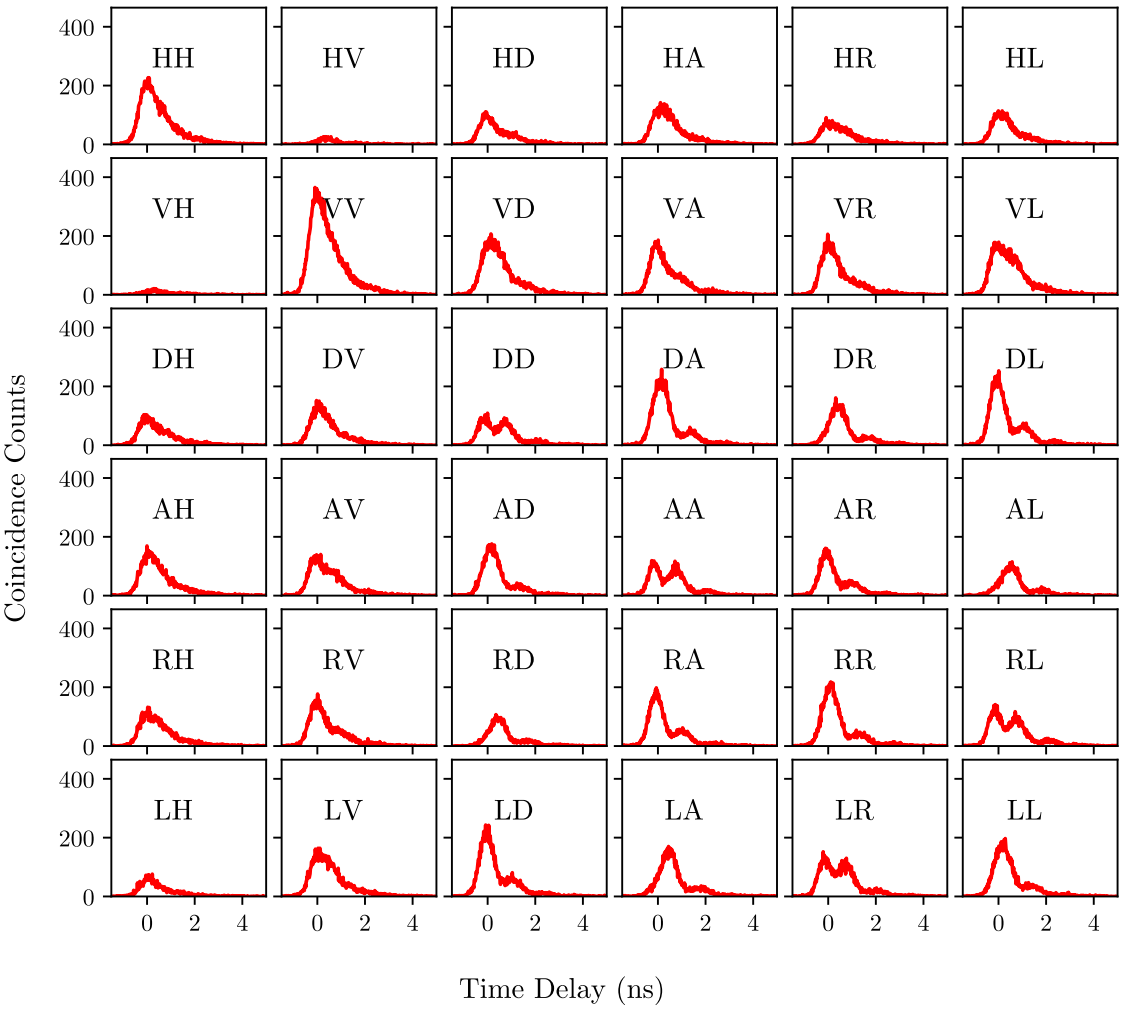

Figure 2: Raw projection measurements captured by the SPADs used in the reconstruction of the density matrix, as part of the quantum state tomography experiment. It is evident from the "rounded" peaks and less defined oscillations that the response time of the SPADs are much slower than the SNSPDs.

Final PIC Circuit Design

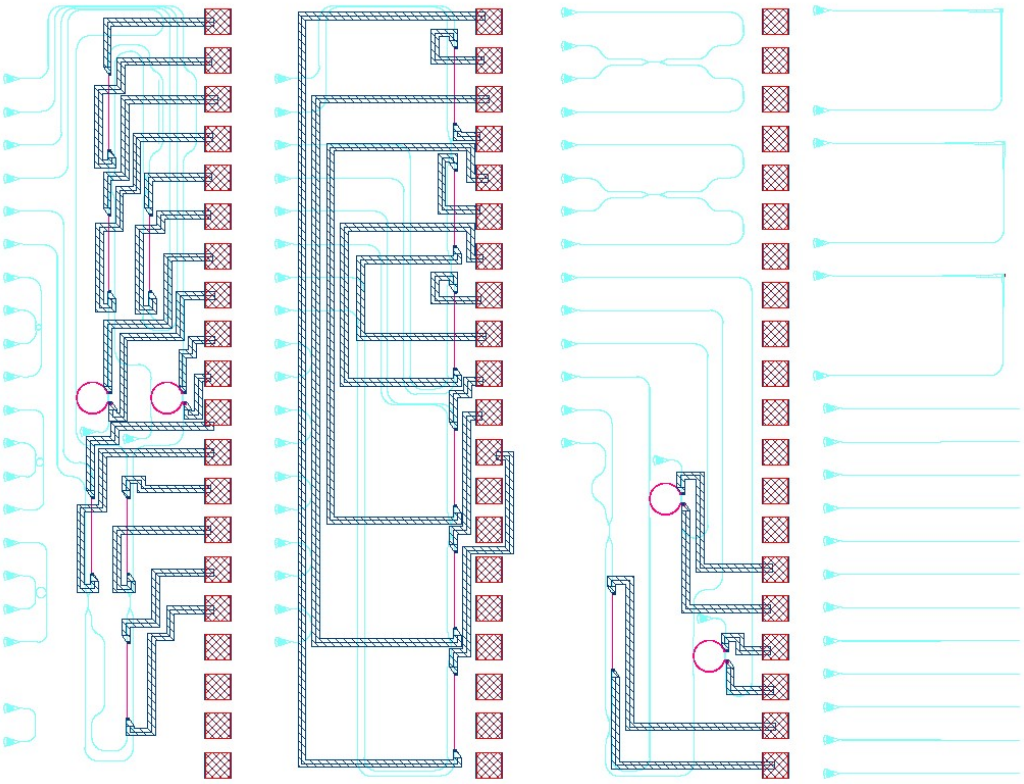

Figure 3: Final AMF PIC, as designed in KLayout. The "teal" colour represents SiN_x structures, such as waveguides, directional couplers, and grating couplers. The thin "pink" lines and circles are heaters placed on top of waveguides and ring resonators respectively. The "red" hatched squares are bond-pads, where electrical connections can be made to control the heating elements. And the "blue" hatched areas are electrical connections between the bond-pads and the heating elements. the circuit has been split into four equal sections, each containing their own experiment which are intended to emulate free space lab experiments carried out in this thesis. From left to right, the experiments are: 1) Tomography where the XX and X are filtered on-chip, 2) tomography where the XX and X photons are filtered off-chip, 3) HOM and two-photon interference, and 4) experimental edge couplers and 2D grating couplers. Note, the 2D grating couplers are not part of this thesis, but they offer a method of separating photons into either waveguide based on their polarization.